

WFC3 TV3 Testing: UVIS Window Contamination

Thomas M. Brown, George Hartig, & Sylvia Baggett
May 27, 2008

ABSTRACT

During the most recent WFC3 thermal vacuum (TV) testing campaign, it was discovered that the outer window of the UVIS flight detector (UVIS-1') is contaminated. The contamination appears to be the mineral residue of an earlier condensation event which has been traced to a period of acceptance testing at Ball Aerospace. These features have been dubbed "droplets" due to their appearance at the time of discovery. We characterized the impact of these features on UVIS channel performance with a series of tests using both point source and flat-field illumination. In large-aperture (10 pixel radius) photometry of point sources stepped across a strong window feature, the feature does not significantly increase the photometric scatter. For small-aperture (3 pixel radius) photometry of point sources stepped across a strong window feature, the photometric scatter increases from ~0.5% to ~1%, with little to no mitigation via flat-fielding, because light in the core of the point spread function is redirected to the near wings. However, the effect of these droplets can be mitigated through appropriate dithering of observations.

Background

The Wide Field Camera 3 (WFC3) recently underwent ground testing under thermal vacuum (TV) conditions. The flight UVIS detector (UVIS-1') is currently installed in the instrument, replacing the spare detector in use during the 2007 TV tests (UVIS-2). The flight detector used in the original 2004 TV tests (UVIS-1) was rebuilt to replace its thermoelectric cooler, and subsequently renamed UVIS-1'. Although the rework of the flight detector at Ball Aerospace was successful, the subsequent acceptance tests were problematic. Apparently, during the thermal cycling of those tests, condensation formed on the outer window of the detector package. Although this condensation evaporated, it left mineral deposits on the outer window.

These deposits are on the order of 100 microns in diameter, and thus not obvious to the naked eye when looking at the detector package. When illuminated by the f/31 science beam, these deposits cause faint bulls-eye patterns in flat-field images; the patterns are ~100 pixels in diameter

and produce a modulation of approximately $\pm 0.5\%$ in the flat-field image (see Figure 1). Unfortunately, the calibration subsystem produces internal flats with a highly collimated beam (i.e., $f/\#$ roughly two orders of magnitude higher), and in such internal flats the effects of the droplets are much worse (Figure 2); they become more compact (~ 10 pixels in diameter) and the modulation is much stronger (tens of percent). Although observers will not see such strong effects in their science data (which will always be in the $f/31$ beam), the strength of these features in the internal flats will complicate the use of internal flat-field images in the production of appropriate calibration reference files.

There are approximately 500 of these droplets on the detector window. Their distribution is not uniform; there are approximately 50, 129, 108, and 179 droplets in quadrants A, B, C, and D, respectively. Because the flat-field features from these droplets have a radius of approximately 50 pixels, that means the fraction of area covered in quadrants A, B, C, and D is approximately 9%, 24%, 20%, and 33%.

For a point source, the $f/31$ science beam is an annulus at the detector window, with the outer radius of the annulus being somewhere in the 1.2 to 2.4 mm range (depending upon field position). The inner radius of the annulus is 46% of the outer radius of the annulus with the central obscuration of the CASTLE optical stimulus used in ground testing, but it is 33% with the central obscuration of the HST OTA in orbit. This means that a point source centered on a detector-window defect will not be affected by that defect, but an offset of approximately 40 pixels will maximize the effect of that defect, because the defect will fall within the science beam annulus at the window.

Another complication is that the droplets are not simply blocking a fraction of the light projected on the detector. The droplets have refractive and diffractive effects so they cannot be completely remedied by applying a straightforward flat-field correction.

To investigate the effects of these droplets on science observations, we obtained a series of flat-field and point-source images in filters spanning the full wavelength range of the UVIS channel. We stepped the position of the point source in the vicinity of various flat-field features to characterize the impact on both photometric accuracy and encircled energy. We also obtained flat-field images spaced in time over the course of the TV campaign, to monitor the stability of these features. In this report we summarize the results of these investigations.

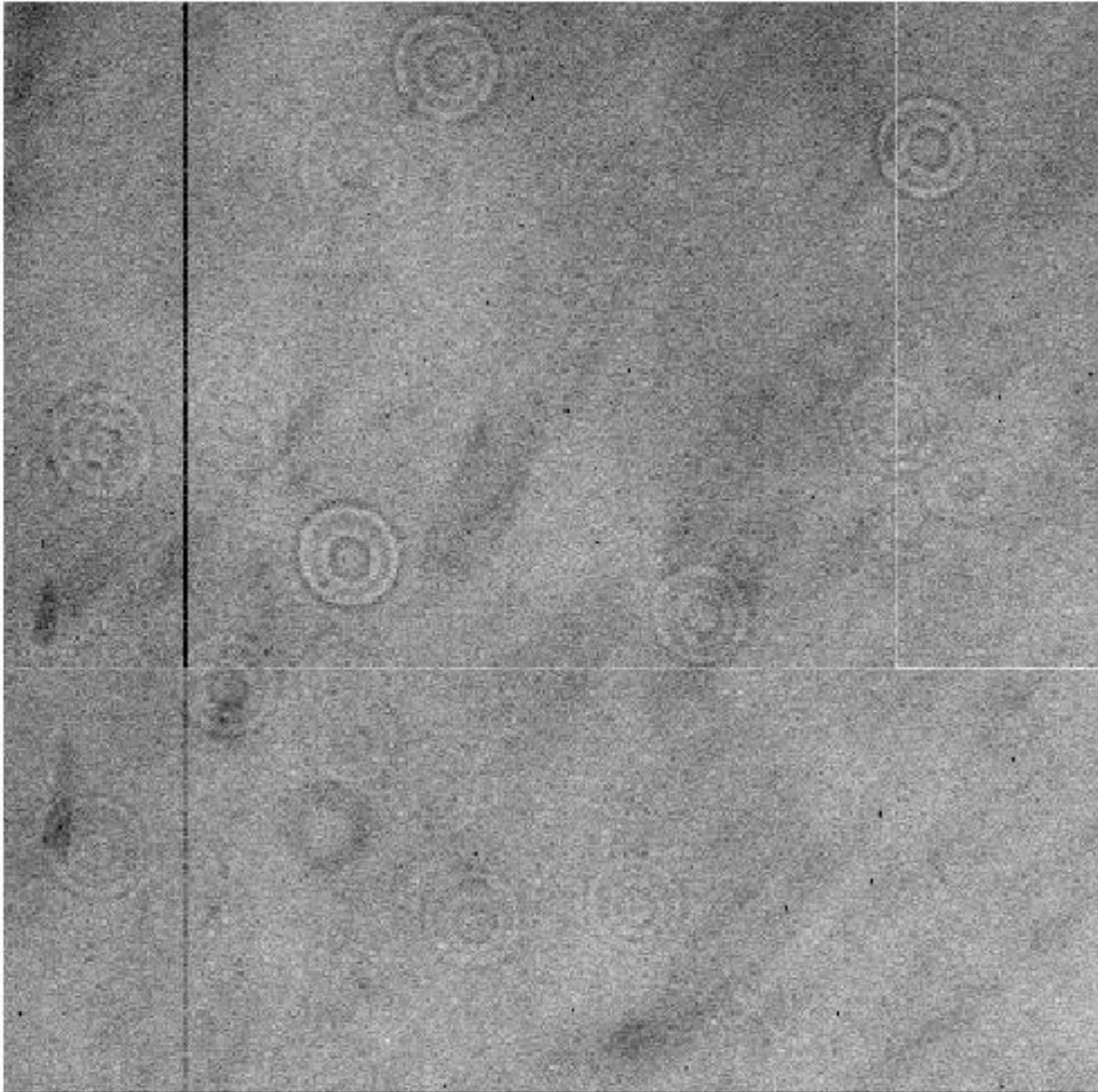


Figure 1: A 800x800 pixel subsection of an F438W flat-field image taken with external illumination. The faint bulls-eye patterns due to the mineral deposits on the detector window are a modulation of approximately $\pm 0.5\%$ in the image.

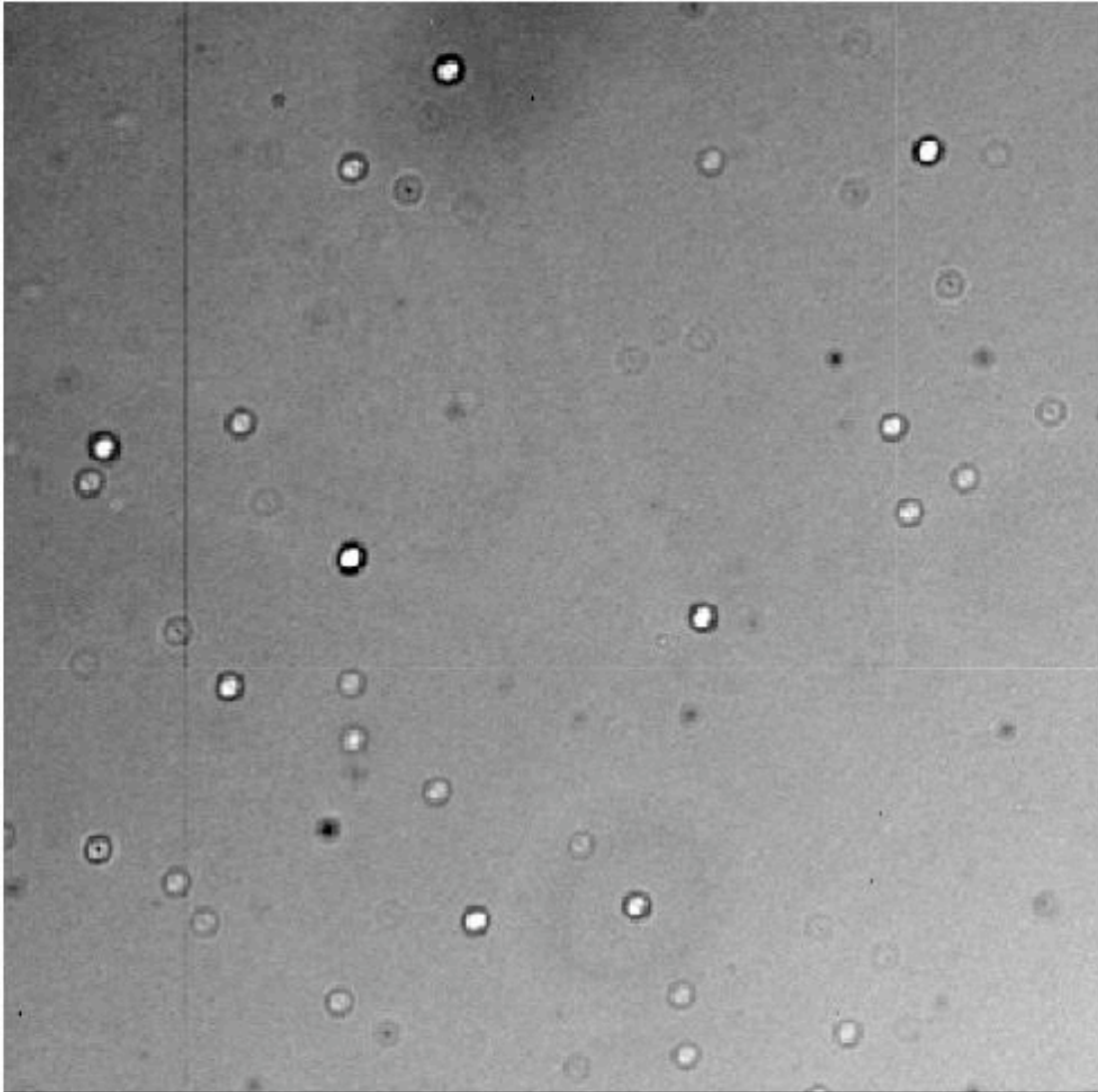


Figure 2: An F438W flat-field image of the same region shown in Figure 1, but now the illumination comes from the highly-collimated internal calibration lamp, which significantly strengthens the impact of material on the detector window. The spots with bright cores are from the droplets (i.e., mineral deposits), whereas the dark spots are from dust motes.

Photometry Investigation

The photometry investigation was performed via a series of tests that stepped a point source (the 10 micron fiber on the “CASTLE” optical stimulus) to various positions in the vicinity of a flat-field feature. The point source was well-exposed in each image - roughly half of full well (i.e., no linearity or saturation issues) but with more than 100,000 electrons within a 3-pixel radius aperture (i.e., signal-to-noise ratio exceeding 300). These tests were performed with 5 filters: F225W, F275W, F336W, F438W, and F814W. In the initial tests, the point source was placed at 13 positions in the vicinity of a feature, stepping by 20 pixels in X and Y, with a position at the center of the feature repeated twice to check the stability of the optical stimulus. In later tests, the number of positions was increased from 13 to 17, with the central position checked 5 times to monitor stability.

Six different regions on the detector were chosen to represent the types of flat-field features one can encounter (Figure 3). These regions were given self-explanatory names: bad droplet #1, bad droplet #2, clean area #1, clean area #2, dust mote, and small droplet. The bad droplets are representative of the worst droplet features on the detector, while the small droplet is representative of the weaker droplet features. Two clean regions relatively free of flat-field features were chosen to provide a baseline for judging the photometric variation seen in the vicinity of various flat-field features. Finally, before the window was contaminated with these droplet features, it was already littered with dust motes that have their own effects on the photometry; the dust mote region was thus chosen to see how the new flat-field features compare to the existing ones.

Each point source image was reduced with a minimal pipeline, including subtraction of a superbias and division by a superflat. Aperture photometry was performed with two different radii: 3 pixels and 10 pixels. The aperture photometry was performed both before flat-fielding and after flat-fielding, to gauge how well these features can be corrected. All photometry was normalized to the first sample in the center of the feature. The individual photometric measurements are shown in the Appendix figures A1 - A30, and summarized by filter in figures A31 - A35.

In Figure 4, we show the photometric scatter vs. wavelength for each of the six regions shown in Figure 3. In a large aperture (10 pixel radius), photometry on flat-fielded images shows the same low level of scatter in all regions of the detector. However, in a small aperture (3 pixel radius), photometry on flat-fielded images shows a low level of scatter only in those regions that are clean or free of strong droplets; in the vicinity of strong droplets, the photometric scatter is roughly twice as large as it is in clean regions, and is not mitigated by flat-fielding. This is because the droplets have diffractive and refractive effects, which would really require a deconvolution to correct properly. Even so, the scatter has only increased from the sub-1% level to just over 1%. Furthermore, the increased scatter is largely due to a few outliers (at the level of a few percent; e.g., Figure A2) in the set of point source images taken at various positions in the vicinity of a flat-field feature. Appropriately dithered science exposures will reduce this scatter significantly; dithers of approximately 100 pixels will move a point source off a droplet.

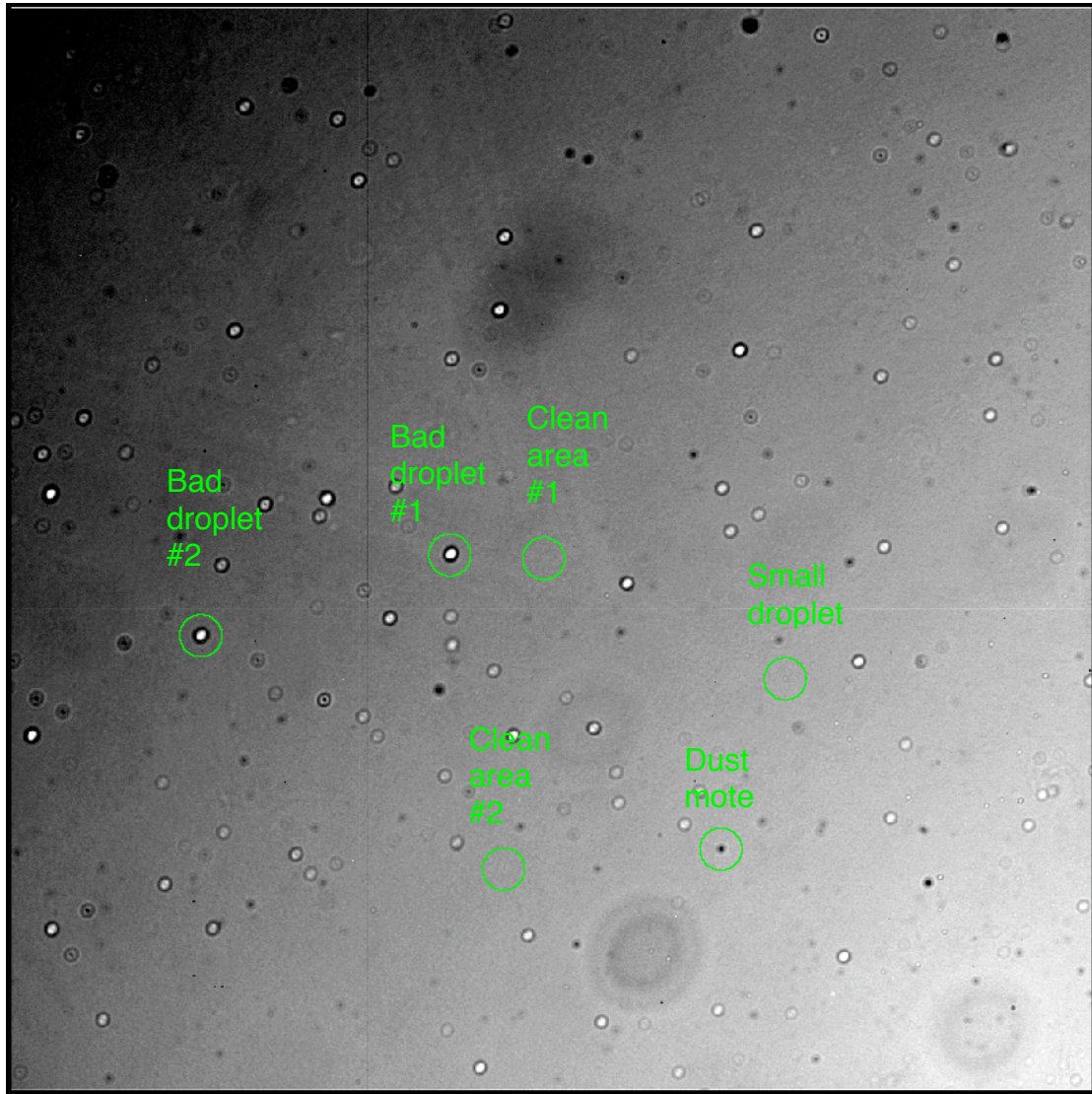


Figure 3: A subsection of an internal flat, with its highly collimated beam accentuating the flat-field features that arise from material on the detector window. The six regions of the detector used to check photometric scatter in the presence of flat-field features are labeled.

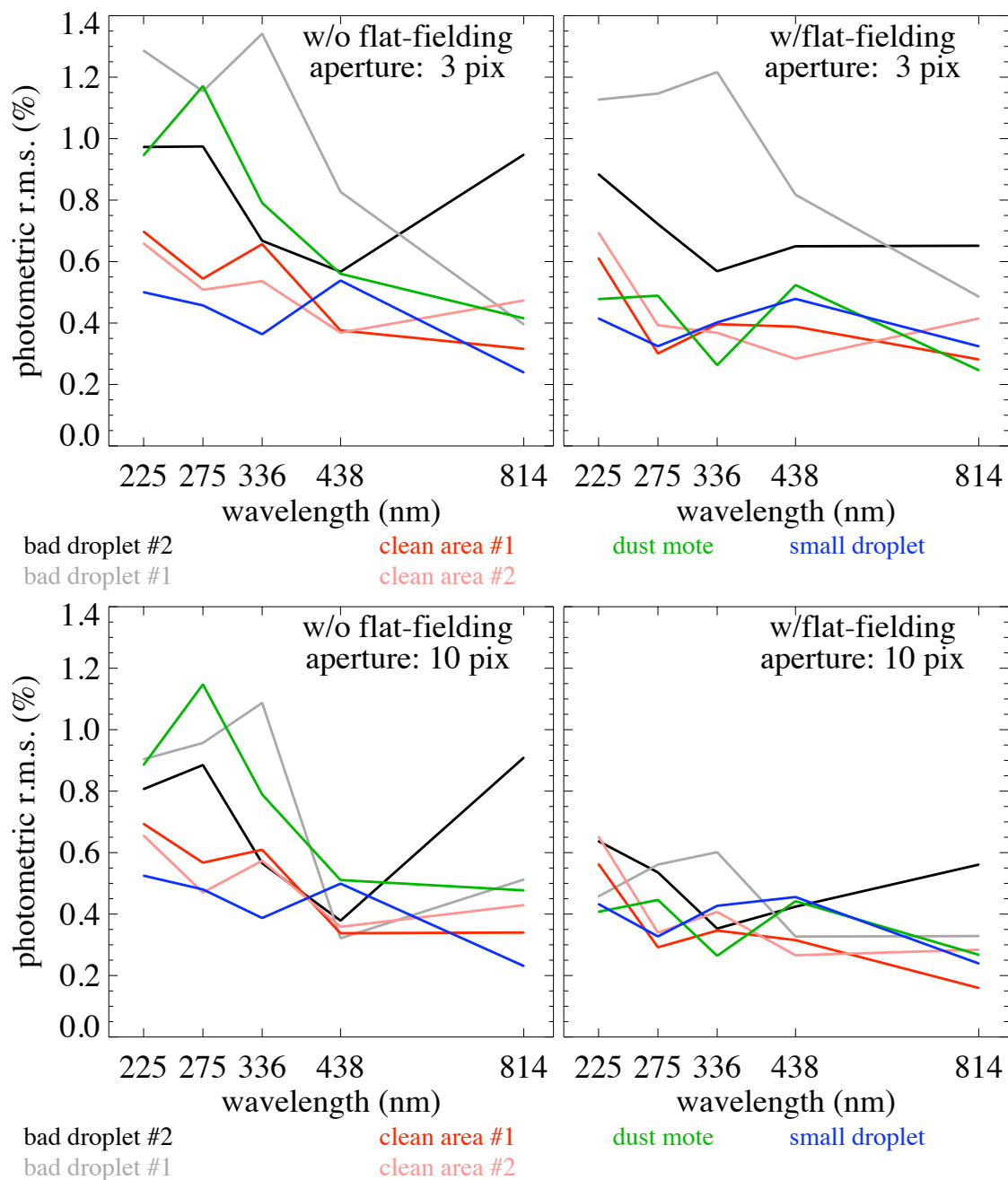


Figure 4: A high-level summary of the photometric measurements made in the vicinity of the flat-field regions shown in Figure 3. In 10-pixel aperture photometry (bottom panels), the photometric scatter for all six regions on the detector was significantly improved by flat-fielding, such that the regions with flat-field features (grey, black, green, and blue curves) showed the same performance as the clean regions (red curves). In 3-pixel aperture photometry (top panels), the photometric scatter for photometry in the vicinity of strong droplets (grey and black curves) is not much improved by flat-fielding, but the photometric scatter in the vicinity of weak flat-field features (blue and green curves) is improved by flat-fielding to the level seen in the clean regions (red curves).

Point Spread Function and Encircled Energy

In the previous section, we showed that 10-pixel aperture photometry on flat-fielded images suffers from little scatter in the vicinity of droplets (i.e., as much scatter as clean regions), but 3-pixel aperture photometry on flat-fielded images exhibits roughly twice the scatter in the vicinity of strong droplets as that in clean regions. It seems likely that a point source placed in the vicinity of a strong droplet has its light redirected from the core to the wings. This should be apparent in the encircled energy curves for point sources placed in a droplet region.

With this in mind, we explored the properties of the point spread function (PSF) when a point source was placed in a subset of the various flat-field features discussed in the previous section. We used a range of exposure times to increase the dynamic range in these measurements, providing well-exposed images of both the PSF core and wings.

At first, we found practically no differences in the PSF and encircled energy curves when the point source was placed in the vicinity of clean area #2, bad droplet #2, the small droplet, and the dust mote (Figure 5). In these measurements through the F438W and F814W filters, the window defect was placed within the annulus of the science beam, to try and maximize the effect of the defect (i.e., we did not center the defect in the annulus, because then it would have no effect).

We then extended these measurements into the UV and tried more point source positions. We again placed the window defect within the f/31 science beam annulus, and then stepped the point source in 4 pixel (~60 micron) increments to move the edge of the annulus across the window defect. No significant variation was seen in the encircled energy curves or the PSF profile as the point source was stepped (Figures 6 and 7; figures in Appendix B show the actual PSF images during this stepping). A small fraction (~0.2%) of the PSF energy was redistributed from the core into the wings as the point source was stepped across bad droplet #2 (Figure 8). This was puzzling, because the point source photometry in the vicinity of the droplets showed that the photometric scatter could increase by a factor of two, largely due to a few outliers at the level of a few percent (e.g., see Figure A2). At a few positions, the encircled energy curves should show a few percent of the light scattered from the core to the wings.

We next put the point source in the exact location within the “bad droplet #1” region showing the largest photometric variation; this is 40 pixels to the right of center in Figure A2. Here, we did in fact see a redistribution of energy from the core to the wings at the level of 2% (Figures 9 and 10), which is consistent with the small-aperture (3 pixel radius) photometry performed in Figure A2. Thus, the PSF measurements and aperture photometry are consistent. Furthermore, as found in the photometric analysis, most of the point source positions in the vicinity of a window feature show little variation in the PSF; instead, there are a few outlier positions with variation at the level of a few percent. To see a variation of a few percent in the aperture photometry and PSF profile, the point source needs to hit a particularly unlucky position in the vicinity of a window feature, while most of the positions in this vicinity will cause variation at the sub-1% level.

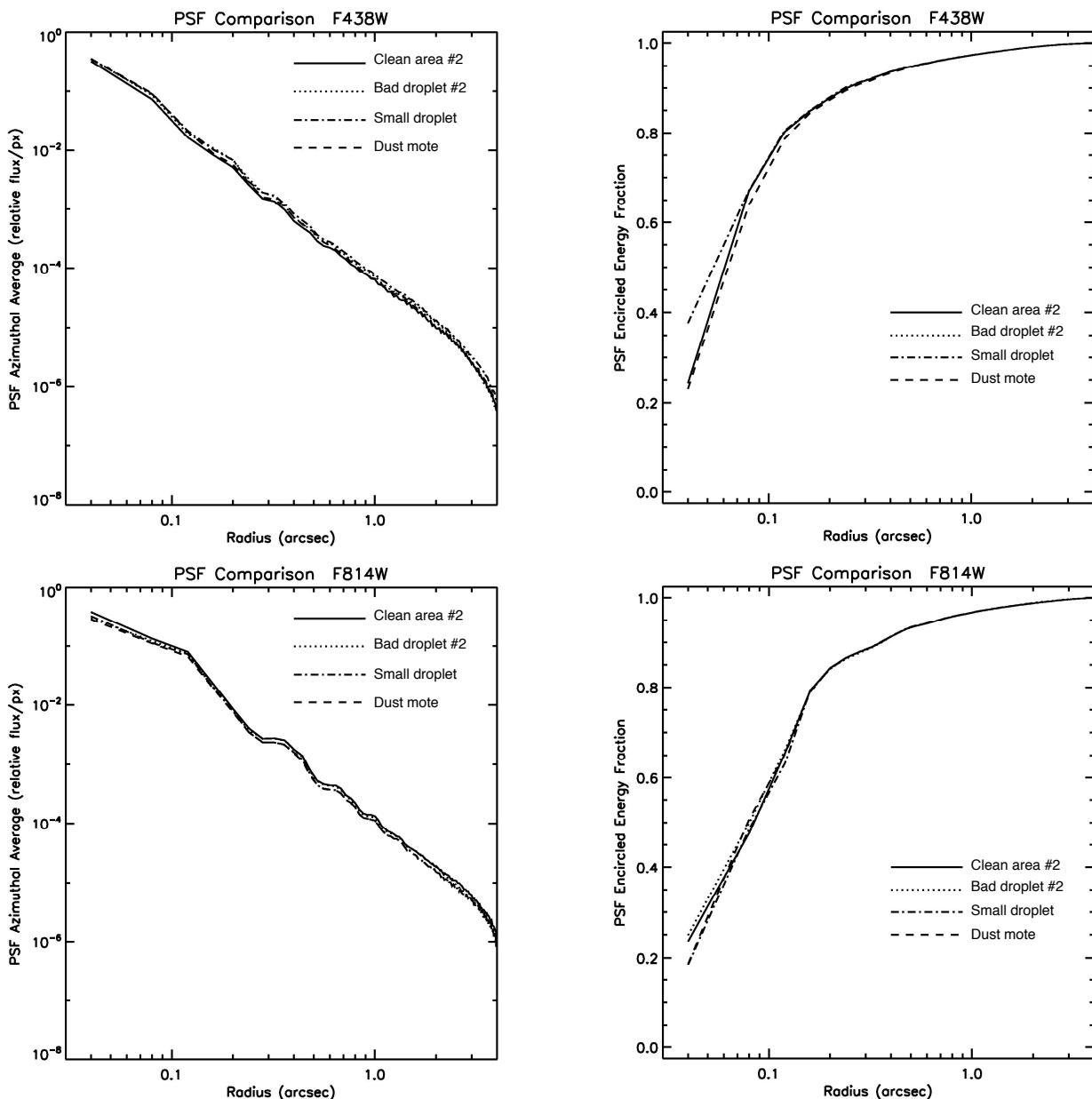


Figure 5: Measurements of the PSF (left panels) and encircled energy (right panels) in the F438W (top panels) and F814W (bottom panels) filters, with the point source placed in four representative regions for flat-field features. These regions are shown in Figure 3. In each measurement here, the point source was placed such that the annulus of the f/31 science beam intersects the defect (in the case of the bad droplet, small droplet, and dust mote); i.e., off-center from the defect itself. The differences between the PSF profile and encircled energy curve are very small when comparing different regions. The differences seen at small radii are due to slight differences in how well the point source was centered within a pixel.

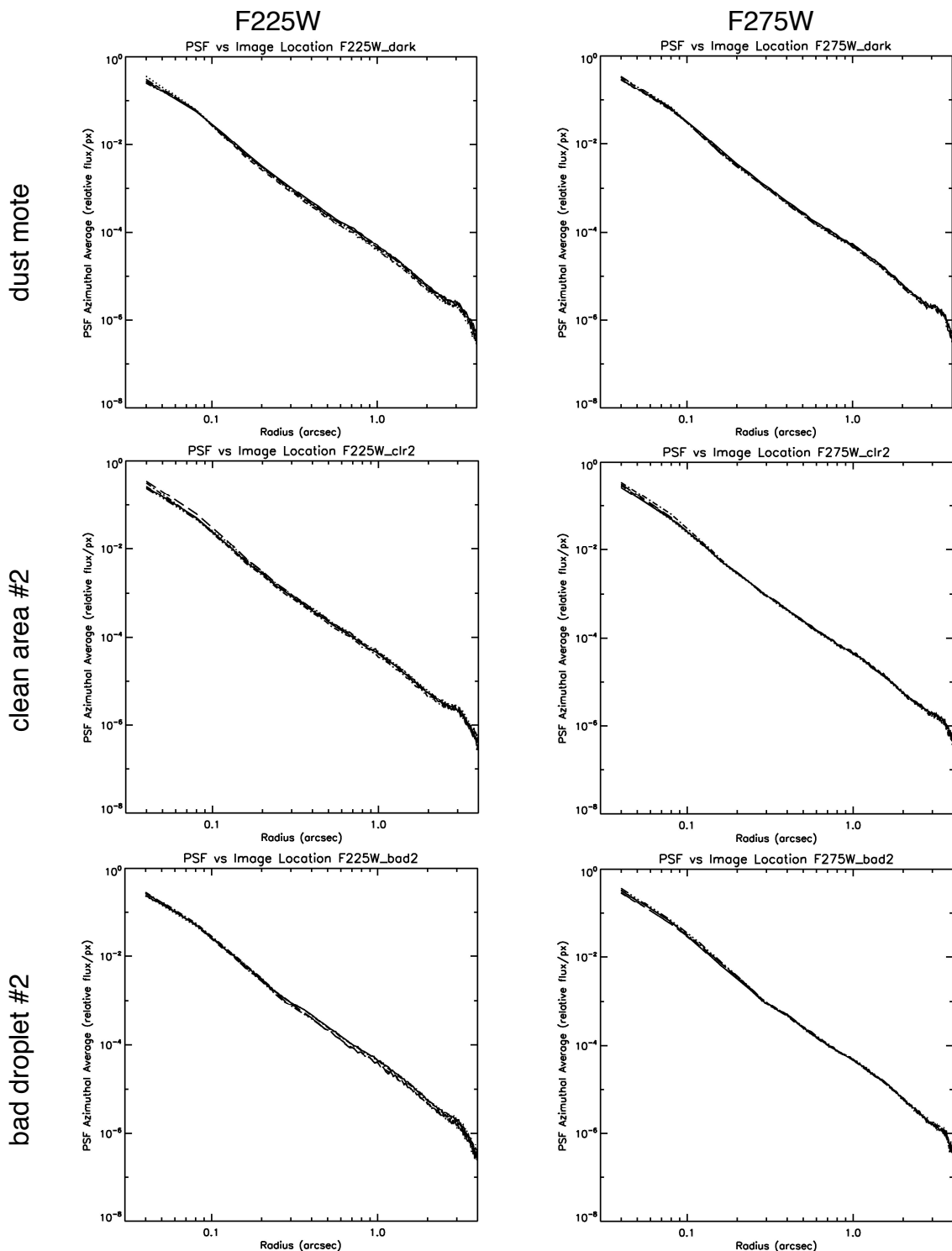


Figure 6: The PSF profile as the point source is stepped in 4 pixel increments across a window feature shows little to no variation with position. The point source was stepped such that the window feature was moved across the annulus of the f/31 science beam.

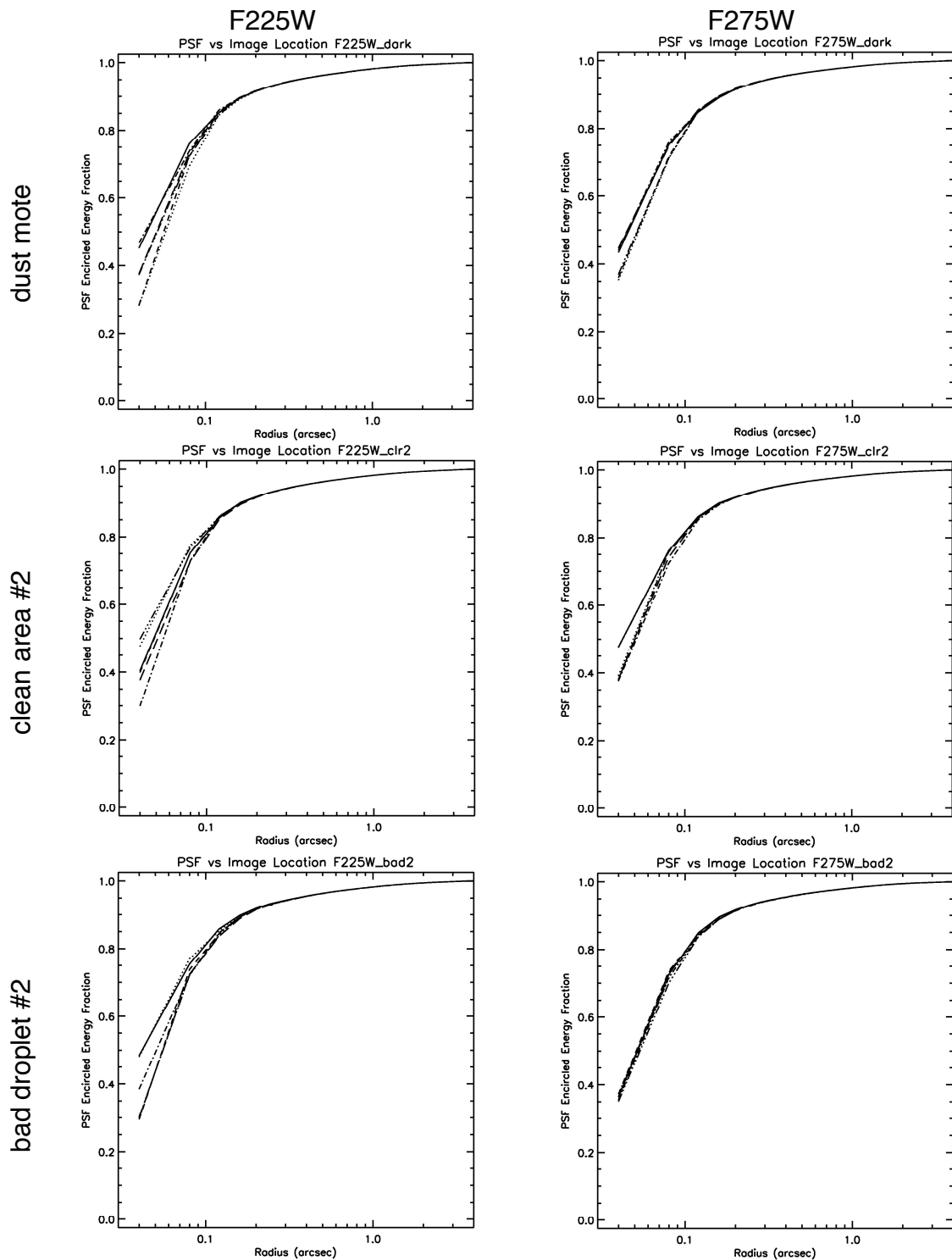


Figure 7: The encircled energy curves as the point source is stepped in 4 pixel increments across a window feature show little to no variation with position. The point source was stepped such that the window feature was moved across the annulus of the f/31 science beam.

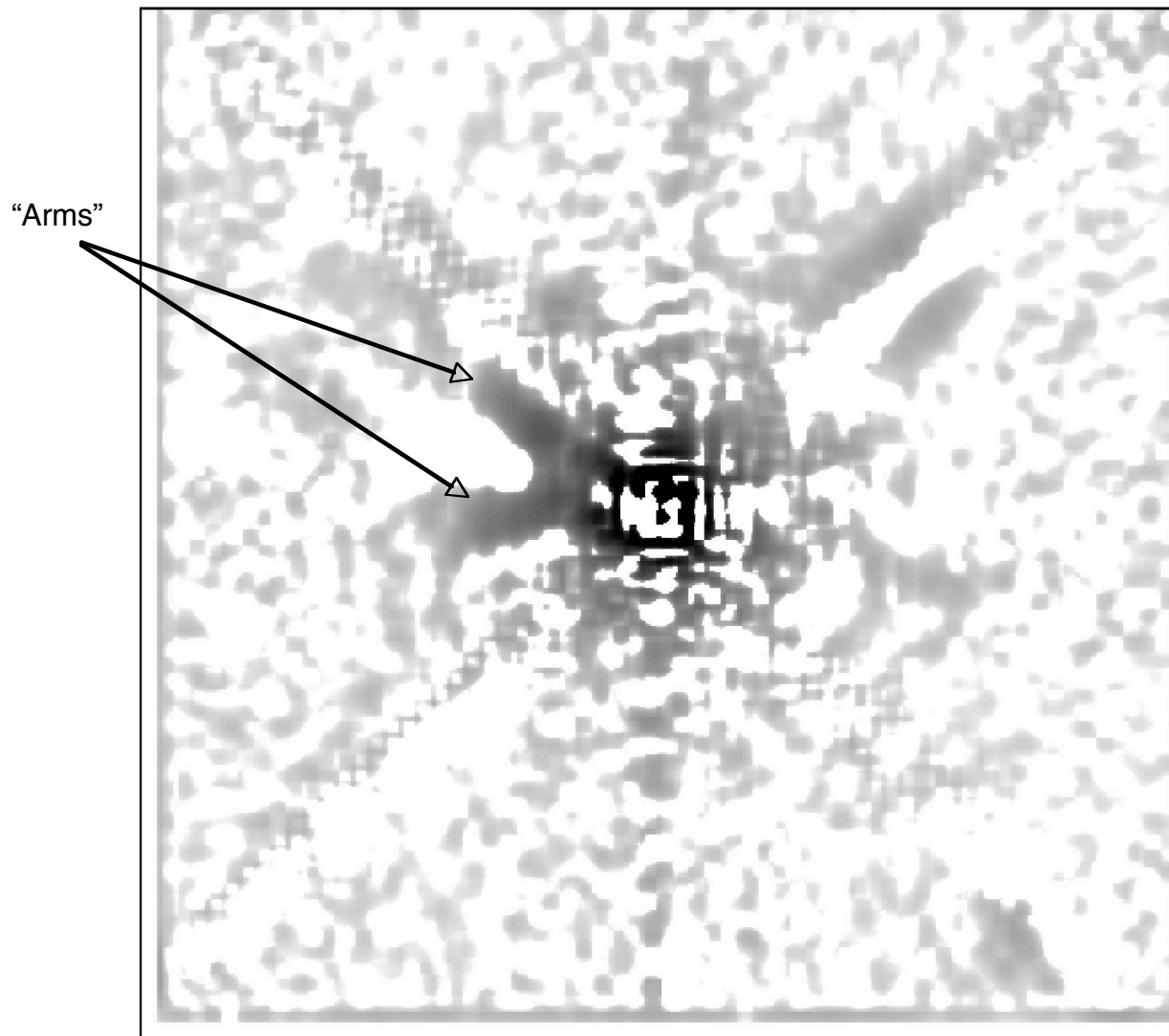


Figure 8: A difference image (64 pixels, ~ 2.5 arcsec) comparing the 6th step to the 1st step as the point source is stepped across the “bad droplet #2” in the F225W filter (bottom 2 panels in Figures 6 and 7). Approximately 0.2% of the energy in the point source appears in two “arms” extending from the core.

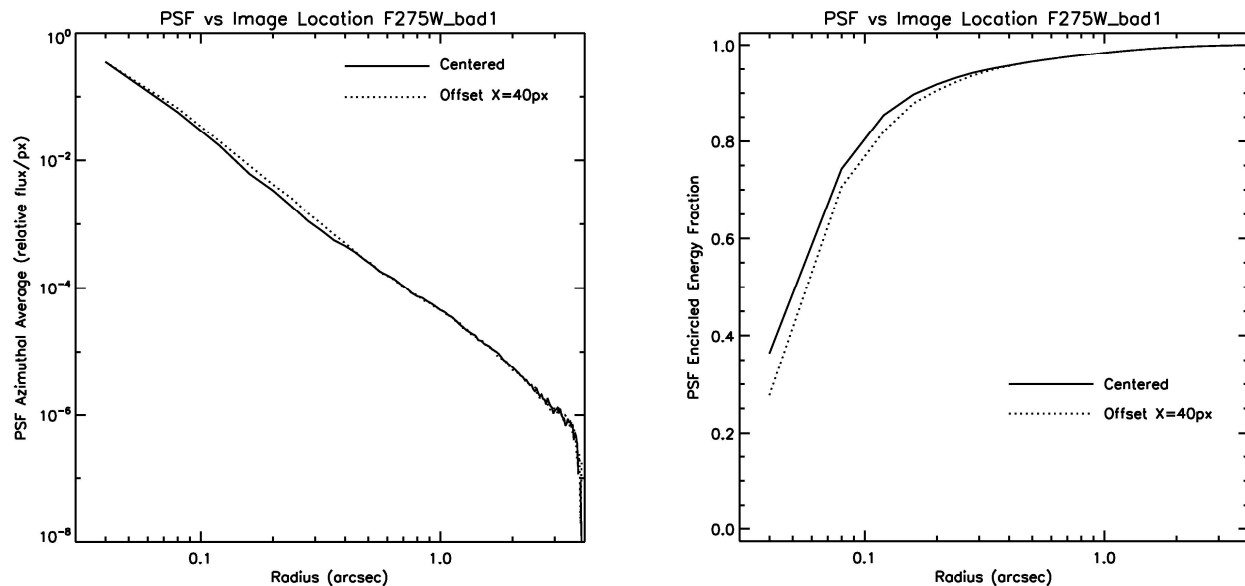


Figure 9: Comparison of the PSF profiles (left panel) and encircled energy curves (right panel) for a point source centered on bad droplet #1, and for a point source offset by 40 pixels from the center of bad droplet #1. As noted in the text, when a point source is centered on a window feature, the f/31 science beam annulus will not intercept the window feature, and the point source should be imaged as if it were in a clean part of the window. With the 40 pixel offset, the annulus intercepts the window feature, and the photometric measurements of a point source in the F275W filter showed a fluctuation of several percent in small-aperture photometry (see Figure A2). The measurements of the PSF and encircled energy are consistent with those photometric results. In the left panel, the PSF profile shows an enhancement at radii of 0.1 to 0.4 arcsec when the point source is offset by 40 pixels from the window feature, as light is redirected from the core to the near wings. In the right panel, the encircled energy curve for the offset position is lower than the centered position until the radius exceeds 0.4 arcsec, beyond which the curves agree.

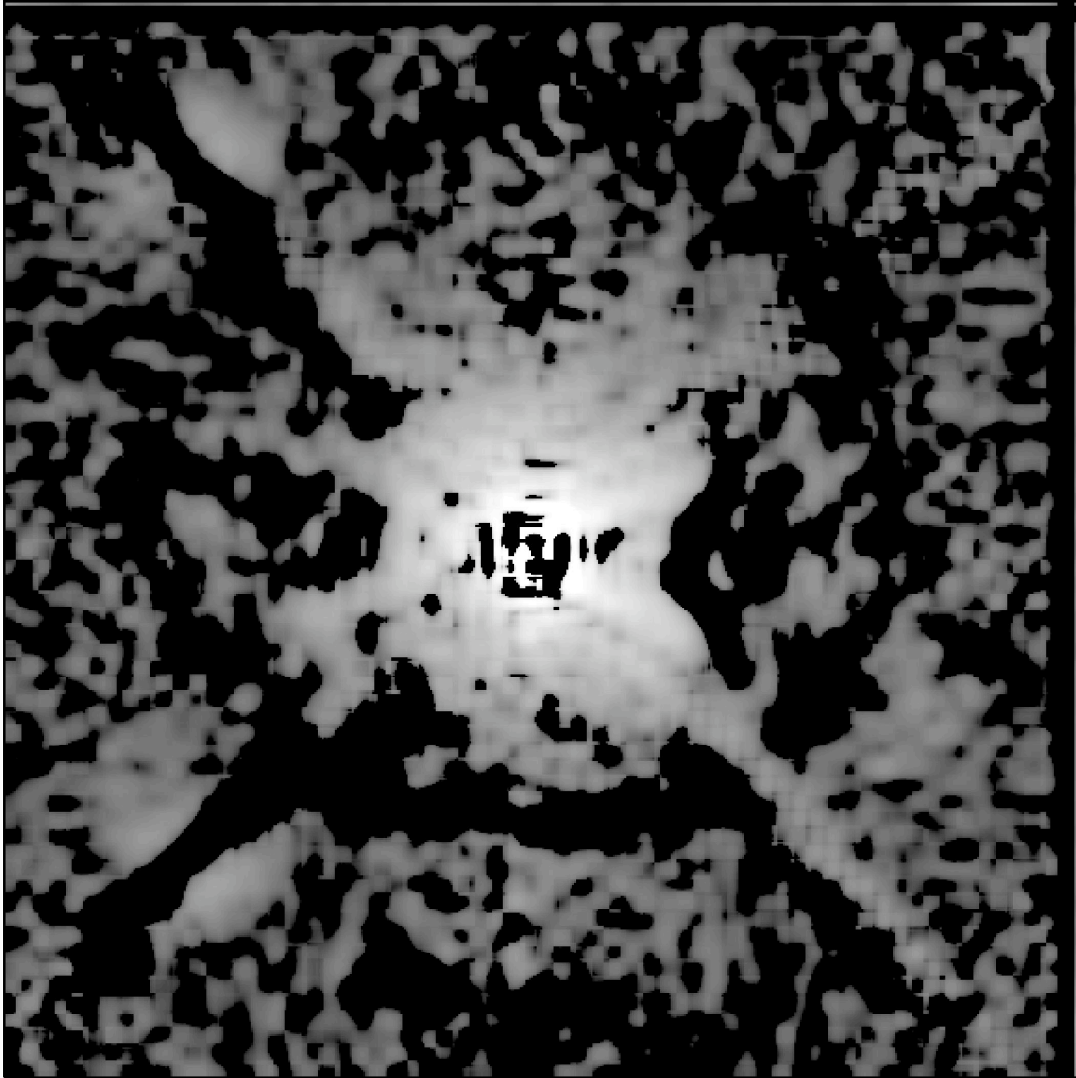


Figure 10: A difference image (64 pixels; ~ 2.5 arcsec) constructed from the two point source images characterized in Figure 9 (i.e., subtracting the image of the centered point source from the image of the offset point source, in the vicinity of bad droplet #1). Approximately 2% of the light appears in a halo immediately outside the core of the PSF, graphically demonstrating that the light is redirected from the PSF core to the near wings, as shown in Figure 9, and as implied by the 3-pixel and 10-pixel photometry at these positions.

Stability of the Droplets

We characterized the stability of the droplets by taking ratios of flat-field images separated in time. In ratios of flat-field images taken with external illumination (i.e., matching the f/31 beam that will be used by observers), the variation in the ratio is at the sub-1% level, and very difficult to see even in the UV, where the effects of the droplets are strongest (Figures 11 and 12). These external flat-field images imply the droplet features are very stable, as expected for inorganic mineral deposits on the window.

In flat-field images obtained with the internal calibration subsystem, the story is murkier. As noted earlier, the internal calibration subsystem has an $f/\#$ approximately two orders of magnitude higher than the science beam. This highly collimated beam amplifies the effects of the droplets. As a result, the ratios of internal flat-field images are more structured. One source of problems is the fact that the images can saturate in the bright cores of the droplet features. Another complication is that tiny changes in alignment will move the features slightly in the internal flat-field images; because the droplets features have such strong contrast, any resulting mis-registration will be reflected in the flat-field ratios. This can be seen in Figures 13 and 14, which show the ratio of two flat-field images taken only 18 days apart with the internal deuterium lamp and the F225W filter.

Because the ratios of flat-field images with the appropriate f/31 beam show very little structure, we expect stable flat-field behavior for science observations when WFC3 is in orbit. However, our ability to monitor the evolution of the flats via the internal calibration system will be complicated (and at some level compromised) by the high $f/\#$ of the calibration system. We will pursue alternative strategies for monitoring the flat-field behavior on orbit (e.g., Earth flats, sky flats), but options in the UV are very limited, and this is where the droplets have their strongest effects.

Summary

The WFC3 UVIS channel has a large number of flat-field features due to material on the outer window of the detector. In external flat-field images, these features have a strength of approximately $\pm 0.5\%$. When a point source is stepped across these features, the photometry can suffer from systematic errors ranging from sub-1% (usually) to a few percent (rarely), and these errors are not corrected by flat-fielding. The changes in PSF profile are consistent with these photometric variations, such that flux in the core is redistributed to the near wings. These flat field features appear to be stable in time, although our baseline in testing is only 2 months.

For the observer, the best strategy for mitigating the flat-field features will be an appropriate dither pattern. Although there are positions within a flat-field feature that cause systematic errors at the level of a few percent in point source photometry, other positions separated by 20 to 40 pixels show much smaller errors, suggesting that dithers on this scale would be sufficient for most photometric programs. To ensure a point source does not hit a particular feature twice requires larger dithers of approximately 100 pixels, which is the typical diameter of these features. It is also worth repeating that quadrant A has the lowest density of features. This is also the quadrant where the window is furthest from the detector surface, so a given window feature will subtend a lower fraction of the PSF beam in this quadrant, minimizing its effects. Thus observers may want to place their target (or the most important region of an extended target) in quadrant A, if the droplets are a concern.

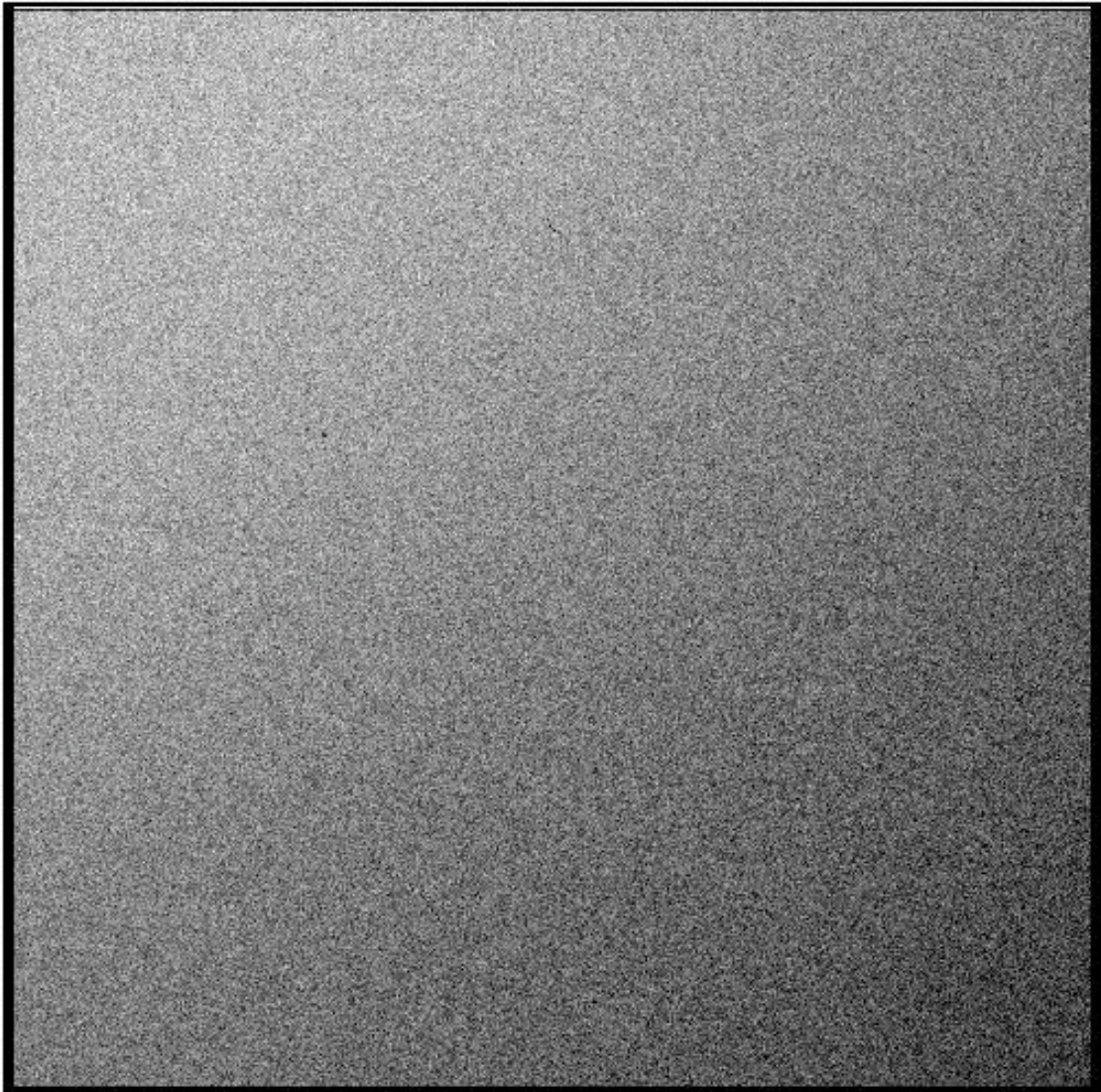


Figure 11: Ratio of two flat-field images in the F225W filter taken with an external deuterium lamp (i.e., matching the $f/\#$ for science observations). The images in this ratio were taken on day 111 and day 55 of 2008. The section of the image shown here is for quadrant D, which has the largest number of droplets. The droplets are not apparent in the ratio (compare with Figure 12). The scale here is $\pm 2\%$.

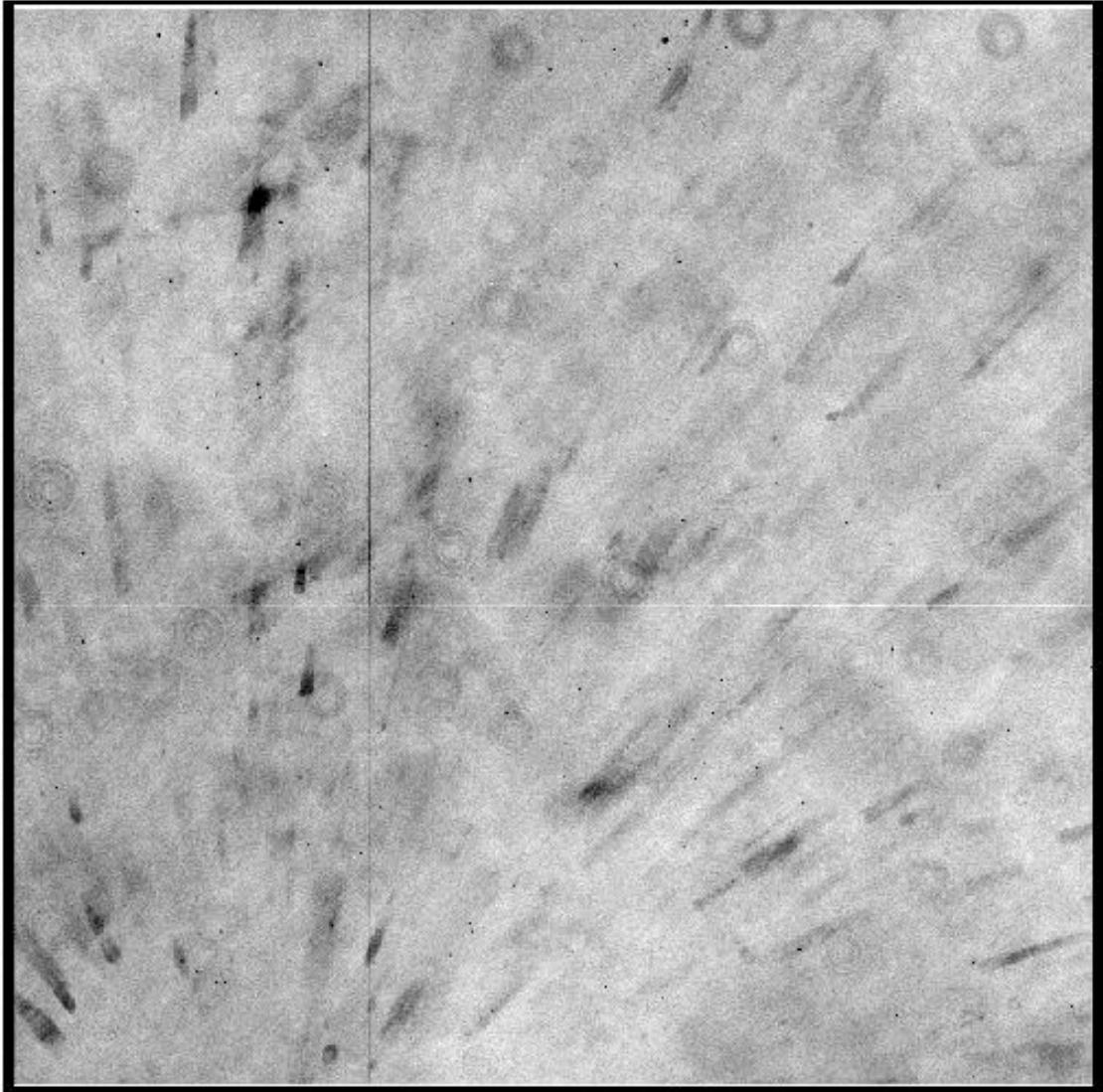


Figure 12: One of the F225W flat-field images used in the ratio of Figure 11. Besides the drop-lets, the UV flats show a lot of structure, but none of this structure is apparent in Figure 11 (i.e., it can be corrected by flat-fielding). The scale here is $\pm 5\%$.



Figure 13: The ratio of two flat-field images obtained with the internal deuterium lamp through the F225W filter, 18 days apart. As noted previously, the highly collimated beam of the internal calibration subsystem amplifies the flat-field features. The residual droplet structure in this flat-field image ratio is due to saturation in the cores of some of the droplet features, and due to small changes in deuterium bulb illumination that result in a small mis-registration of the features. The scale here is $\pm 5\%$.

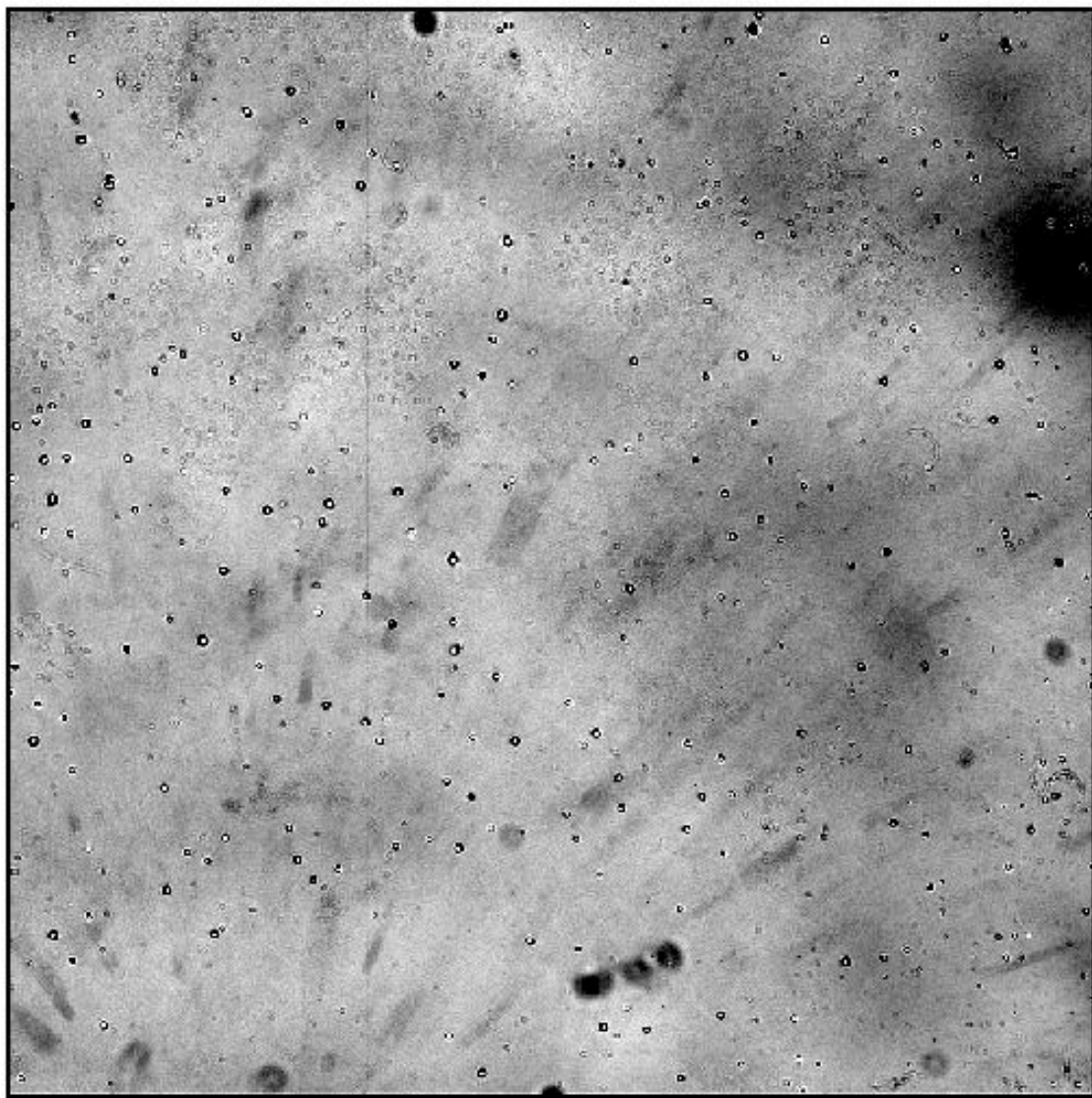


Figure 14: One of the F225W flat-field images used in the ratio of Figure 13. The scale here is $\pm 15\%$.

Appendix A - Photometry Details

In this section we show the detailed photometric results for each of the 6 detector regions sampled.

Each panel in Figures A1 through A30 shows a 210x210 pixel subsection of an external flat-field image in the given filter, with the photometric measurements superimposed. All photometric measurements are normalized to the first measurement in the center of the region, with repeated measurements in the center region shown with an offset for clarity. Measurements that are outliers at the level of 2% or more are highlighted. The left-hand plots show the measurements prior to flat-fielding, while the right-hand plots show the measurements after flat-fielding.

In Figures A31 through A35, we summarize the photometric measurements for each filter, with sorting in flux to make it easier to see outliers. The left-hand plots show the measurements prior to flat-fielding, while the right-hand plots show the measurements after flat-fielding. The top panels show the 3-pixel aperture results, while the bottom panels show the 10-pixel aperture results.

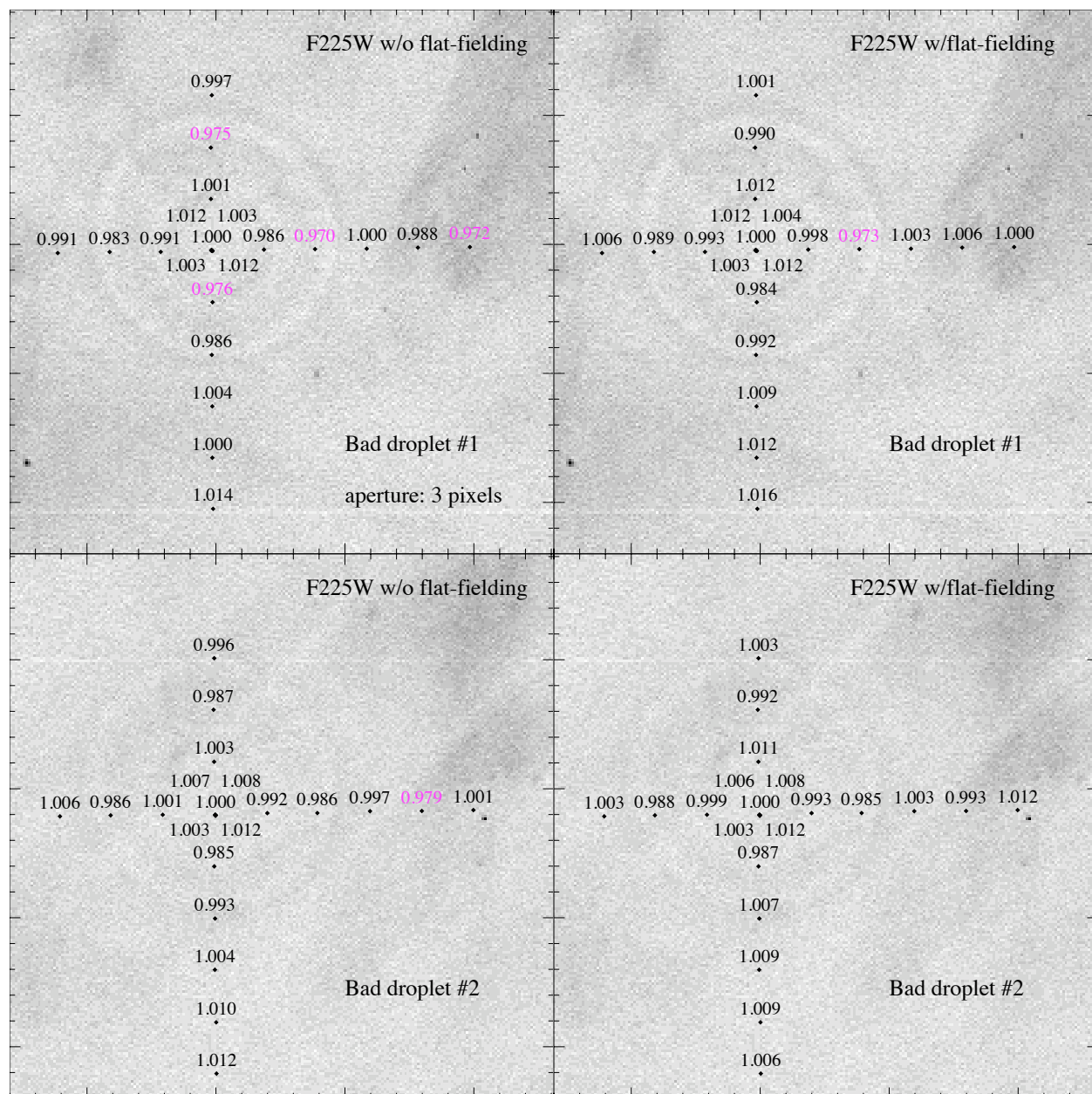


Figure A1: Photometric measurements in the F225W filter in the vicinity of two strong droplet features: bad droplet #1 (top panels) and bad droplet #2 (bottom panels), without flat-fielding (left panels) and with flat-fielding (right panels), using a 3-pixel aperture. The measurements are shown superimposed on the external flat-field image, to indicate where they lie with respect to the flat-field features.

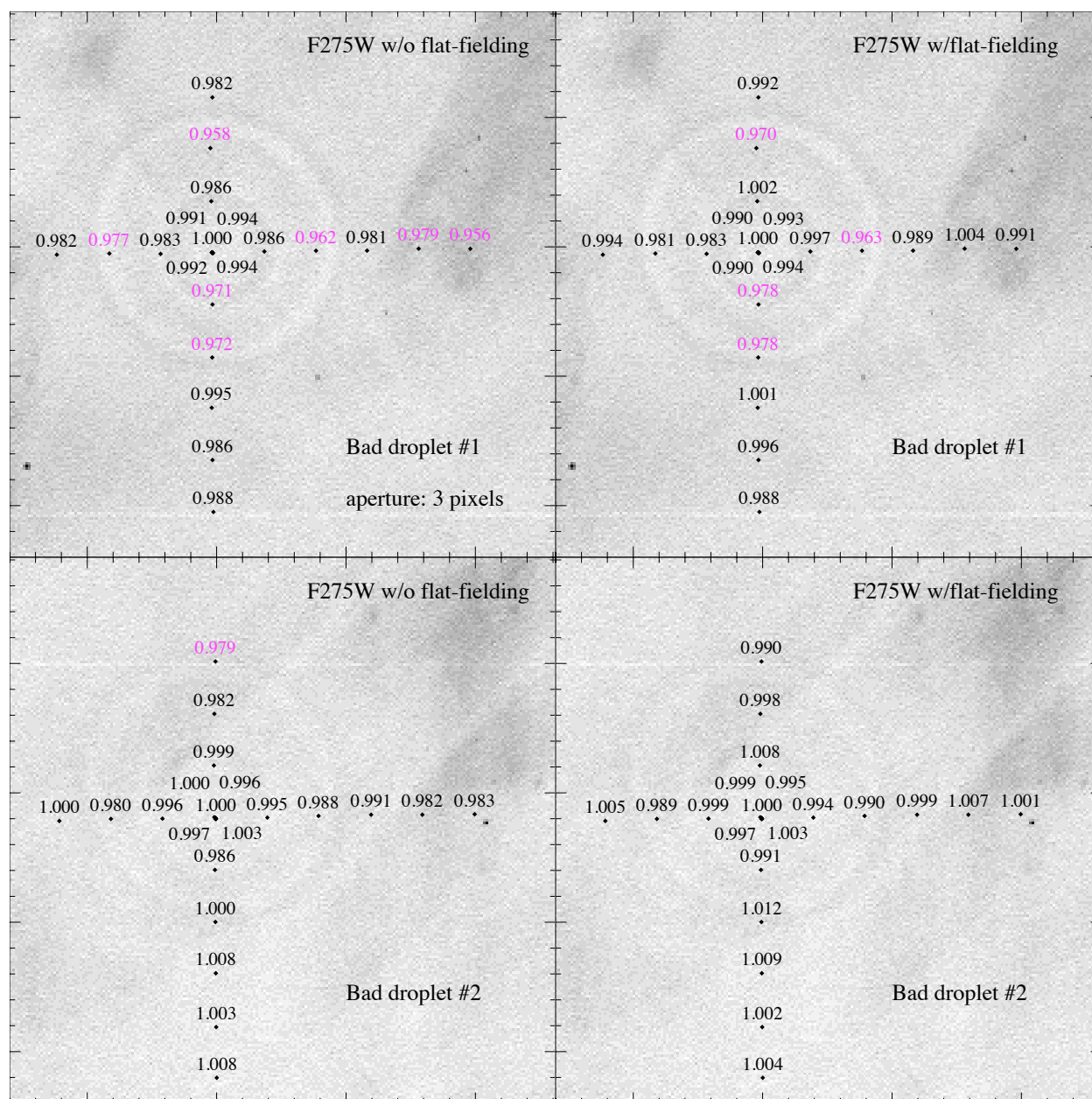


Figure A2: Photometric measurements in the F275W filter in the vicinity of two strong droplet features: bad droplet #1 (top panels) and bad droplet #2 (bottom panels), without flat-fielding (left panels) and with flat-fielding (right panels), using a 3-pixel aperture. The measurements are shown superimposed on the external flat-field image, to indicate where they lie with respect to the flat-field features.

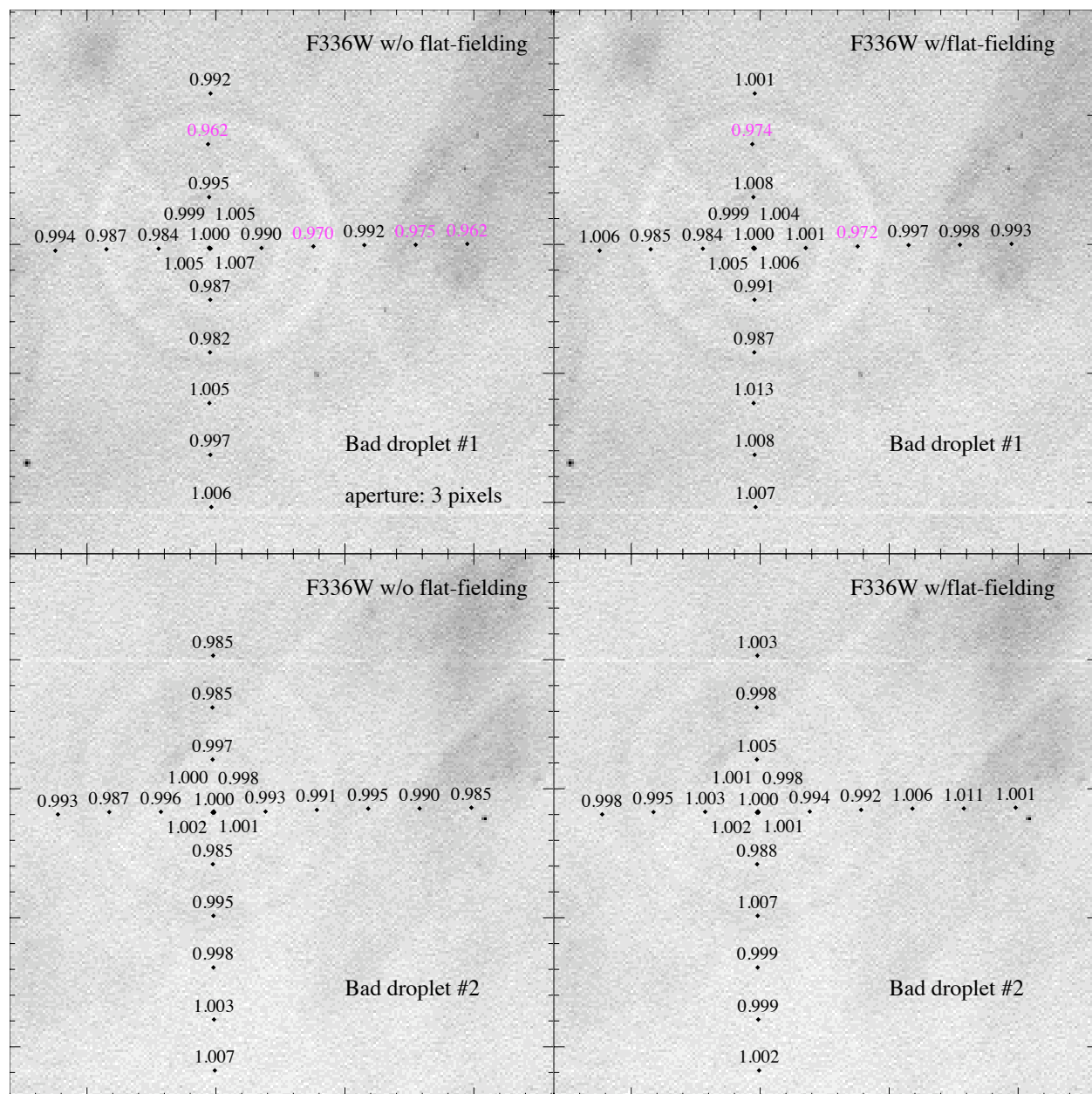


Figure A3: Photometric measurements in the F336W filter in the vicinity of two strong droplet features: bad droplet #1 (top panels) and bad droplet #2 (bottom panels), without flat-fielding (left panels) and with flat-fielding (right panels), using a 3-pixel aperture. The measurements are shown superimposed on the external flat-field image, to indicate where they lie with respect to the flat-field features.

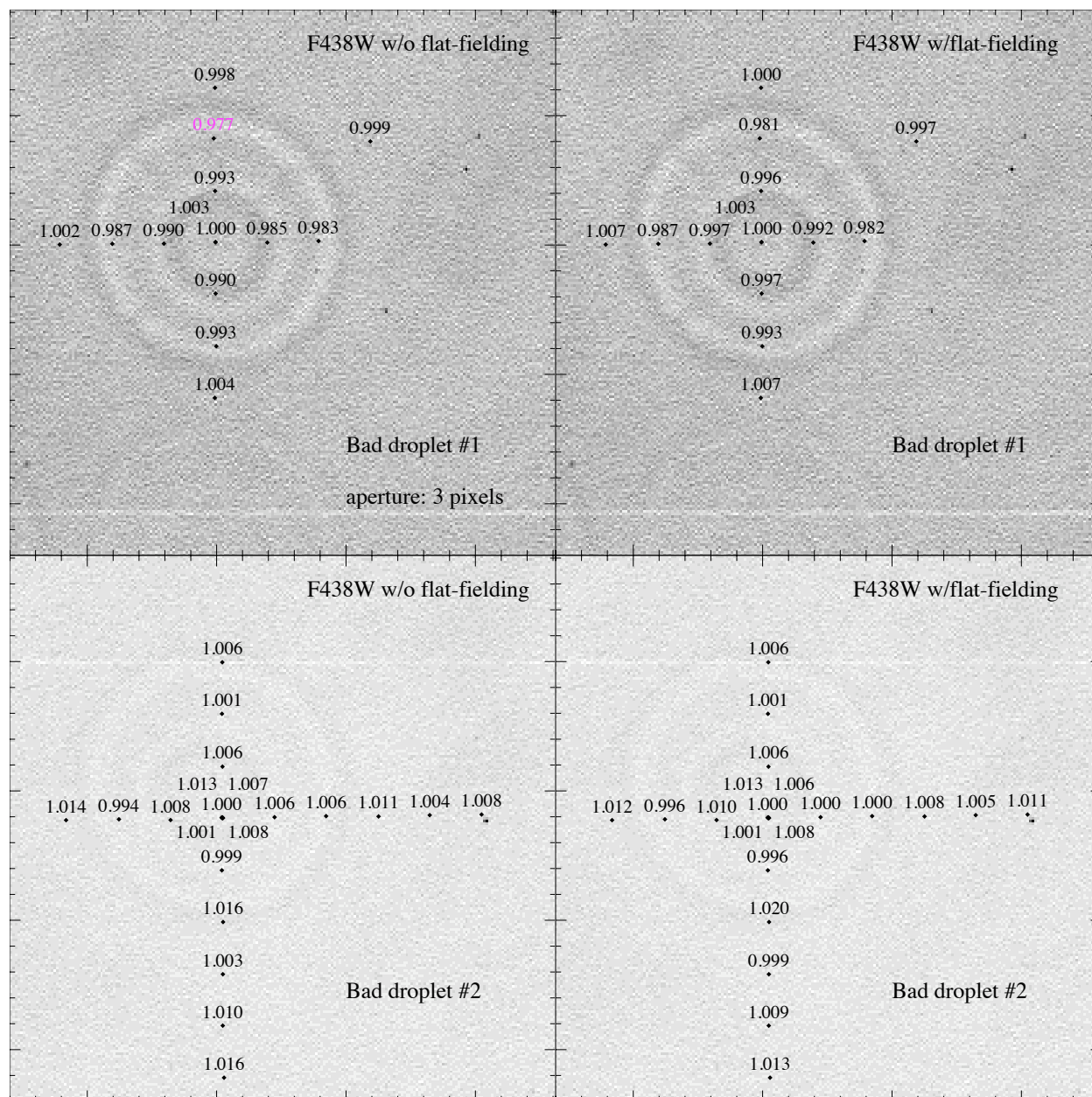


Figure A4: Photometric measurements in the F438W filter in the vicinity of two strong droplet features: bad droplet #1 (top panels) and bad droplet #2 (bottom panels), without flat-fielding (left panels) and with flat-fielding (right panels), using a 3-pixel aperture. The measurements are shown superimposed on the external flat-field image, to indicate where they lie with respect to the flat-field features.

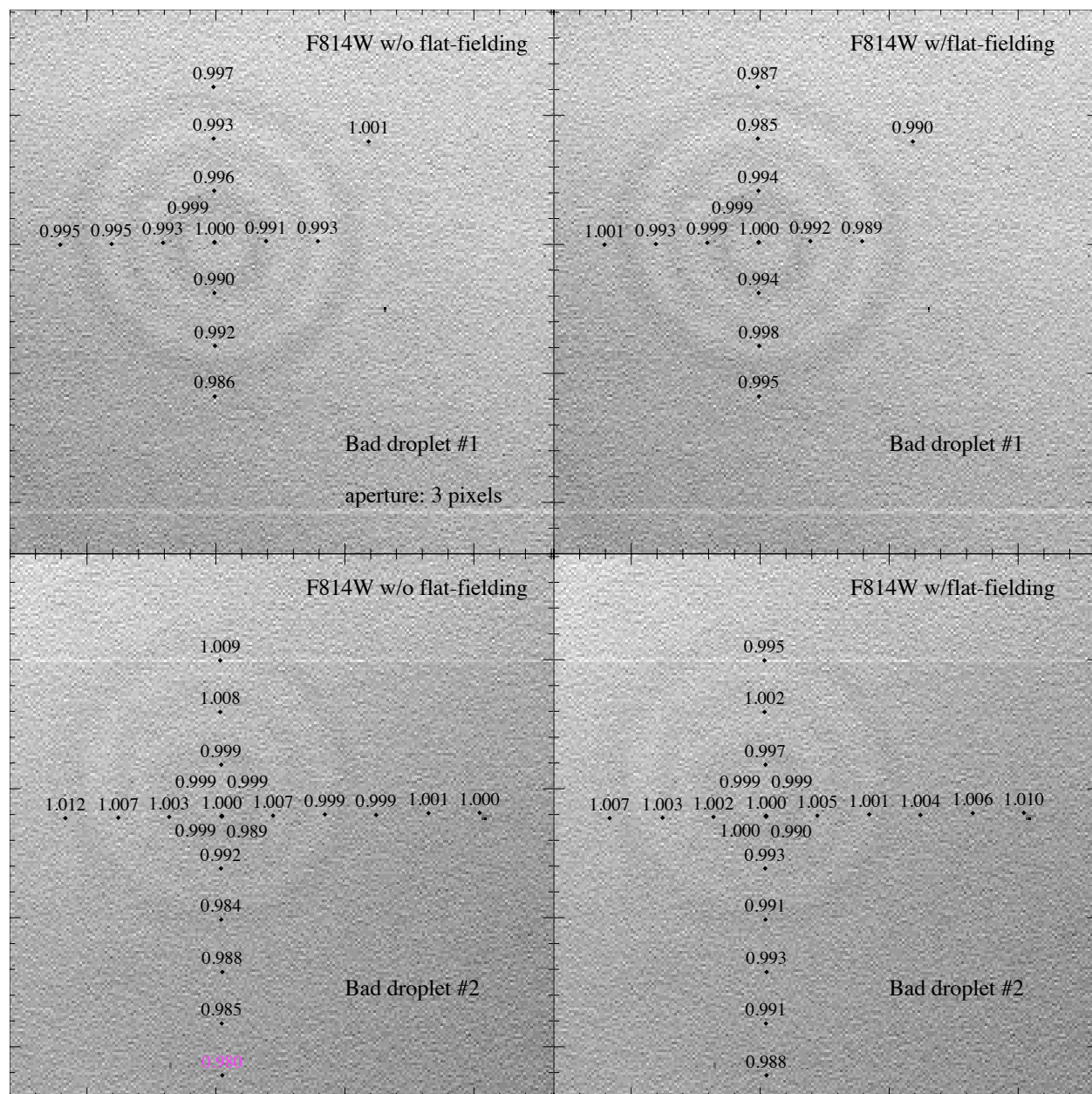


Figure A5: Photometric measurements in the F814W filter in the vicinity of two strong droplet features: bad droplet #1 (top panels) and bad droplet #2 (bottom panels), without flat-fielding (left panels) and with flat-fielding (right panels), using a 3-pixel aperture. The measurements are shown superimposed on the external flat-field image, to indicate where they lie with respect to the flat-field features.

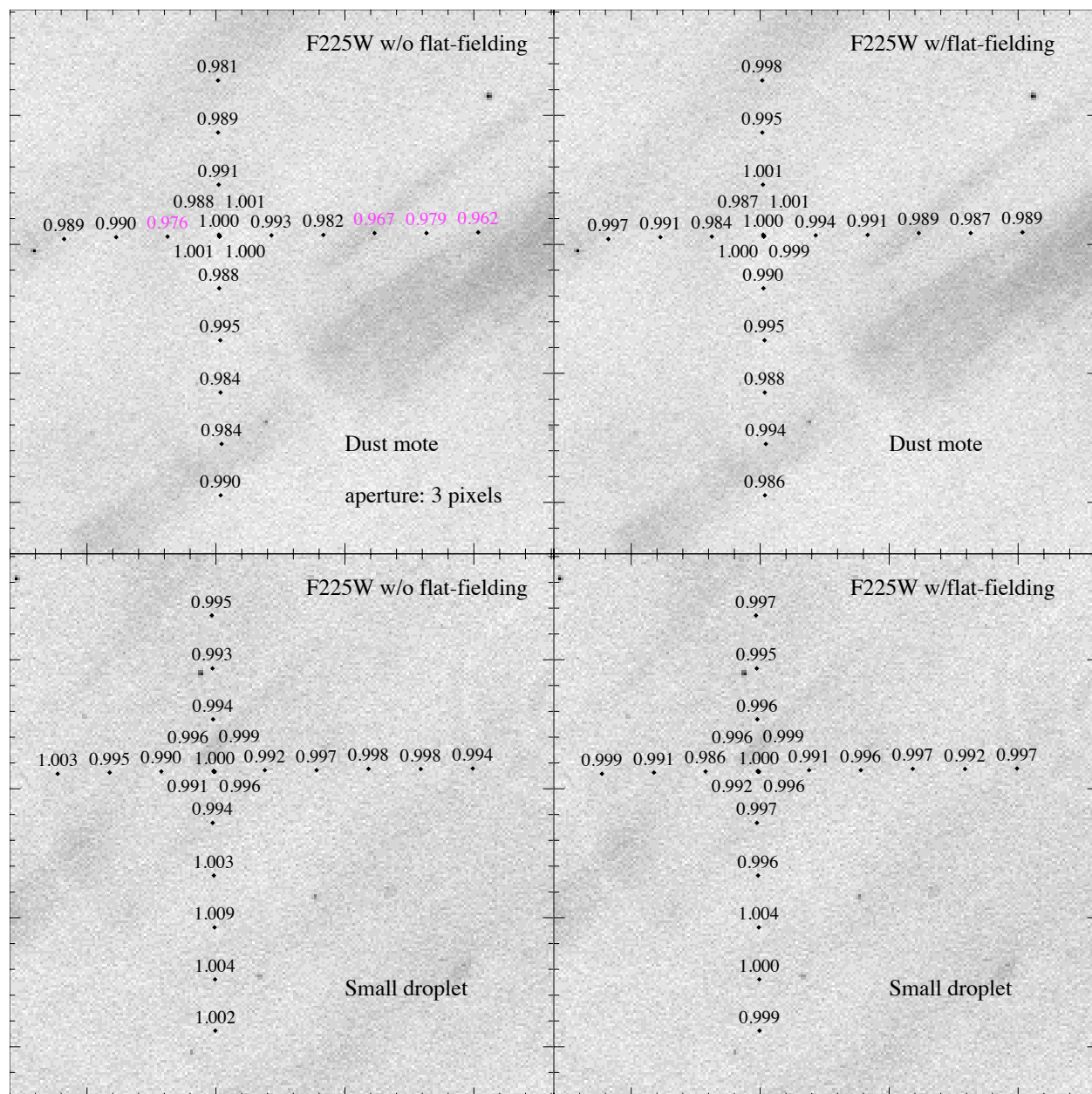


Figure A6: Photometric measurements in the F225W filter in the vicinity of two weak features: a dust mote (top panels) and a small droplet (bottom panels), without flat-fielding (left panels) and with flat-fielding (right panels), using a 3-pixel aperture. The measurements are shown superimposed on the external flat-field image, to indicate where they lie with respect to the flat-field features.

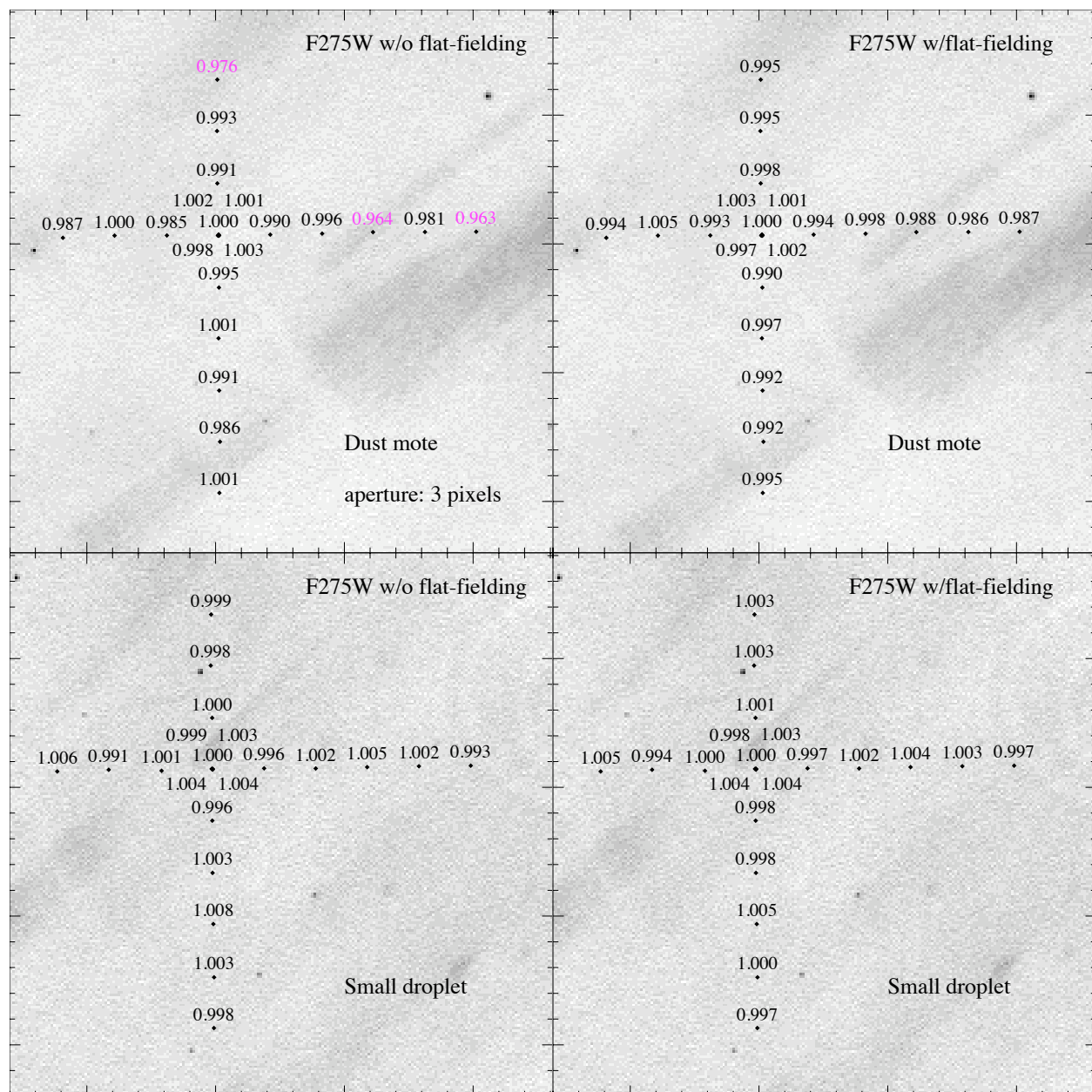


Figure A7: Photometric measurements in the F275W filter in the vicinity of two weak features: a dust mote (top panels) and a small droplet (bottom panels), without flat-fielding (left panels) and with flat-fielding (right panels), using a 3-pixel aperture. The measurements are shown superimposed on the external flat-field image, to indicate where they lie with respect to the flat-field features.

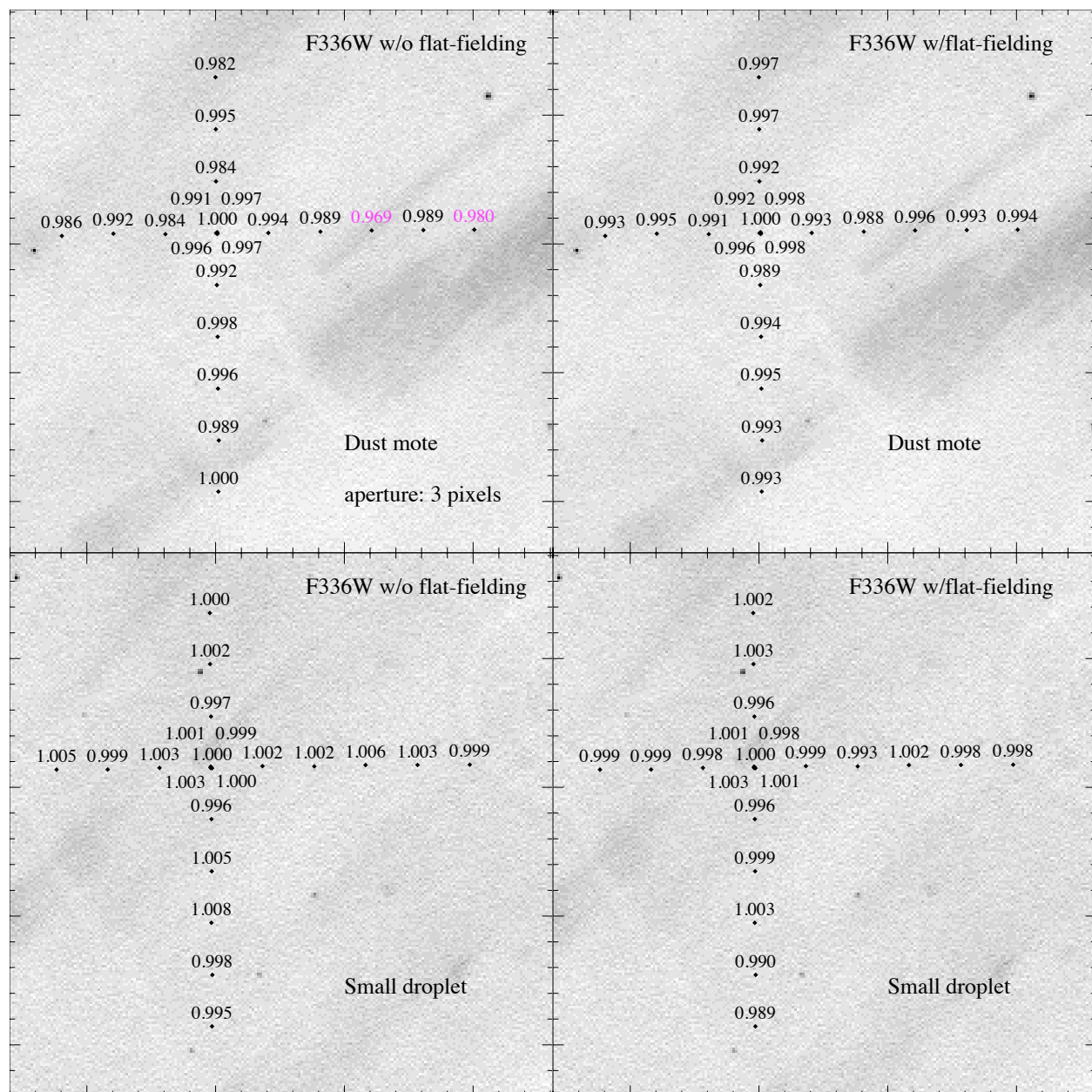


Figure A8: Photometric measurements in the F336W filter in the vicinity of two weak features: a dust mote (top panels) and a small droplet (bottom panels), without flat-fielding (left panels) and with flat-fielding (right panels), using a 3-pixel aperture. The measurements are shown superimposed on the external flat-field image, to indicate where they lie with respect to the flat-field features.

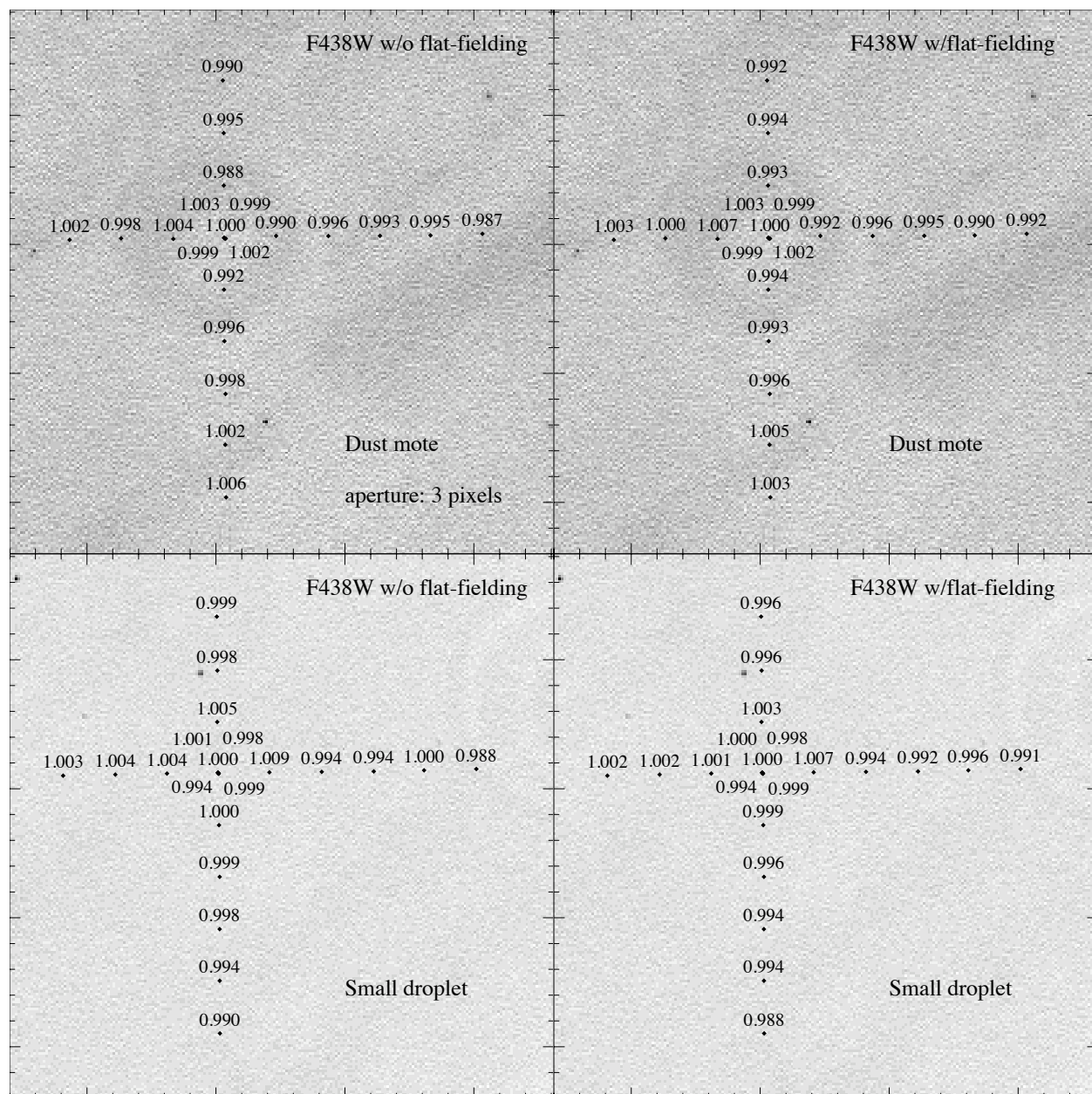


Figure A9: Photometric measurements in the F438W filter in the vicinity of two weak features: a dust mote (top panels) and a small droplet (bottom panels), without flat-fielding (left panels) and with flat-fielding (right panels), using a 3-pixel aperture. The measurements are shown superimposed on the external flat-field image, to indicate where they lie with respect to the flat-field features.

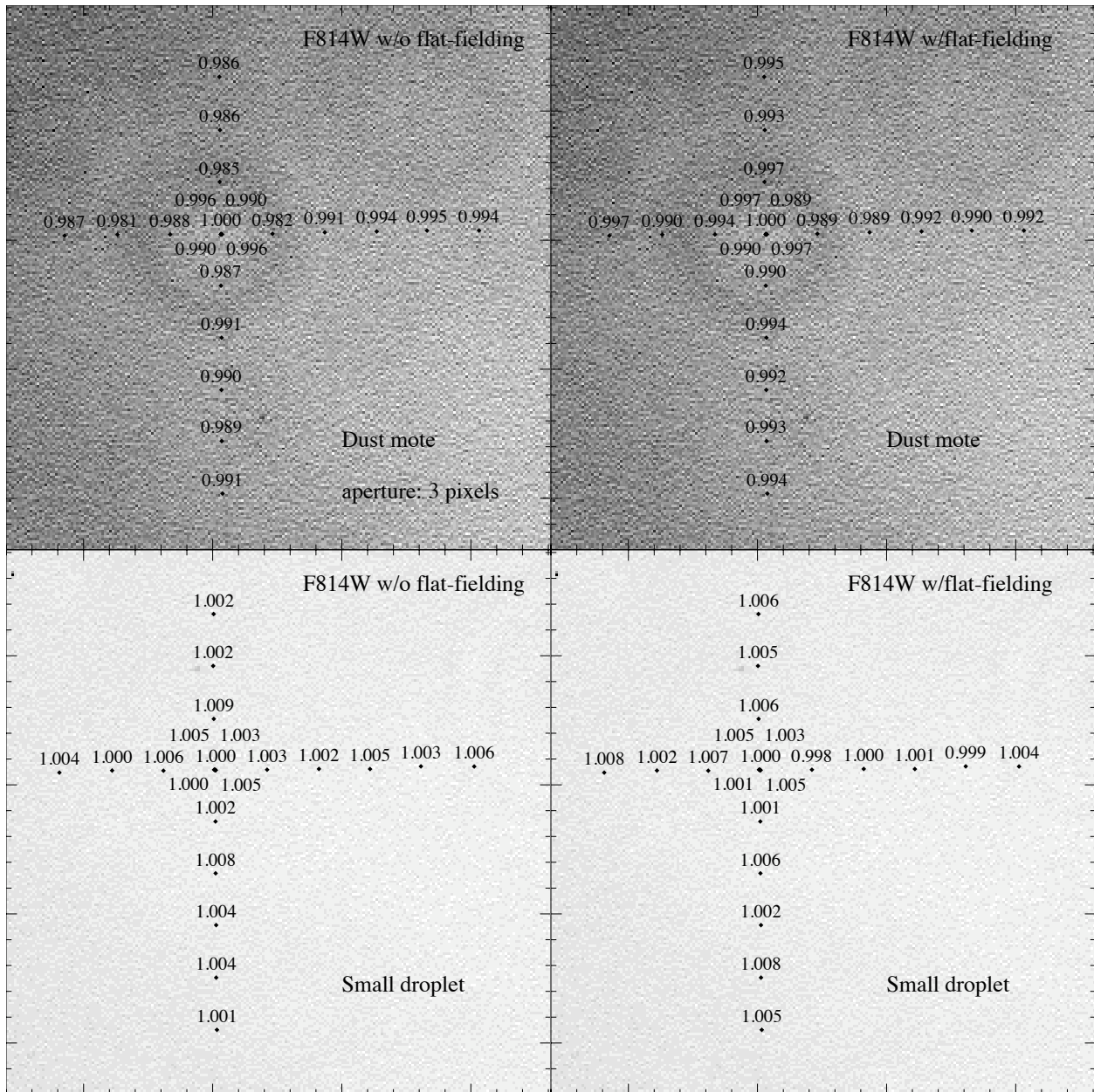


Figure A10: Photometric measurements in the F814W filter in the vicinity of two weak features: a dust mote (top panels) and a small droplet (bottom panels), without flat-fielding (left panels) and with flat-fielding (right panels), using a 3-pixel aperture. The measurements are shown superimposed on the external flat-field image, to indicate where they lie with respect to the flat-field features.

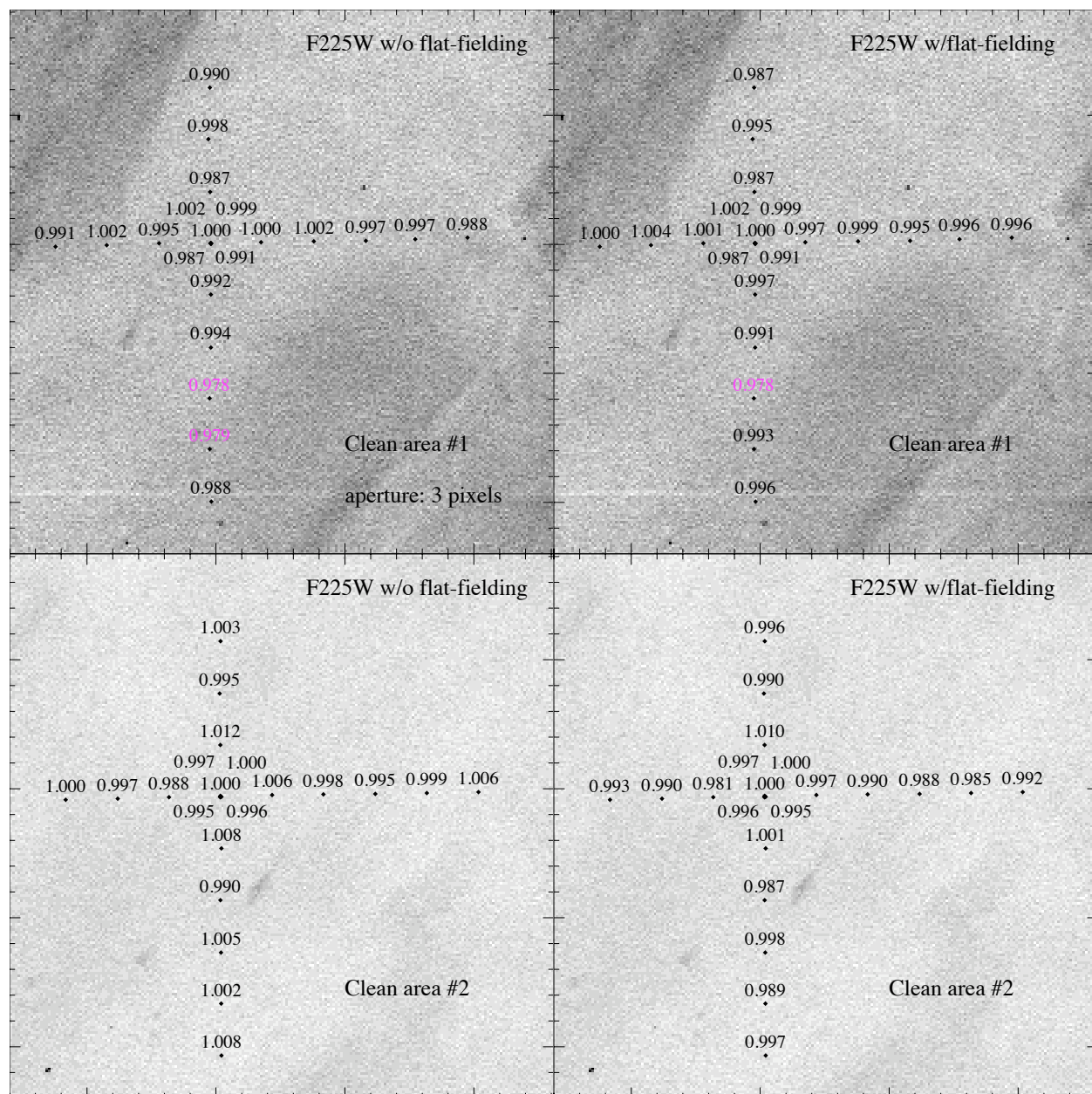


Figure A11: Photometric measurements in the F225W filter in the vicinity of two relatively featureless regions on the detector: clean area #1 (top panels) and clean area #2 (bottom panels), without flat-fielding (left panels) and with flat-fielding (right panels), using a 3-pixel aperture. The measurements are shown superimposed on the external flat-field image, to indicate where they lie with respect to the flat-field features.

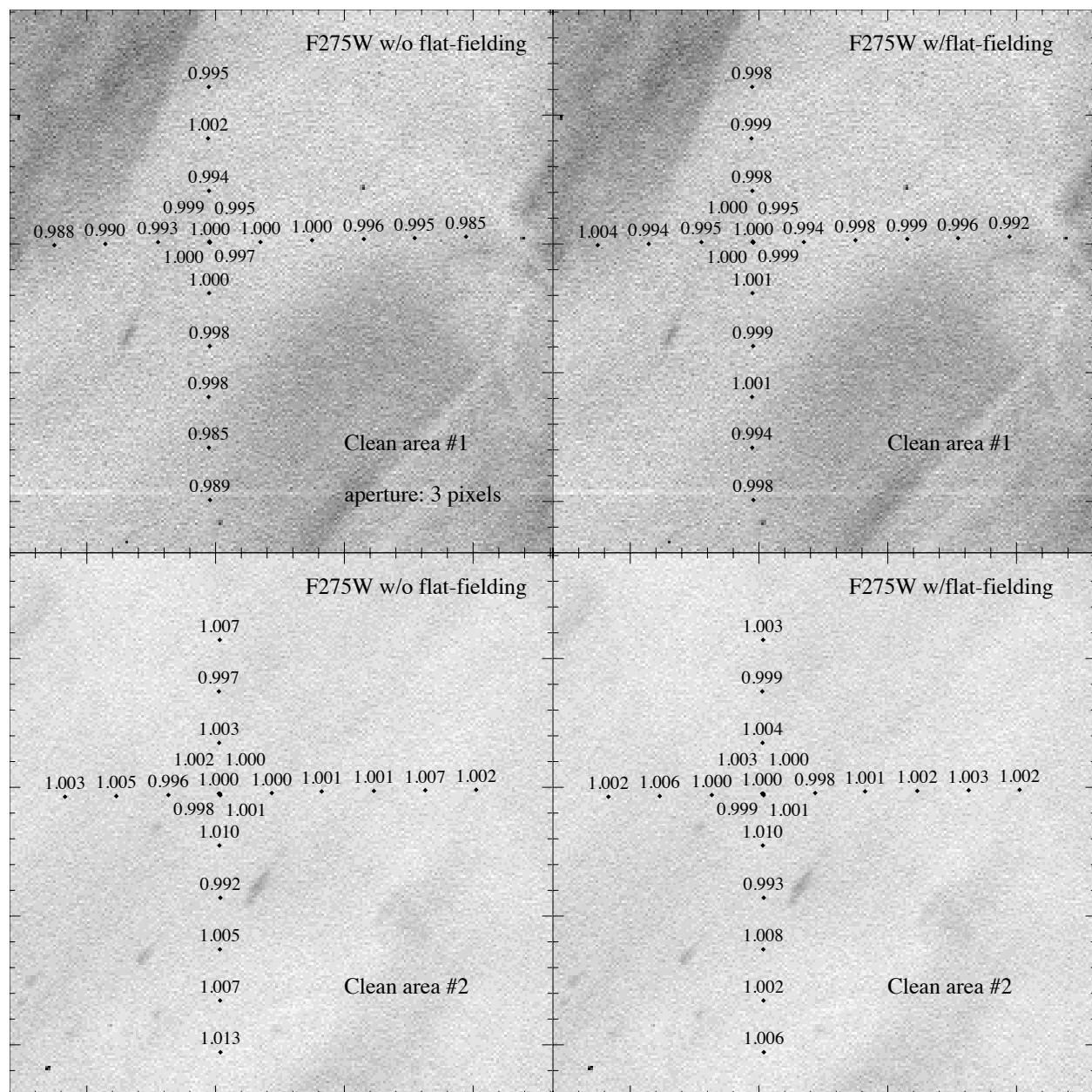


Figure A12: Photometric measurements in the F275W filter in the vicinity of two relatively featureless regions on the detector: clean area #1 (top panels) and clean area #2 (bottom panels), without flat-fielding (left panels) and with flat-fielding (right panels), using a 3-pixel aperture. The measurements are shown superimposed on the external flat-field image, to indicate where they lie with respect to the flat-field features.

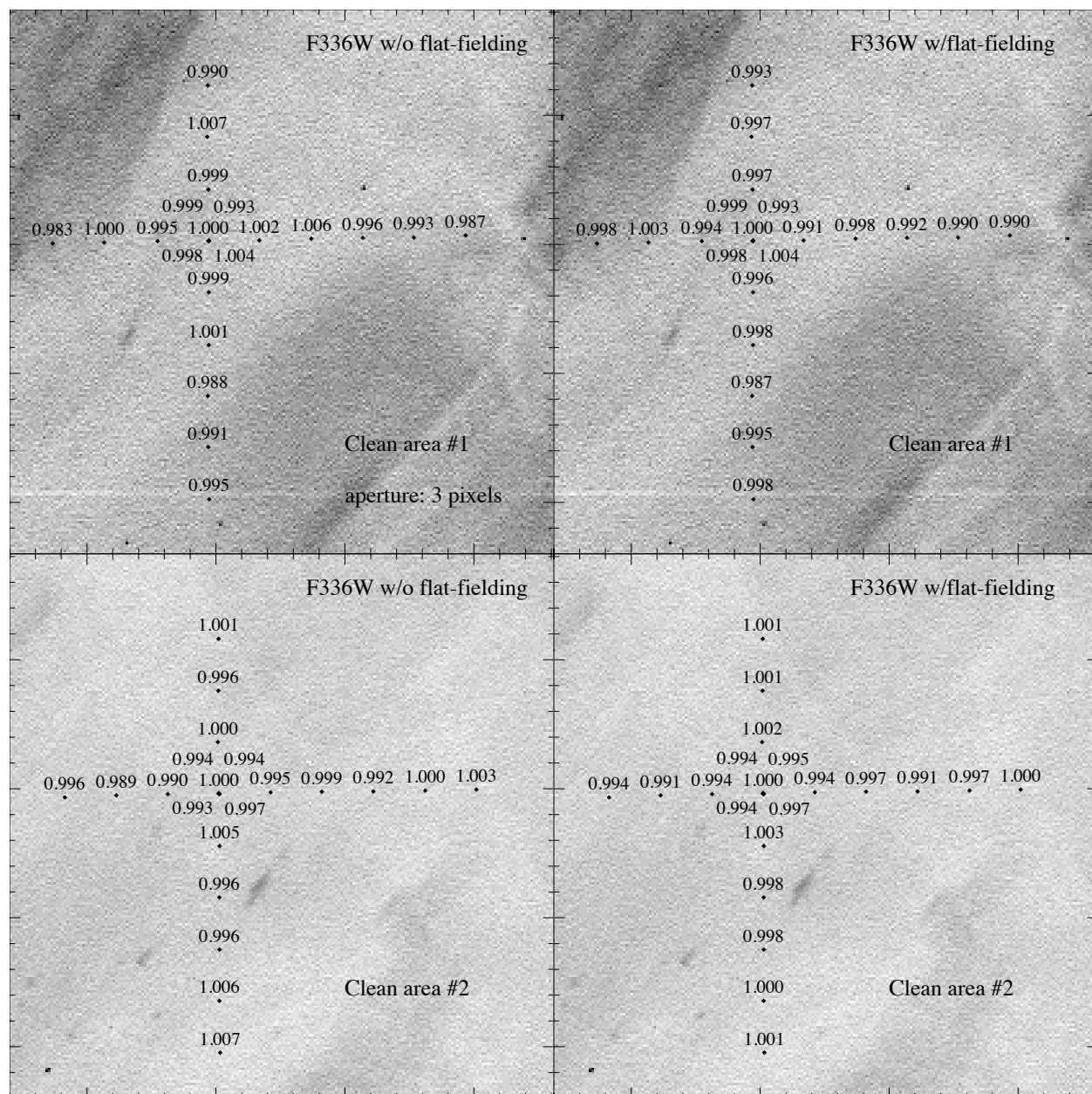


Figure A13: Photometric measurements in the F336W filter in the vicinity of two relatively featureless regions on the detector: clean area #1 (top panels) and clean area #2 (bottom panels), without flat-fielding (left panels) and with flat-fielding (right panels), using a 3-pixel aperture. The measurements are shown superimposed on the external flat-field image, to indicate where they lie with respect to the flat-field features.

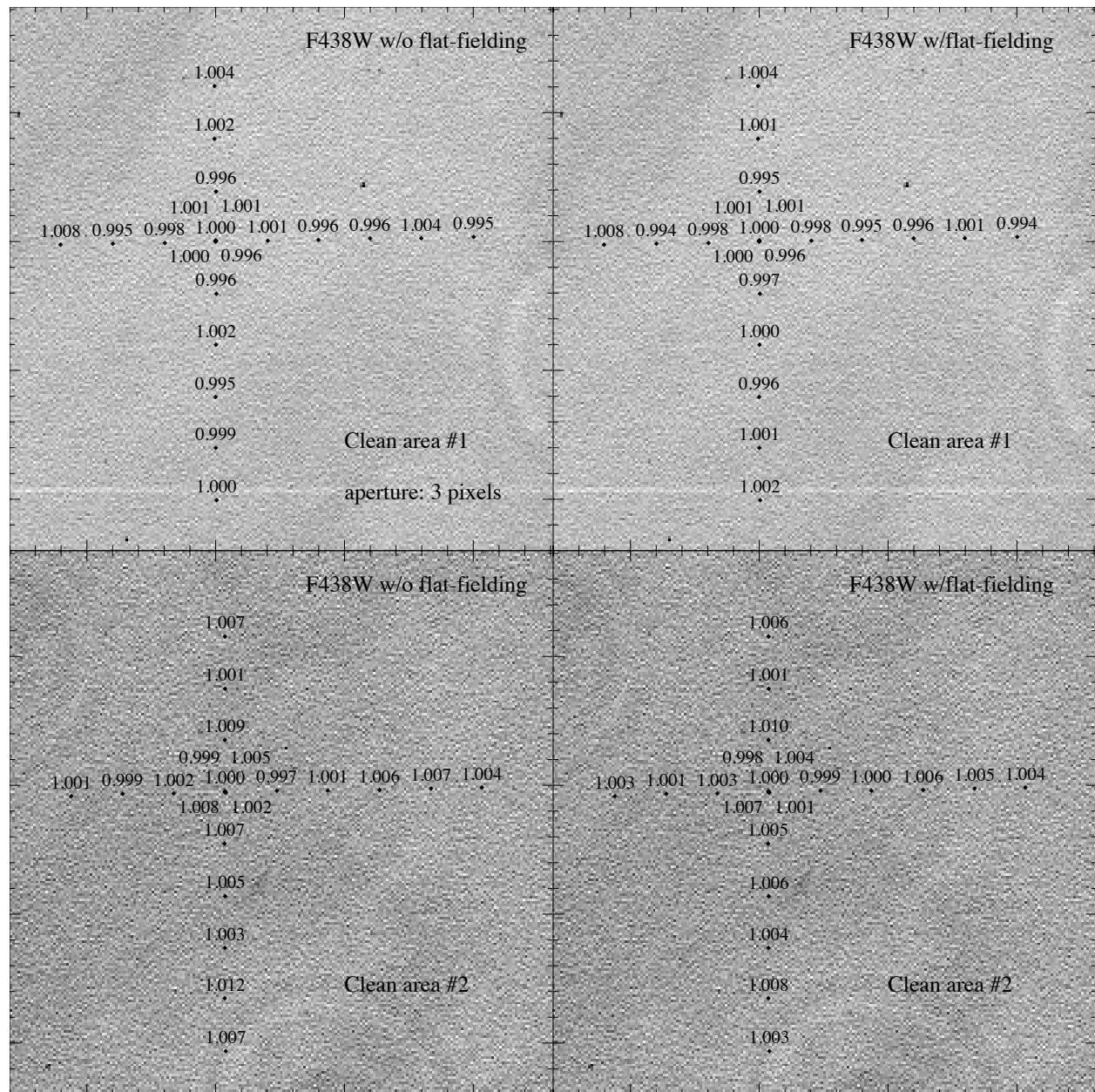


Figure A14: Photometric measurements in the F438W filter in the vicinity of two relatively featureless regions on the detector: clean area #1 (top panels) and clean area #2 (bottom panels), without flat-fielding (left panels) and with flat-fielding (right panels), using a 3-pixel aperture. The measurements are shown superimposed on the external flat-field image, to indicate where they lie with respect to the flat-field features.

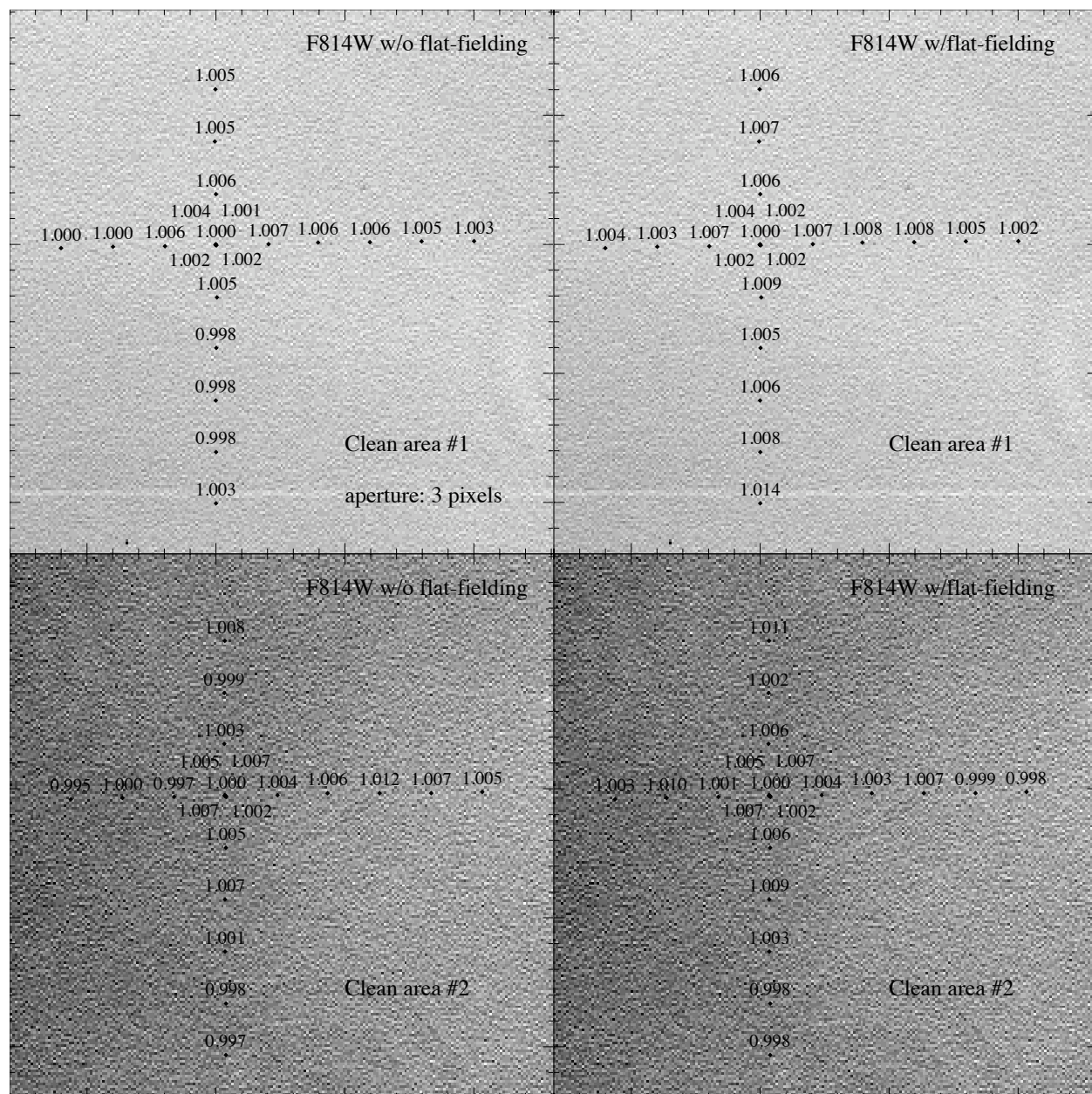


Figure A15: Photometric measurements in the F814W filter in the vicinity of two relatively featureless regions on the detector: clean area #1 (top panels) and clean area #2 (bottom panels), without flat-fielding (left panels) and with flat-fielding (right panels), using a 3-pixel aperture. The measurements are shown superimposed on the external flat-field image, to indicate where they lie with respect to the flat-field features.

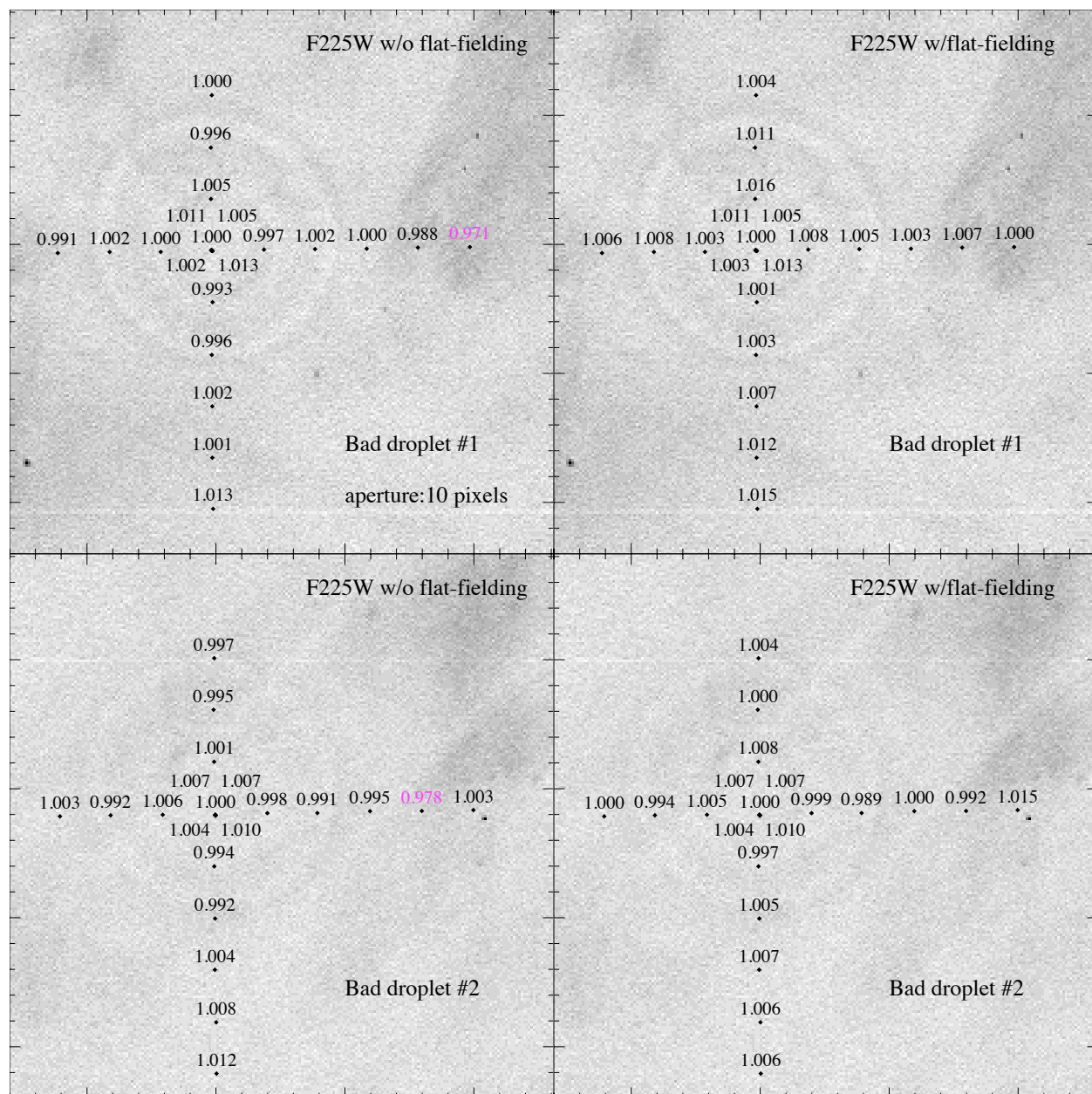


Figure A16: Photometric measurements in the F225W filter in the vicinity of two strong droplet features: bad droplet #1 (top panels) and bad droplet #2 (bottom panels), without flat-fielding (left panels) and with flat-fielding (right panels), using a 10-pixel aperture. The measurements are shown superimposed on the external flat-field image, to indicate where they lie with respect to the flat-field features.

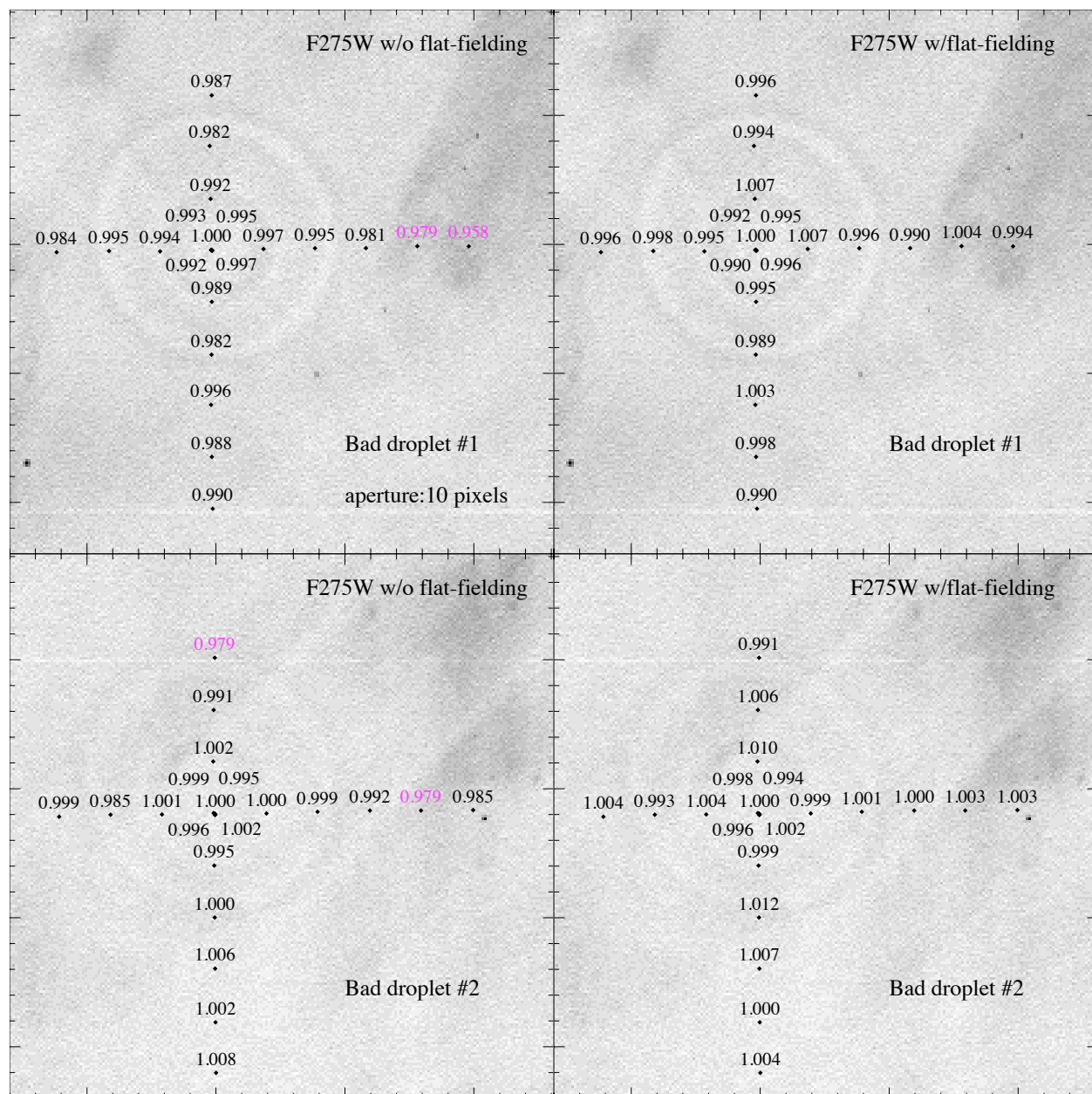


Figure A17: Photometric measurements in the F275W filter in the vicinity of two strong droplet features: bad droplet #1 (top panels) and bad droplet #2 (bottom panels), without flat-fielding (left panels) and with flat-fielding (right panels), using a 10-pixel aperture. The measurements are shown superimposed on the external flat-field image, to indicate where they lie with respect to the flat-field features.

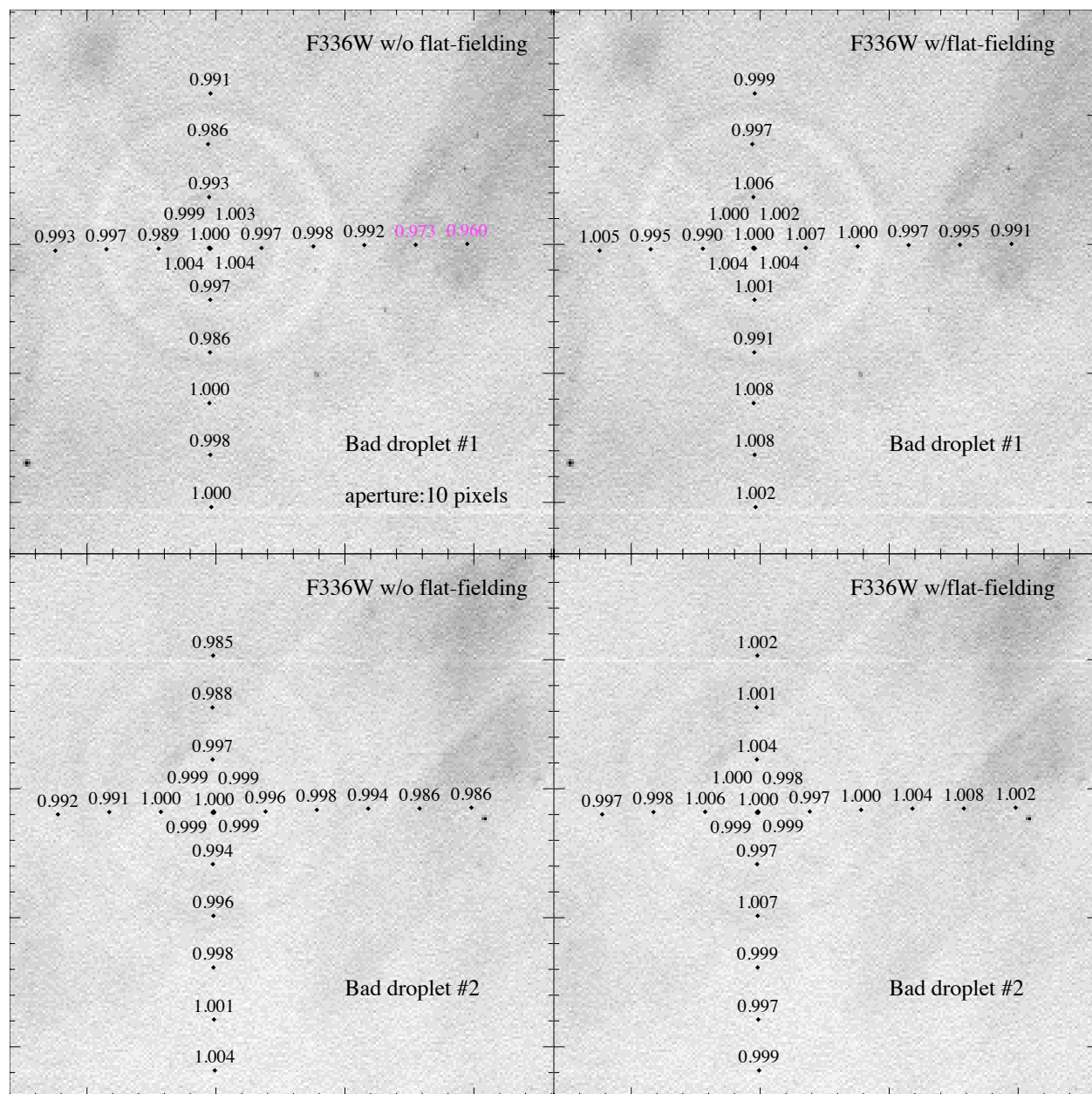


Figure A18: Photometric measurements in the F336W filter in the vicinity of two strong droplet features: bad droplet #1 (top panels) and bad droplet #2 (bottom panels), without flat-fielding (left panels) and with flat-fielding (right panels), using a 10-pixel aperture. The measurements are shown superimposed on the external flat-field image, to indicate where they lie with respect to the flat-field features.

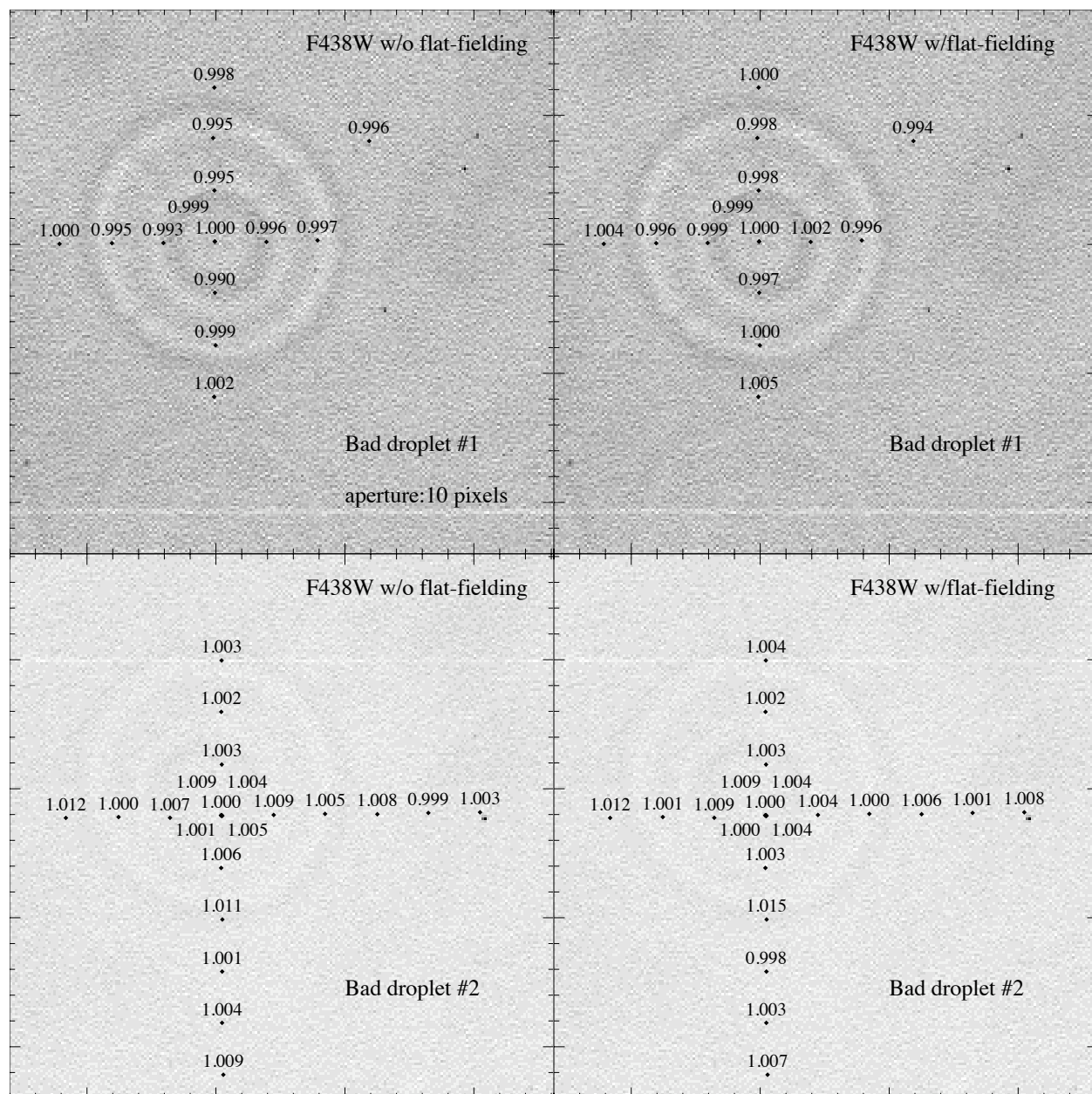


Figure A19: Photometric measurements in the F438W filter in the vicinity of two strong droplet features: bad droplet #1 (top panels) and bad droplet #2 (bottom panels), without flat-fielding (left panels) and with flat-fielding (right panels), using a 10-pixel aperture. The measurements are shown superimposed on the external flat-field image, to indicate where they lie with respect to the flat-field features.

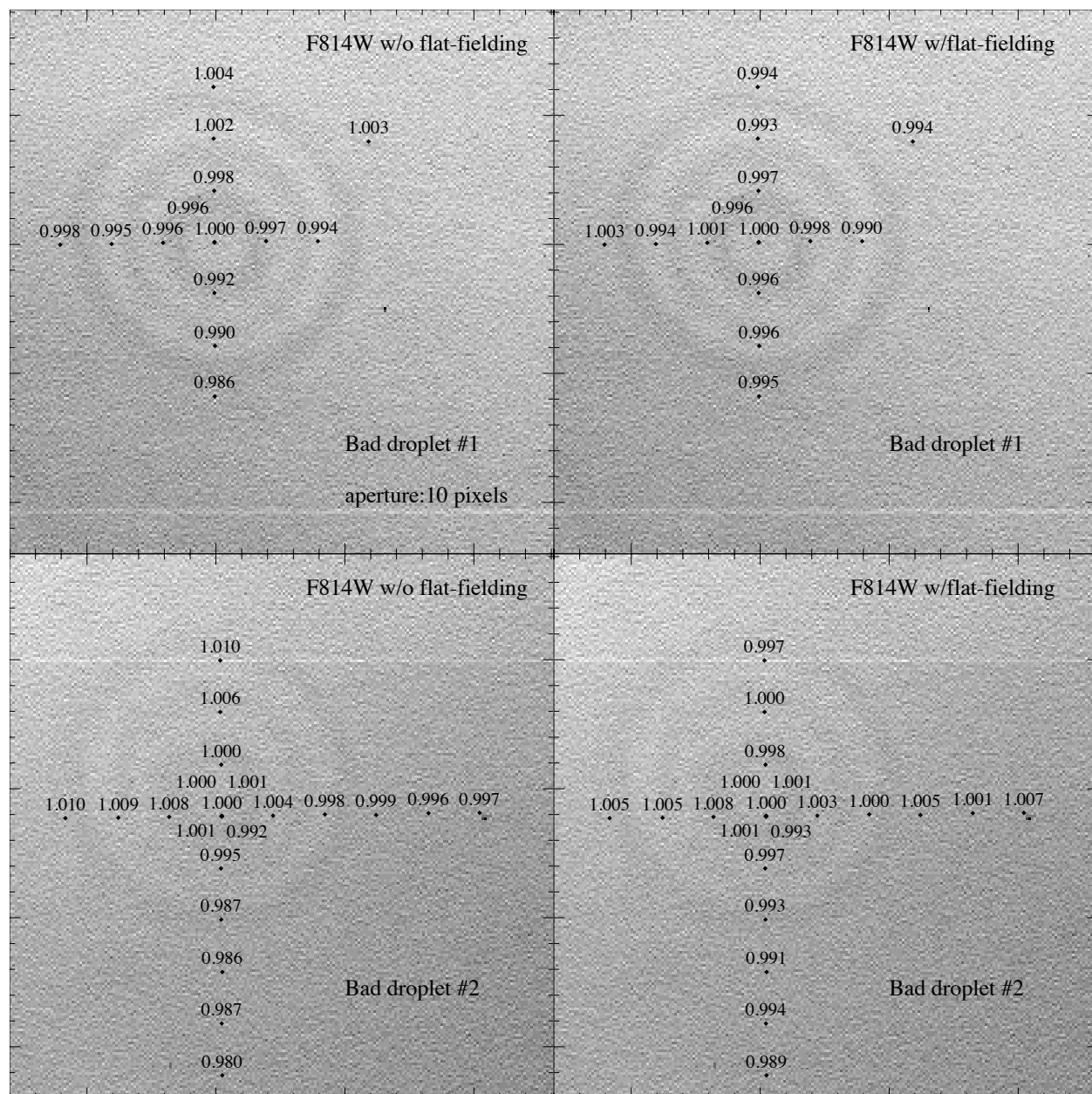


Figure A20: Photometric measurements in the F814W filter in the vicinity of two strong droplet features: bad droplet #1 (top panels) and bad droplet #2 (bottom panels), without flat-fielding (left panels) and with flat-fielding (right panels), using a 10-pixel aperture. The measurements are shown superimposed on the external flat-field image, to indicate where they lie with respect to the flat-field features.

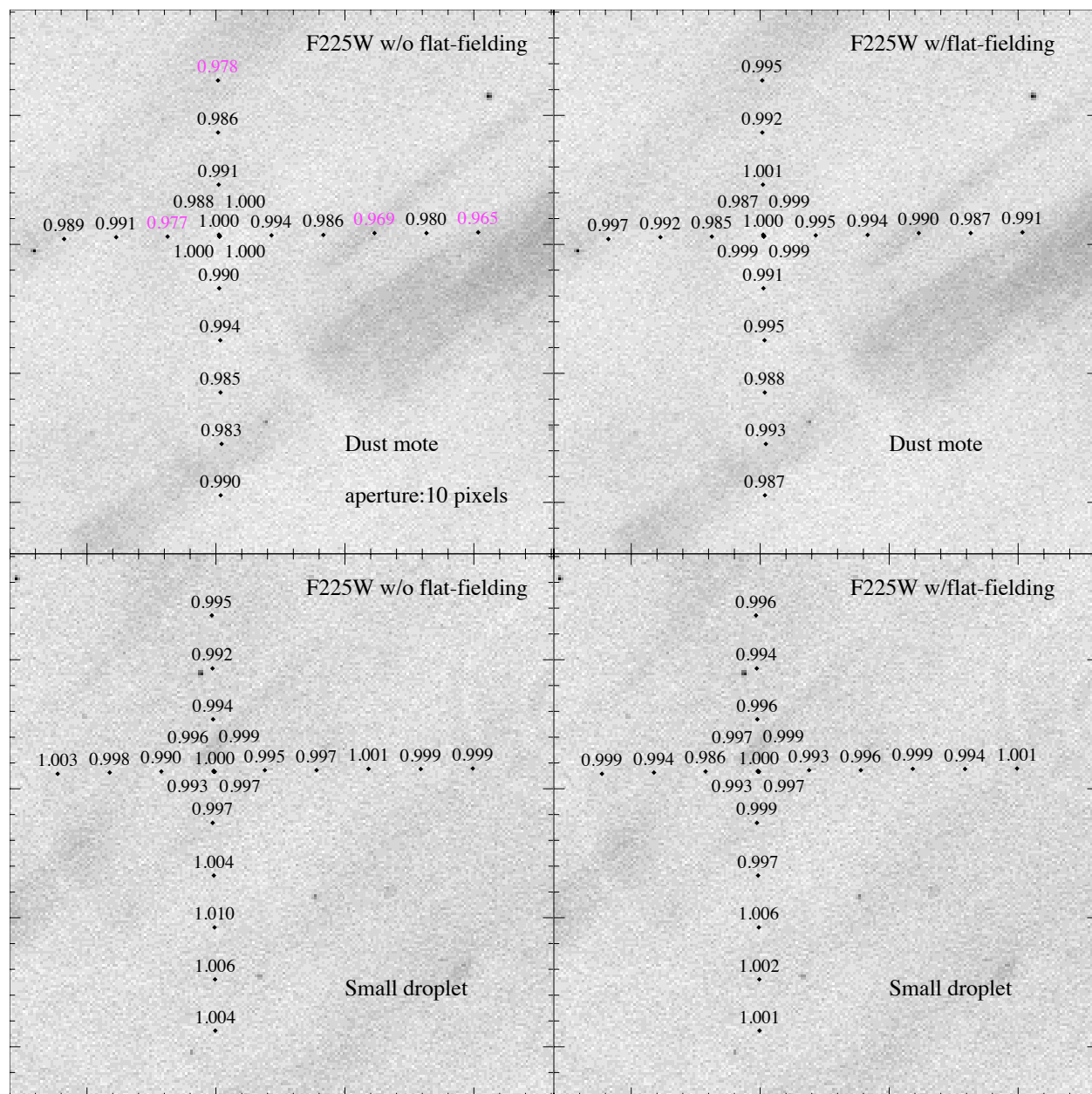


Figure A21: Photometric measurements in the F225W filter in the vicinity of two weak features: a dust mote (top panels) and a small droplet (bottom panels), without flat-fielding (left panels) and with flat-fielding (right panels), using a 10-pixel aperture. The measurements are shown superimposed on the external flat-field image, to indicate where they lie with respect to the flat-field features.

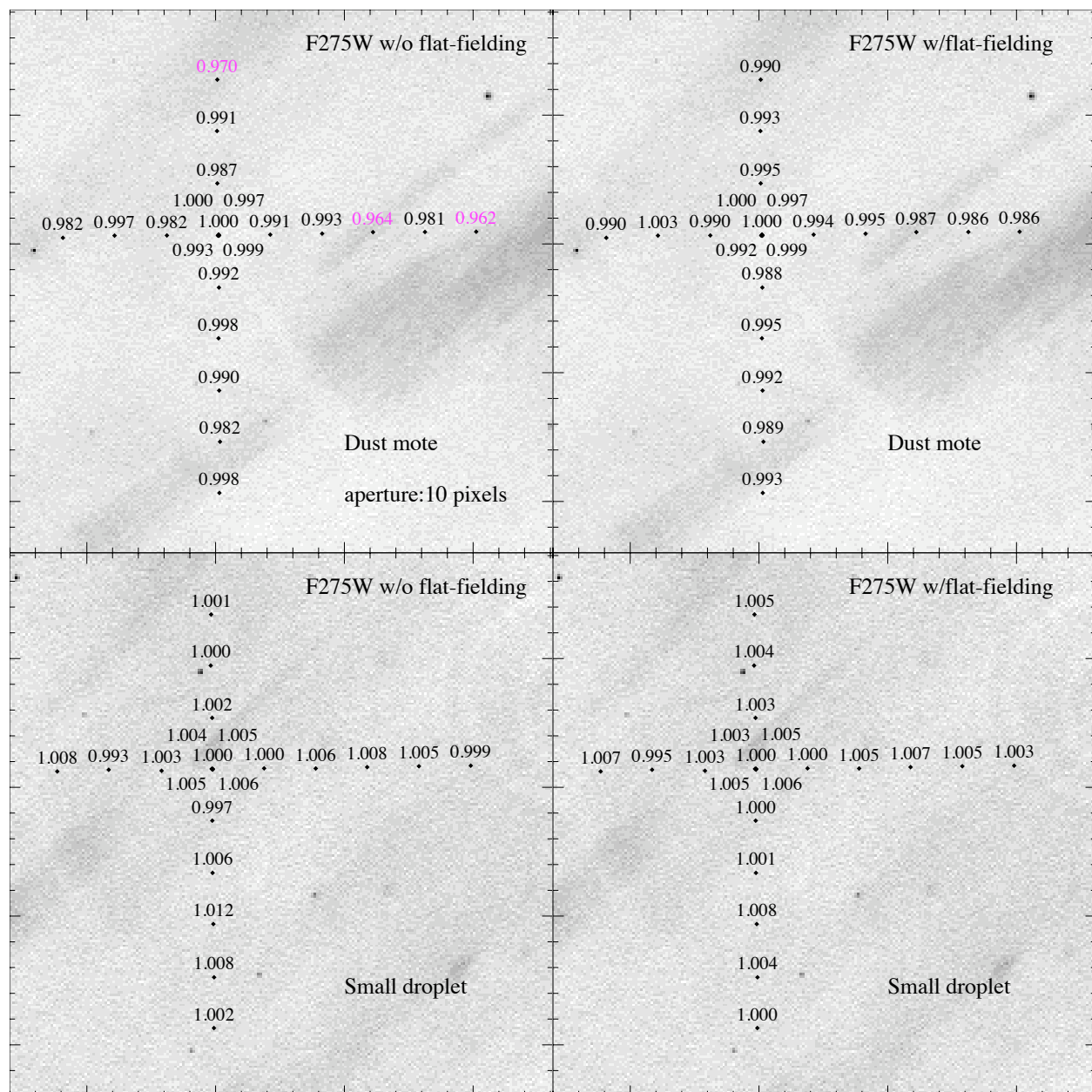


Figure A22: Photometric measurements in the F275W filter in the vicinity of two weak features: a dust mote (top panels) and a small droplet (bottom panels), without flat-fielding (left panels) and with flat-fielding (right panels), using a 10-pixel aperture. The measurements are shown superimposed on the external flat-field image, to indicate where they lie with respect to the flat-field features.

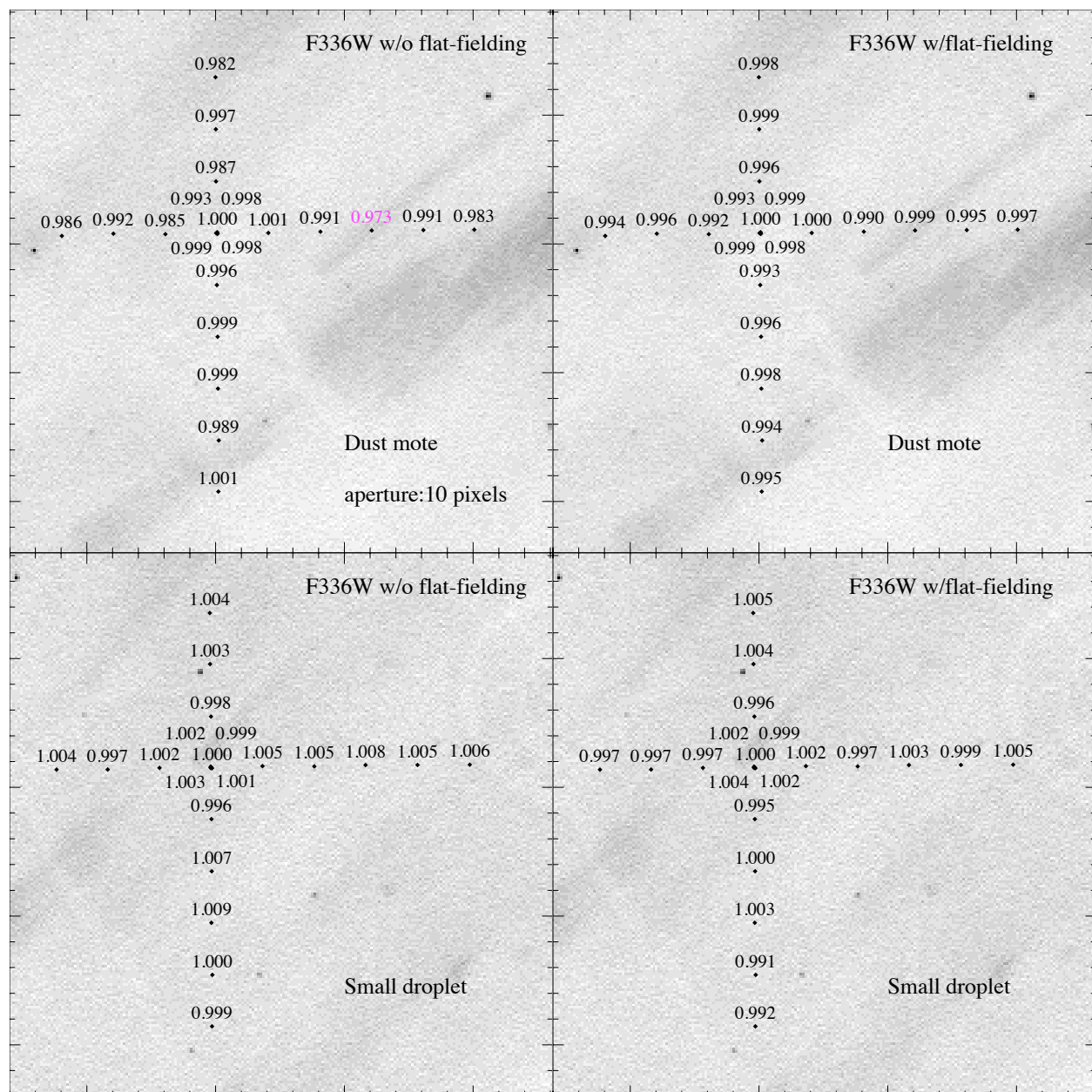


Figure A23: Photometric measurements in the F336W filter in the vicinity of two weak features: a dust mote (top panels) and a small droplet (bottom panels), without flat-fielding (left panels) and with flat-fielding (right panels), using a 10-pixel aperture. The measurements are shown superimposed on the external flat-field image, to indicate where they lie with respect to the flat-field features.

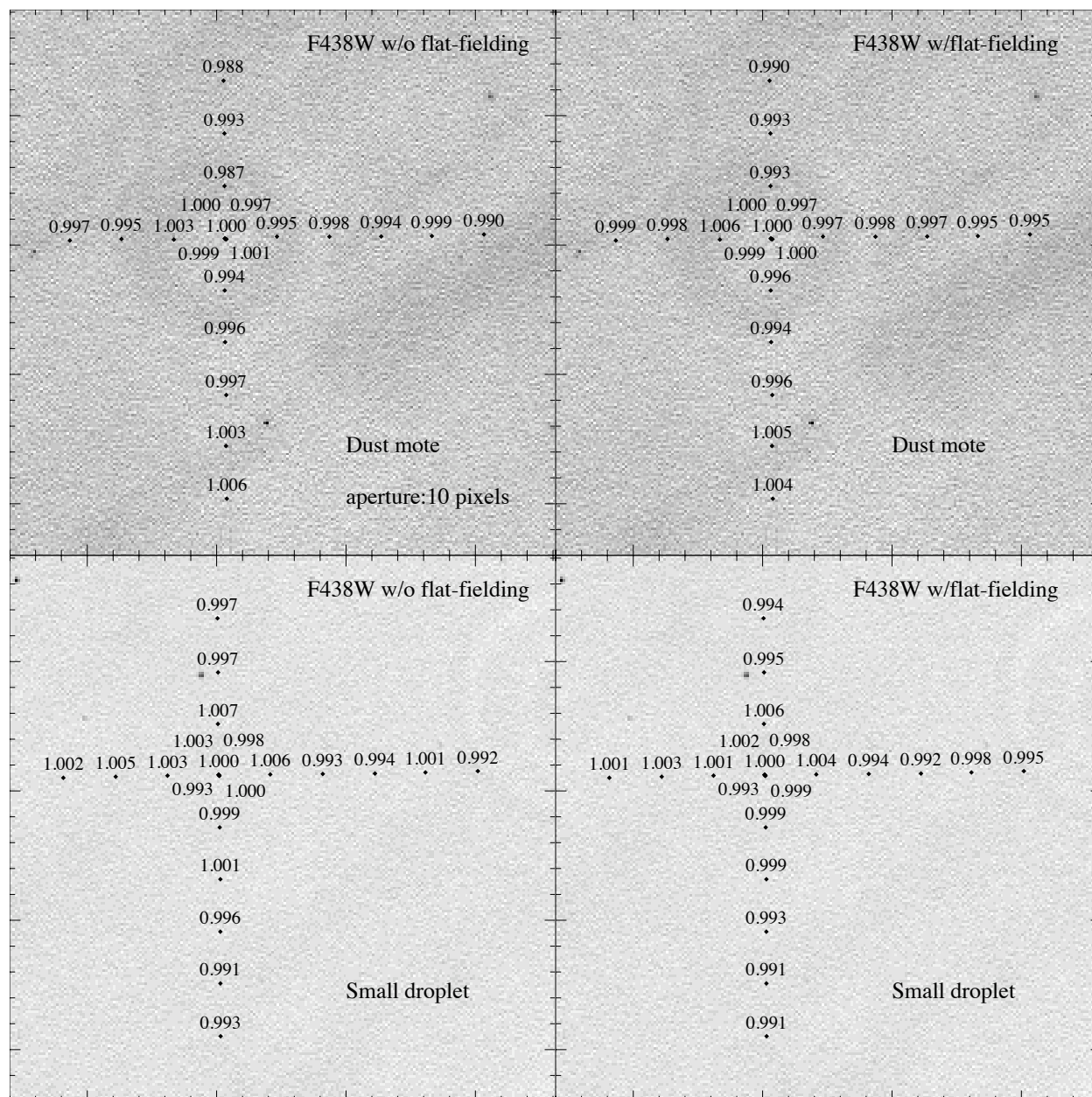


Figure A24: Photometric measurements in the F438W filter in the vicinity of two weak features: a dust mote (top panels) and a small droplet (bottom panels), without flat-fielding (left panels) and with flat-fielding (right panels), using a 10-pixel aperture. The measurements are shown superimposed on the external flat-field image, to indicate where they lie with respect to the flat-field features.

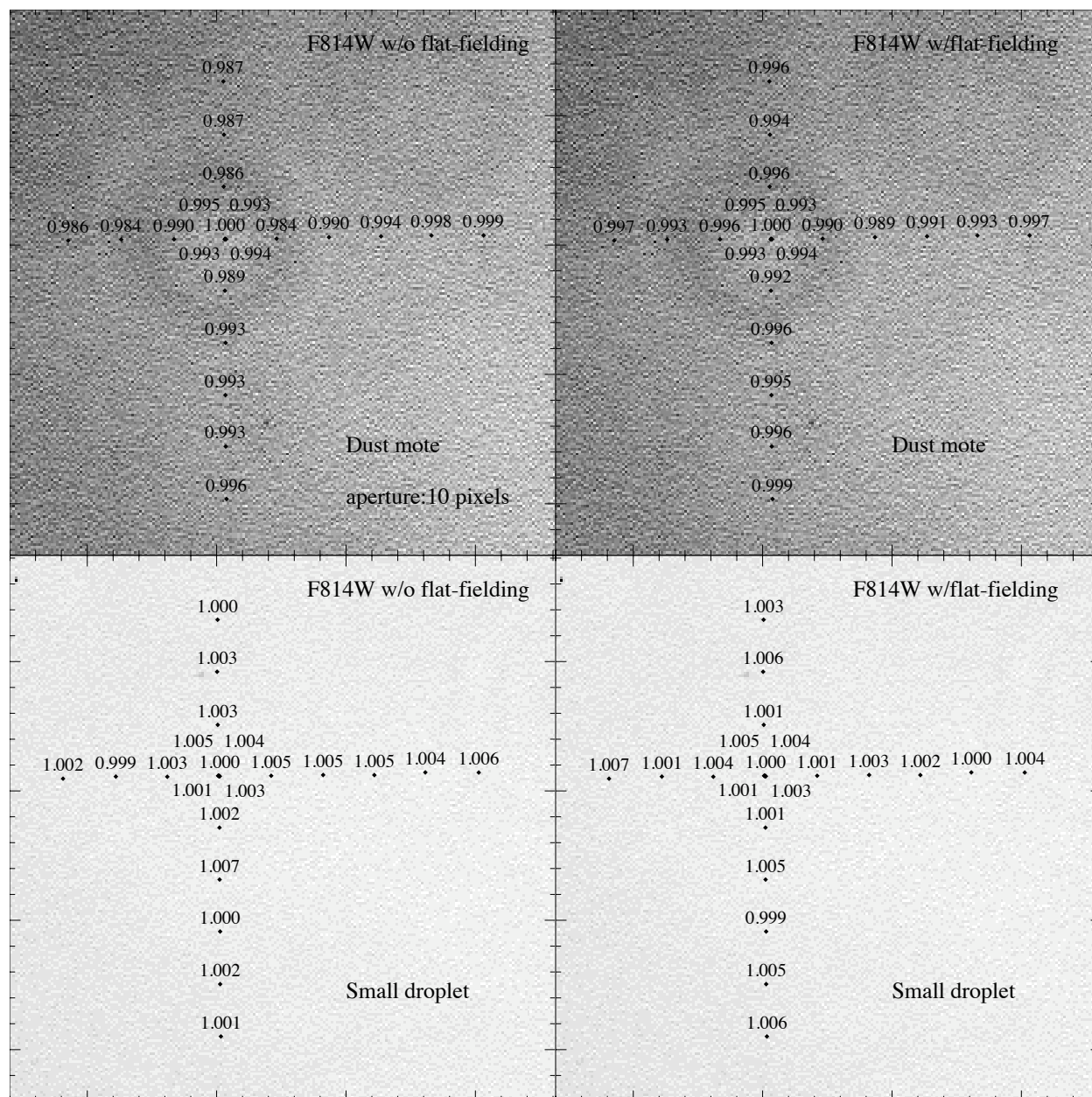


Figure A25: Photometric measurements in the F814W filter in the vicinity of two weak features: a dust mote (top panels) and a small droplet (bottom panels), without flat-fielding (left panels) and with flat-fielding (right panels), using a 10-pixel aperture. The measurements are shown superimposed on the external flat-field image, to indicate where they lie with respect to the flat-field features.

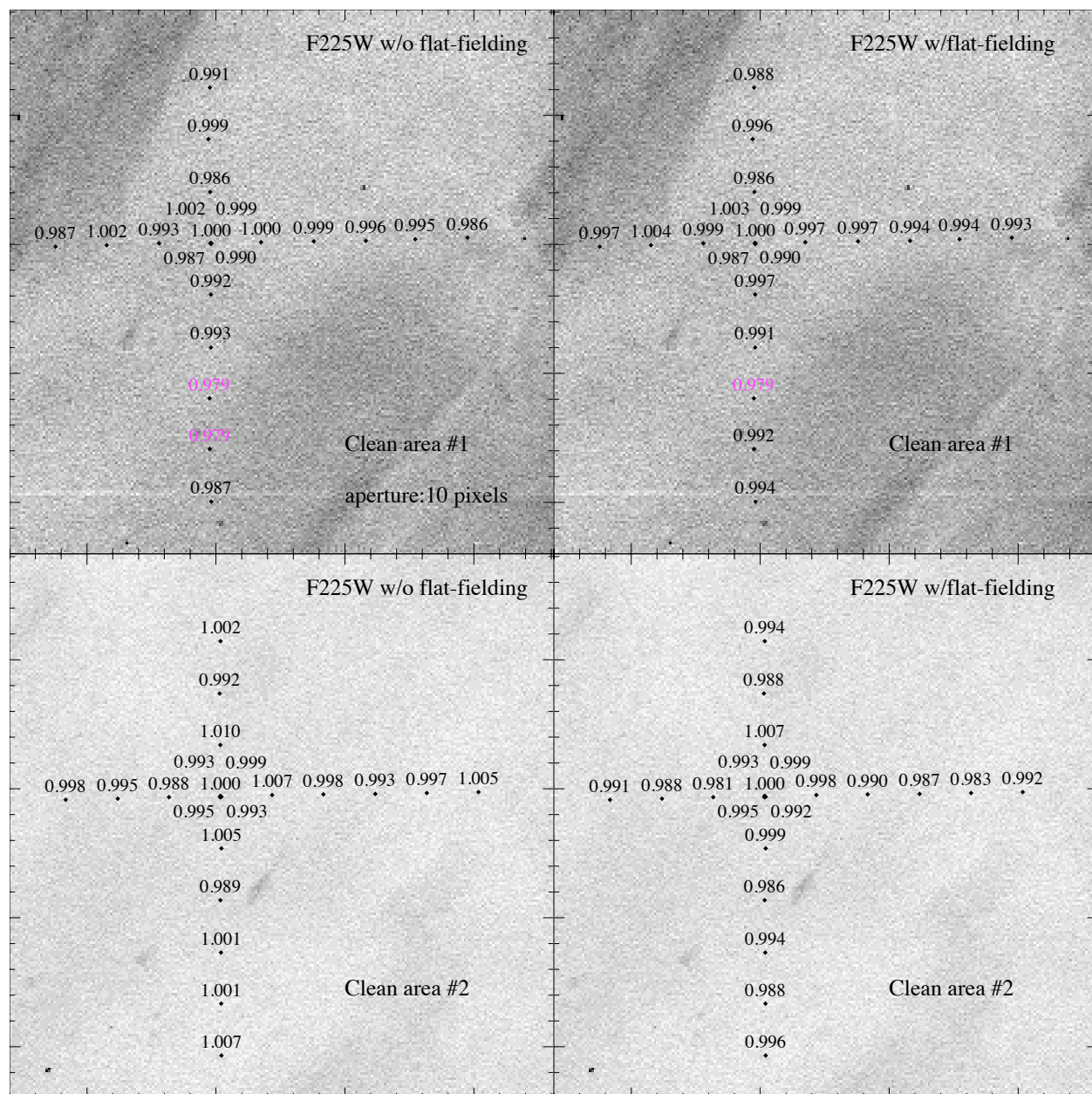


Figure A26: Photometric measurements in the F225W filter in the vicinity of two relatively featureless regions on the detector: clean area #1 (top panels) and clean area #2 (bottom panels), without flat-fielding (left panels) and with flat-fielding (right panels), using a 10-pixel aperture. The measurements are shown superimposed on the external flat-field image, to indicate where they lie with respect to the flat-field features.

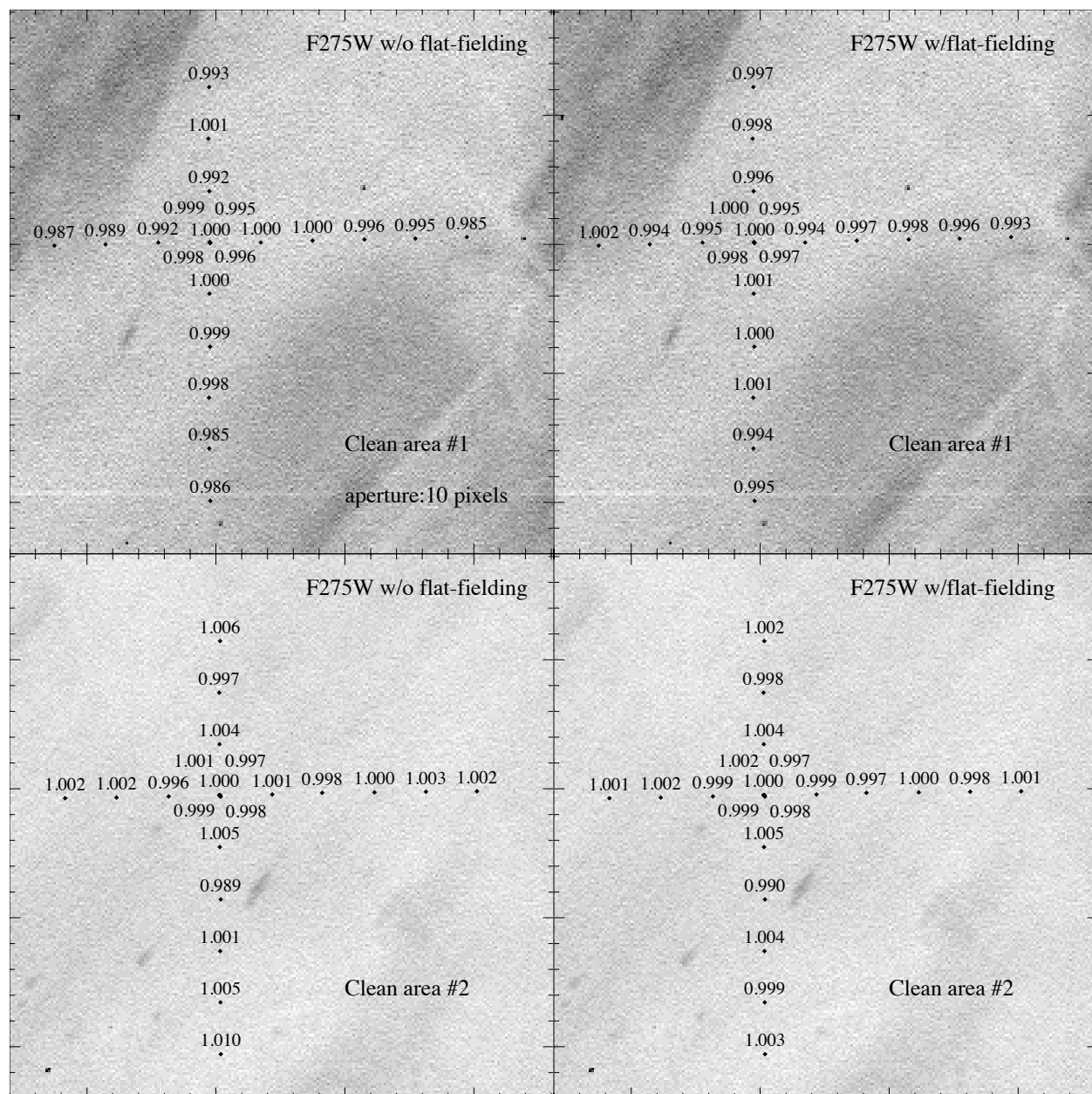


Figure A27: Photometric measurements in the F275W filter in the vicinity of two relatively featureless regions on the detector: clean area #1 (top panels) and clean area #2 (bottom panels), without flat-fielding (left panels) and with flat-fielding (right panels), using a 10-pixel aperture. The measurements are shown superimposed on the external flat-field image, to indicate where they lie with respect to the flat-field features.

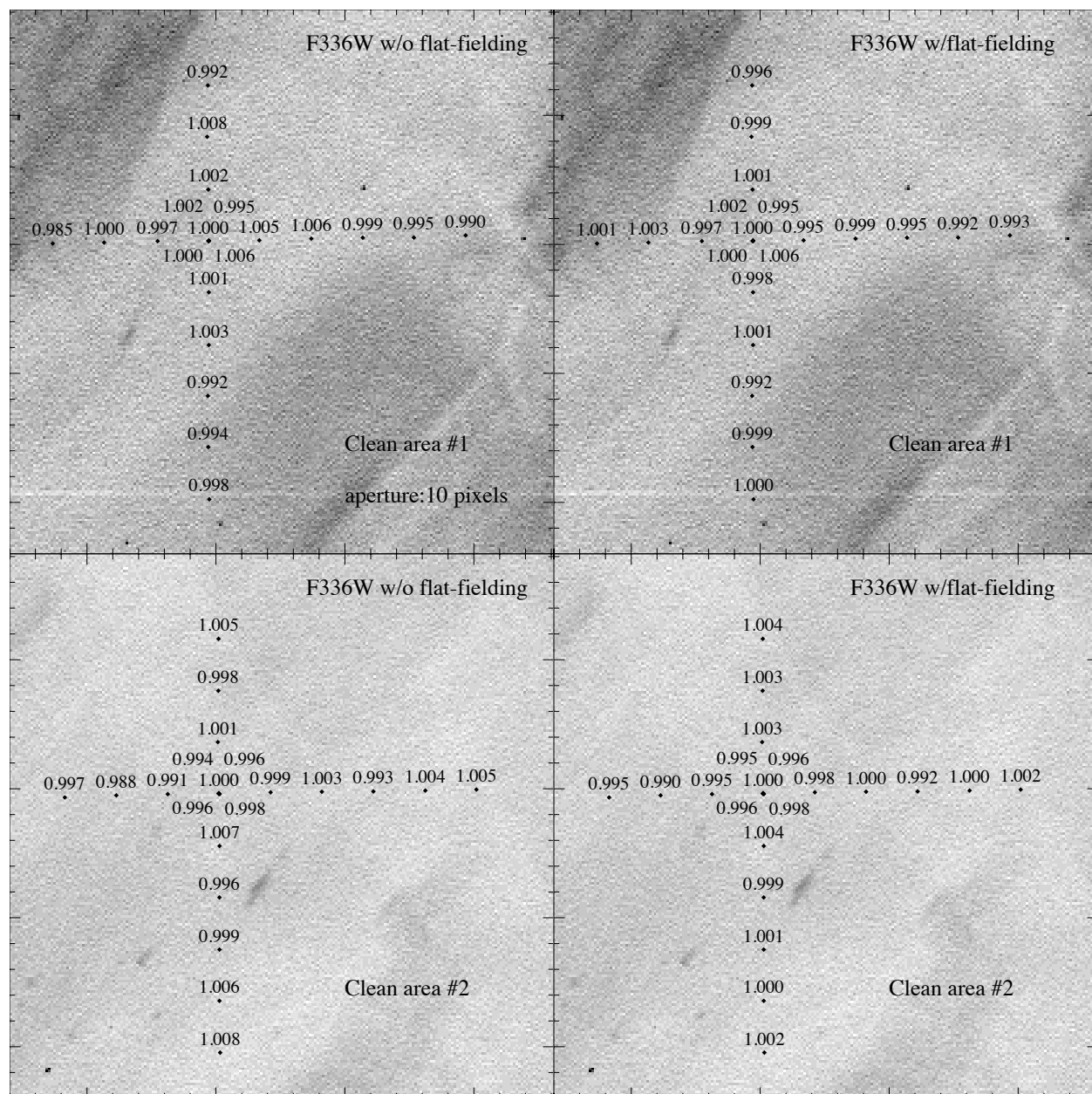


Figure A28: Photometric measurements in the F336W filter in the vicinity of two relatively featureless regions on the detector: clean area #1 (top panels) and clean area #2 (bottom panels), without flat-fielding (left panels) and with flat-fielding (right panels), using a 10-pixel aperture. The measurements are shown superimposed on the external flat-field image, to indicate where they lie with respect to the flat-field features.

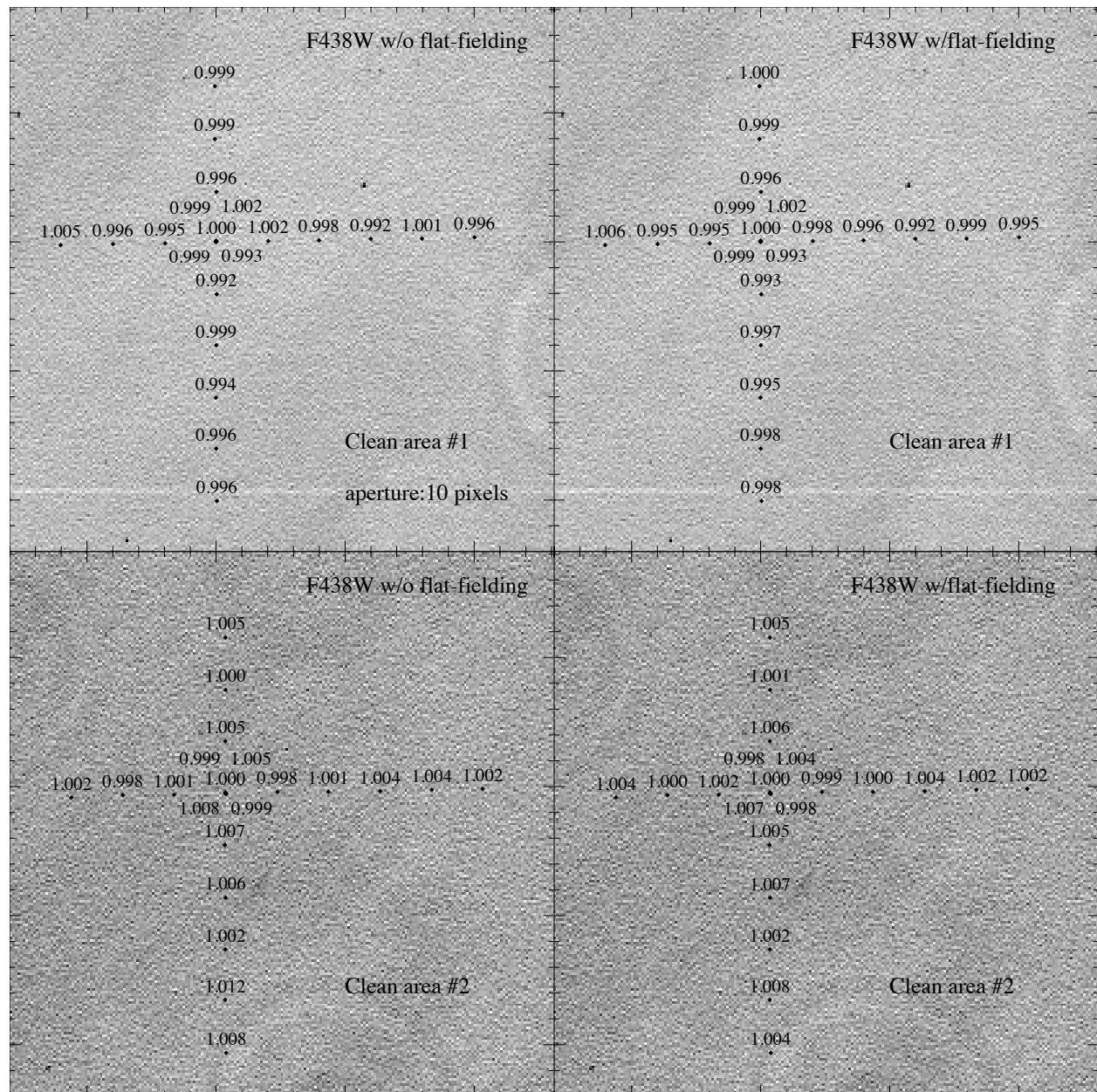


Figure A29: Photometric measurements in the F438W filter in the vicinity of two relatively featureless regions on the detector: clean area #1 (top panels) and clean area #2 (bottom panels), without flat-fielding (left panels) and with flat-fielding (right panels), using a 10-pixel aperture. The measurements are shown superimposed on the external flat-field image, to indicate where they lie with respect to the flat-field features.

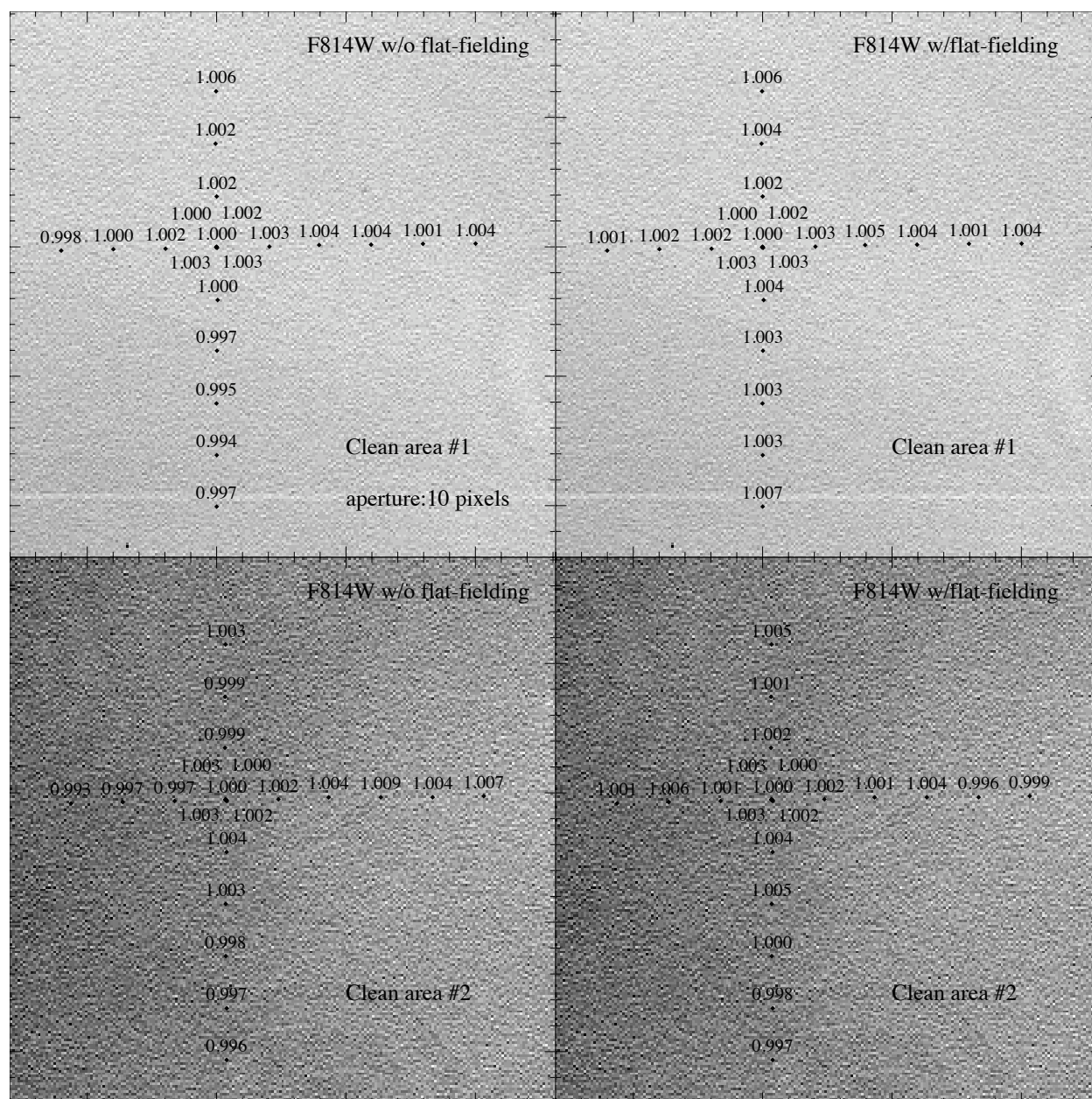


Figure A30: Photometric measurements in the F814W filter in the vicinity of two relatively featureless regions on the detector: clean area #1 (top panels) and clean area #2 (bottom panels), without flat-fielding (left panels) and with flat-fielding (right panels), using a 10-pixel aperture. The measurements are shown superimposed on the external flat-field image, to indicate where they lie with respect to the flat-field features.

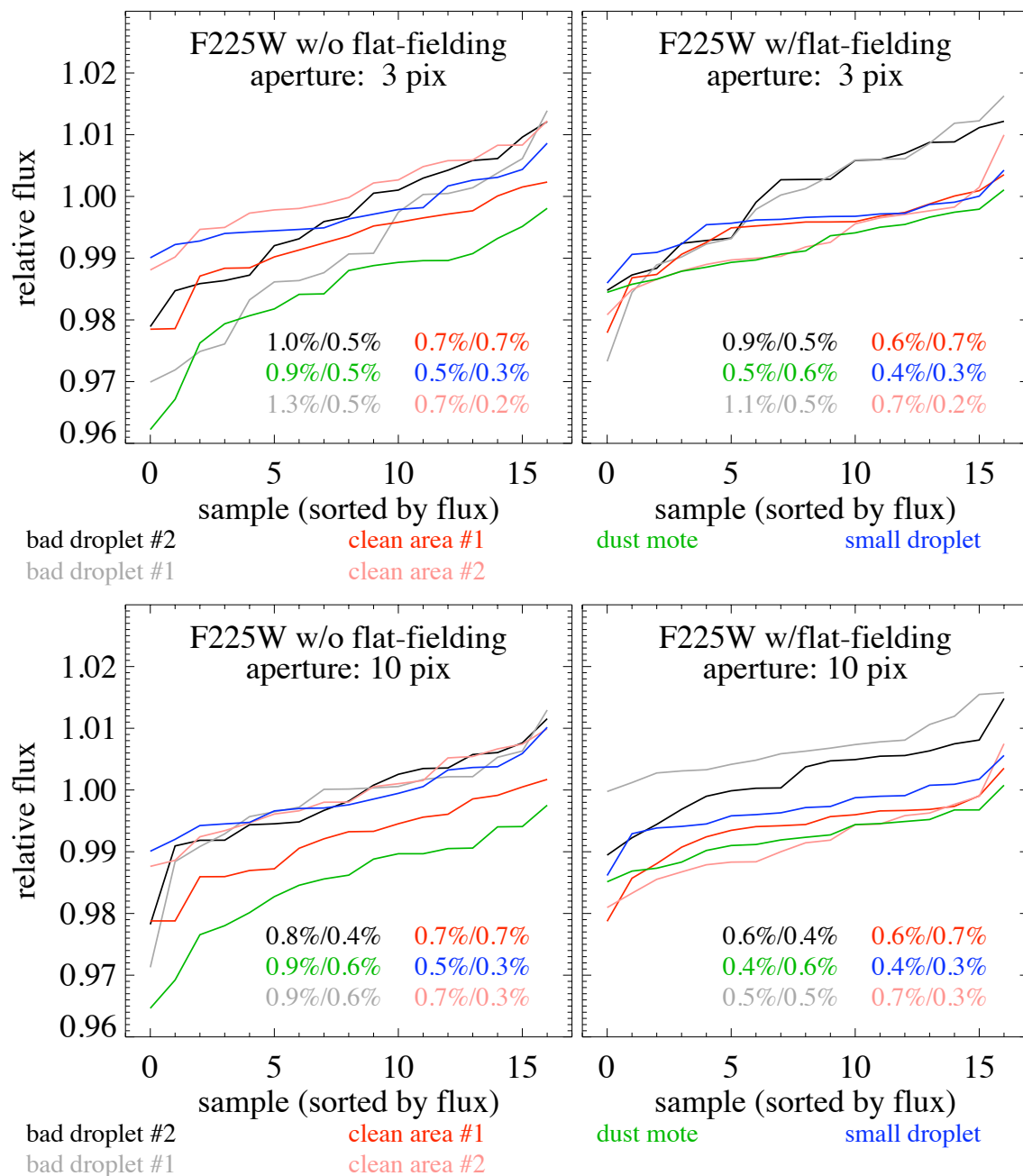


Figure A31: Summary of the F225W photometry shown in Figures A1, A6, A11, A16, A21, and A26. Results are shown before flat-fielding (left panels), after flat-fielding (right panels), with a 3-pixel aperture (top panels), and with a 10-pixel aperture (bottom panels). The repeated measurements in the central position were averaged to a single measurement to avoid biasing the curves and r.m.s. low. The pairs of numbers in each panel give the r.m.s. in the spatially distinct samples and the r.m.s. in the repeated center samples for comparison.

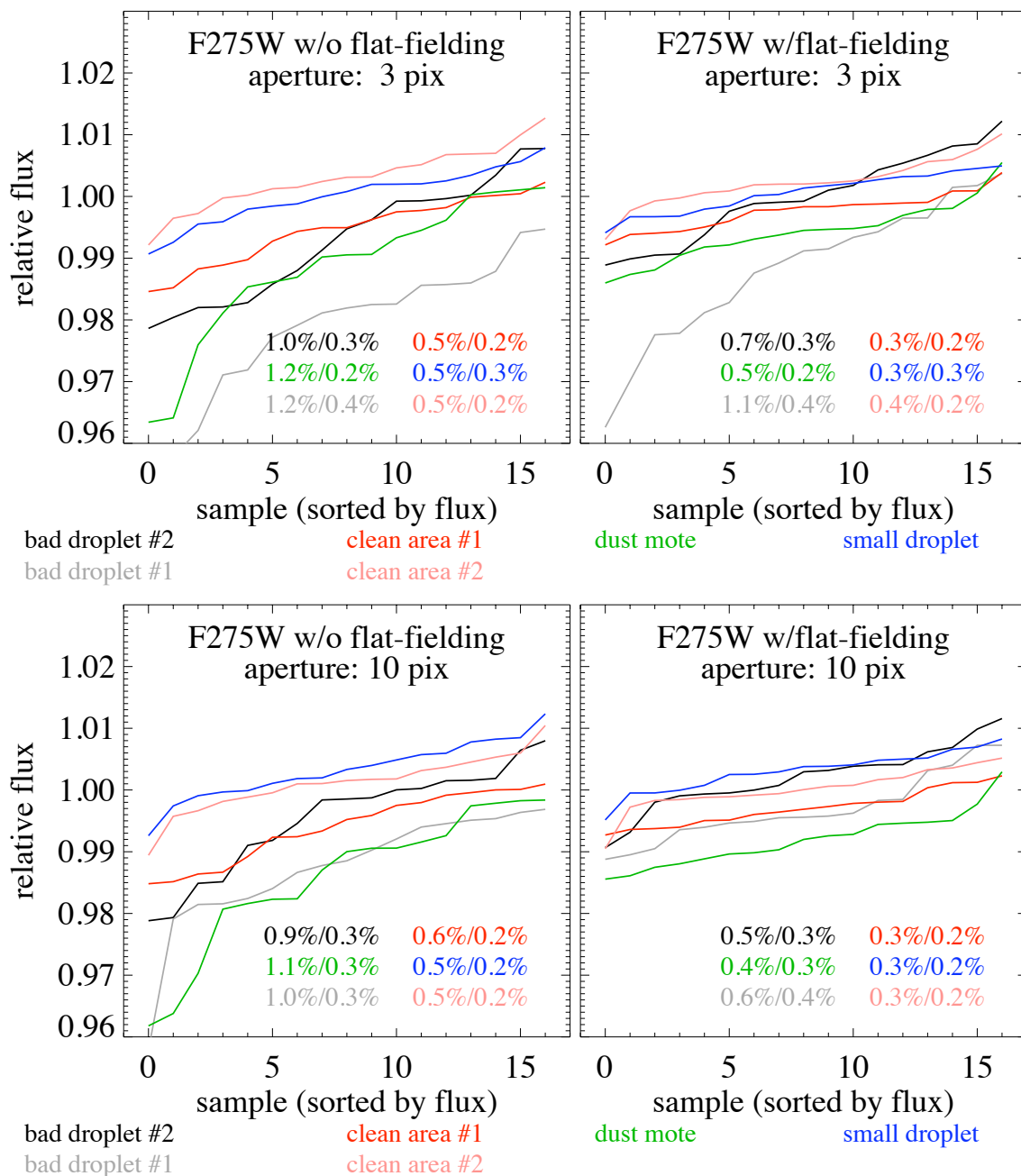


Figure A32: Summary of the F275W photometry shown in Figures A2, A7, A12, A17, A22, and A27. Results are shown before flat-fielding (left panels), after flat-fielding (right panels), with a 3-pixel aperture (top panels), and with a 10-pixel aperture (bottom panels). The repeated measurements in the central position were averaged to a single measurement to avoid biasing the curves and r.m.s. low. The pairs of numbers in each panel give the r.m.s. in the spatially distinct samples and the r.m.s. in the repeated center samples for comparison.

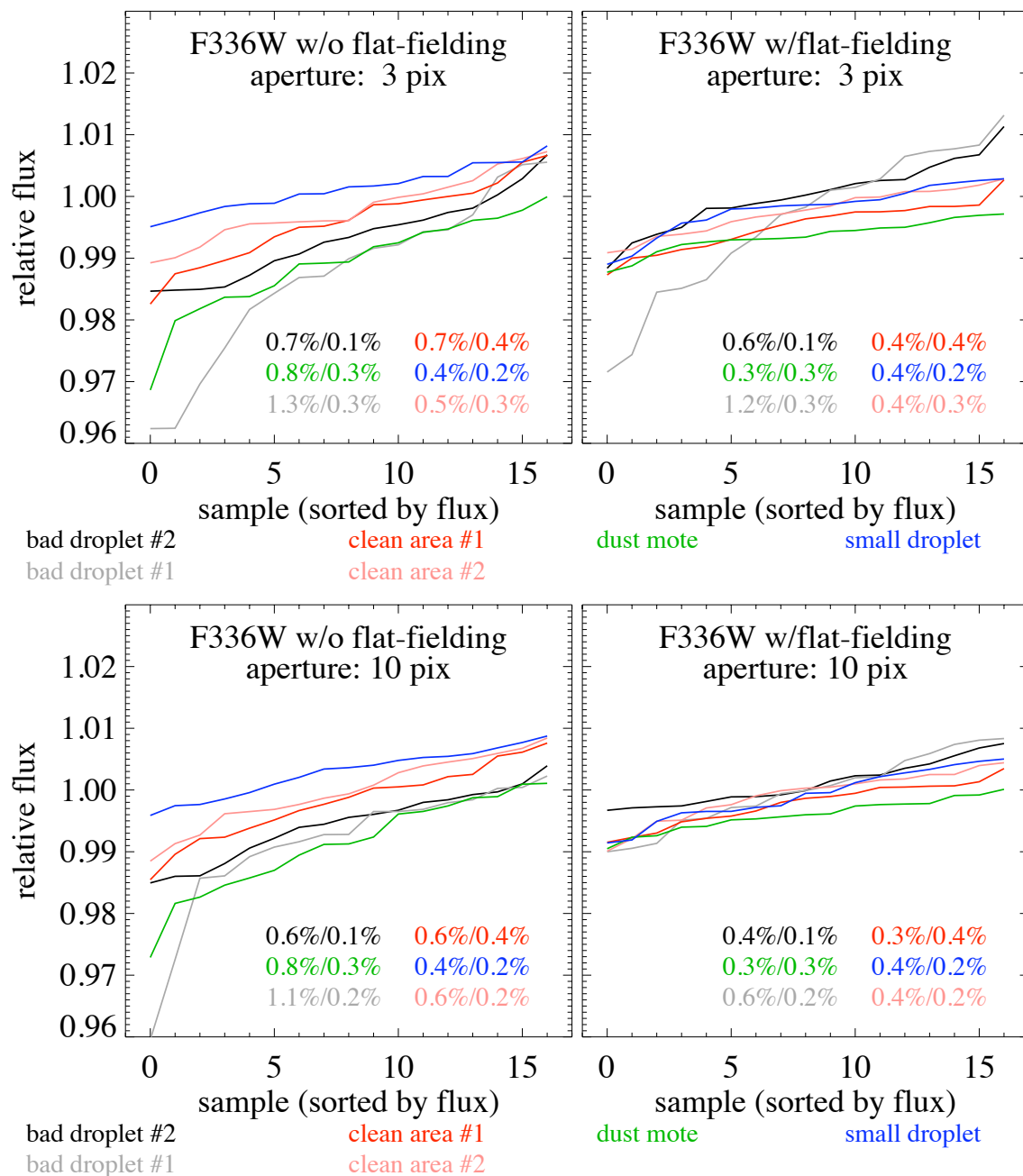


Figure A33: Summary of the F336W photometry shown in Figures A3, A8, A13, A18, A23, and A28. Results are shown before flat-fielding (left panels), after flat-fielding (right panels), with a 3-pixel aperture (top panels), and with a 10-pixel aperture (bottom panels). The repeated measurements in the central position were averaged to a single measurement to avoid biasing the curves and r.m.s. low. The pairs of numbers in each panel give the r.m.s. in the spatially distinct samples and the r.m.s. in the repeated center samples for comparison.

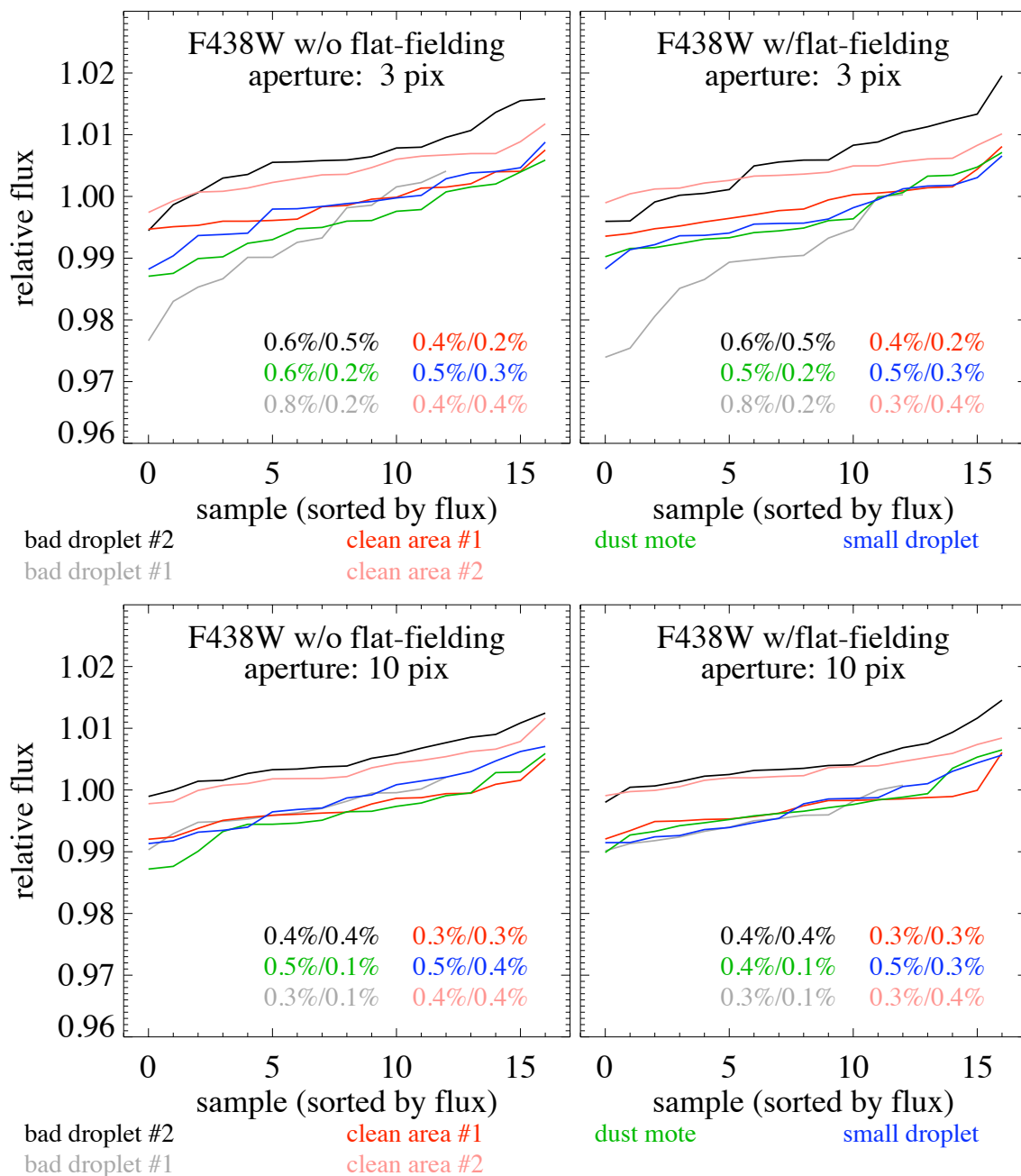


Figure A34: Summary of the F438W photometry shown in Figures A4, A9, A14, A19, A24, and A29. Results are shown before flat-fielding (left panels), after flat-fielding (right panels), with a 3-pixel aperture (top panels), and with a 10-pixel aperture (bottom panels). The repeated measurements in the central position were averaged to a single measurement to avoid biasing the curves and r.m.s. low. The pairs of numbers in each panel give the r.m.s. in the spatially distinct samples and the r.m.s. in the repeated center samples for comparison.

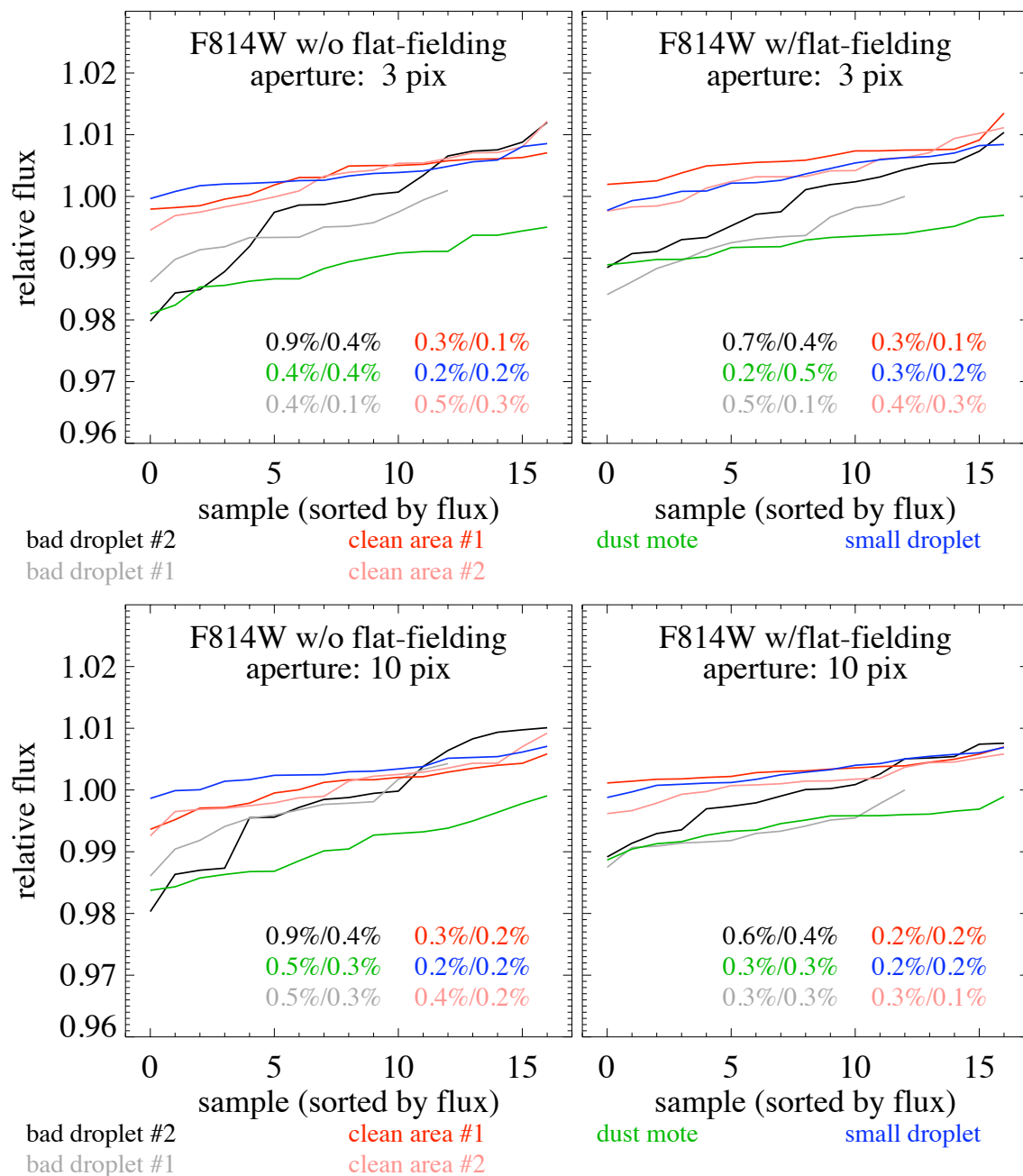


Figure A35: Summary of the F814W photometry shown in Figures A5, A10, A15, A20, A25, and A30. Results are shown before flat-fielding (left panels), after flat-fielding (right panels), with a 3-pixel aperture (top panels), and with a 10-pixel aperture (bottom panels). The repeated measurements in the central position were averaged to a single measurement to avoid biasing the curves and r.m.s. low. The pairs of numbers in each panel give the r.m.s. in the spatially distinct samples and the r.m.s. in the repeated center samples for comparison.

Appendix B - Encircled Energy and PSF Details

In this section we show the two-dimensional PSF profiles corresponding to the azimuthal averages shown in Figure 6. The point source is stepped in 4 pixel increments across a window feature, such that the feature moves from a point within the annulus to its edge.

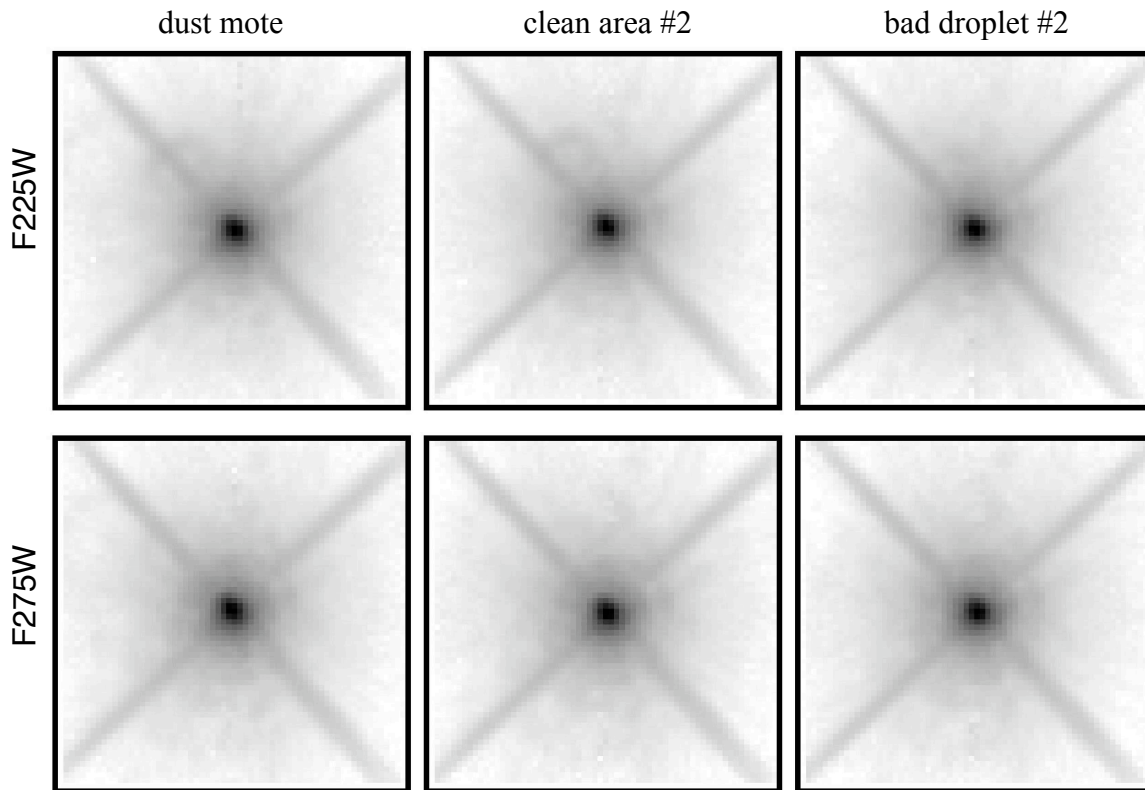


Figure B1: The PSF profiles at step #1 as the point source is stepped across a window feature in 4 pixel increments, corresponding to one of the curves in Figure 6. The annulus of the science beam intercepts the window feature.

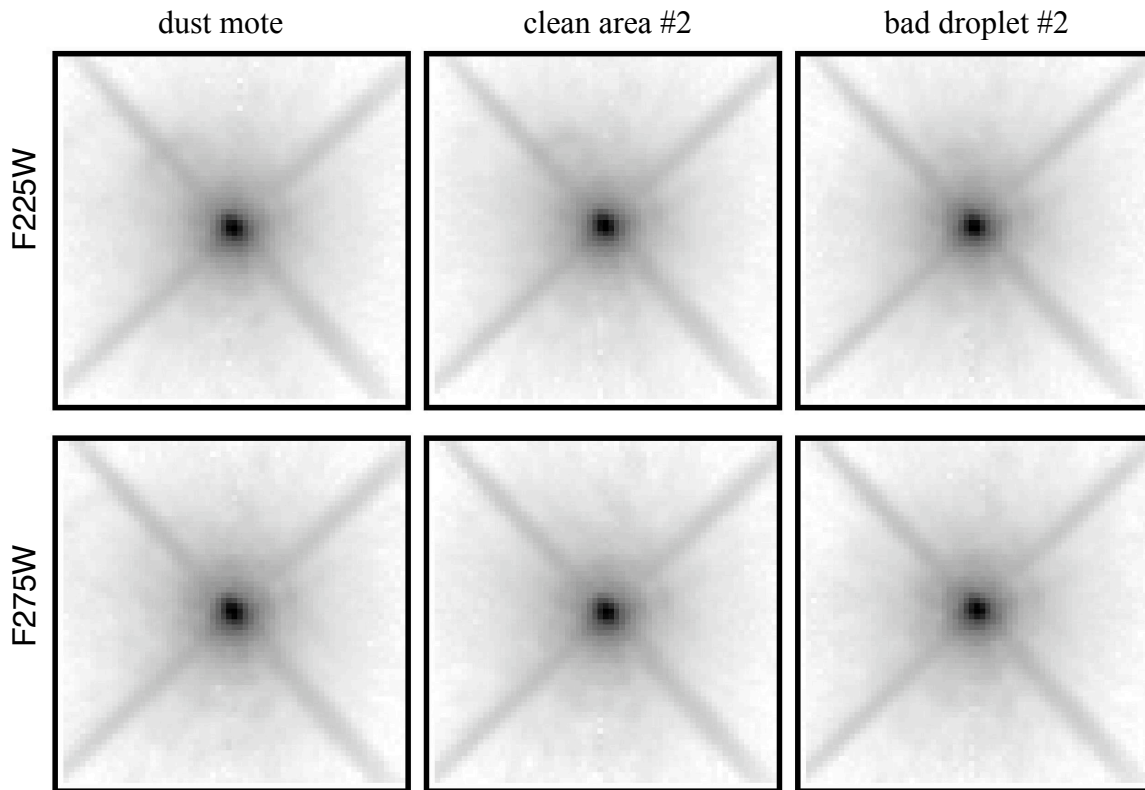


Figure B2: The PSF profiles at step #2 as the point source is stepped across a window feature in 4 pixel increments, corresponding to one of the curves in Figure 6. The annulus of the science beam intercepts the window feature.

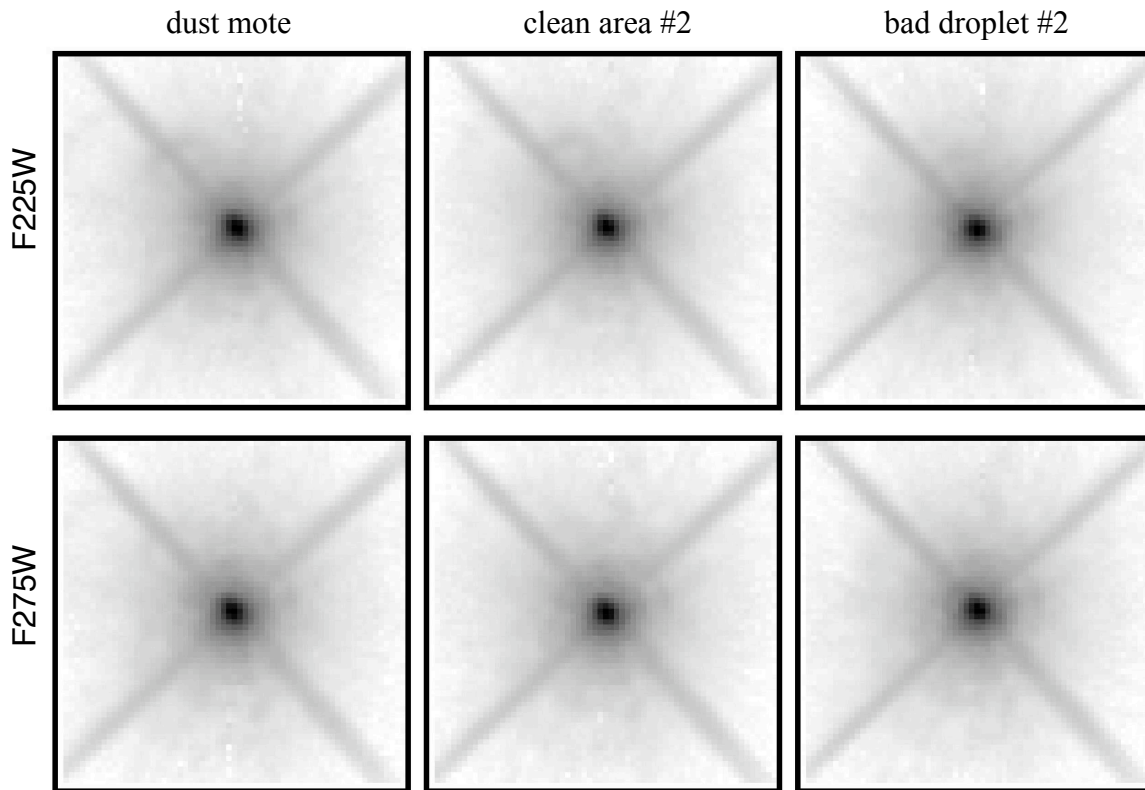


Figure B3: The PSF profiles at step #3 as the point source is stepped across a window feature in 4 pixel increments, corresponding to one of the curves in Figure 6. The annulus of the science beam intercepts the window feature.

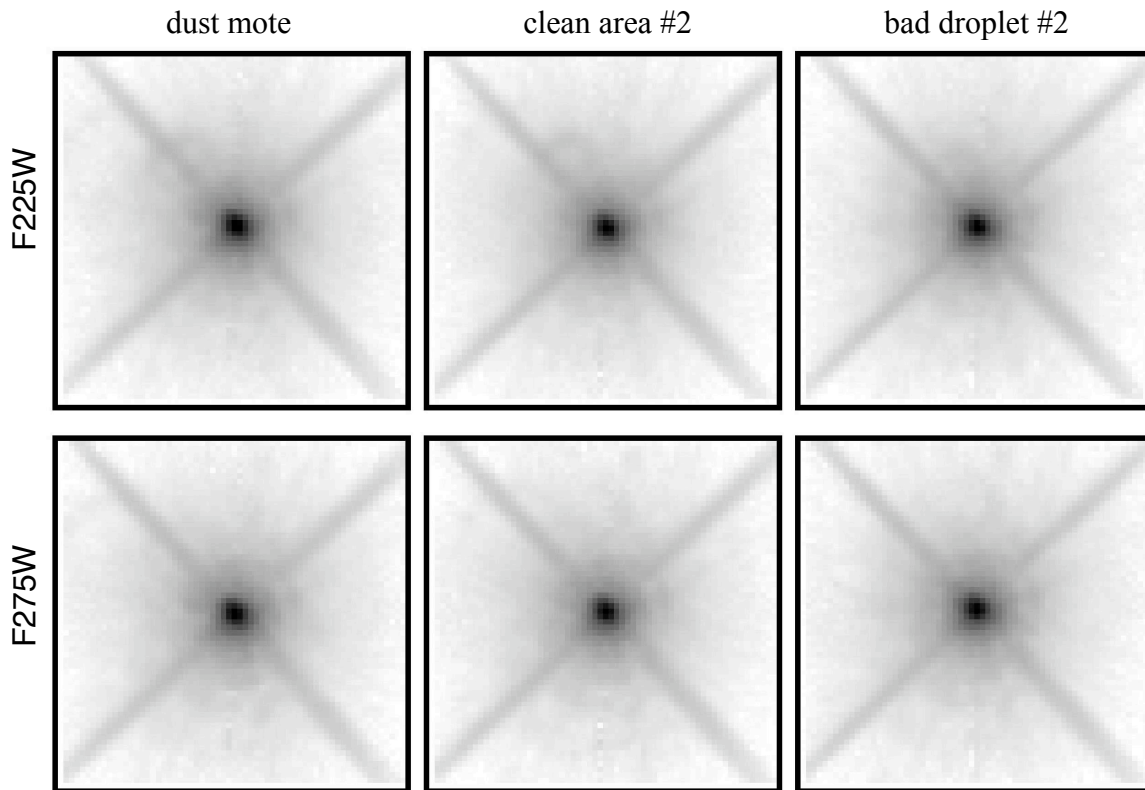


Figure B4: The PSF profiles at step #4 as the point source is stepped across a window feature in 4 pixel increments, corresponding to one of the curves in Figure 6. The annulus of the science beam intercepts the window feature.

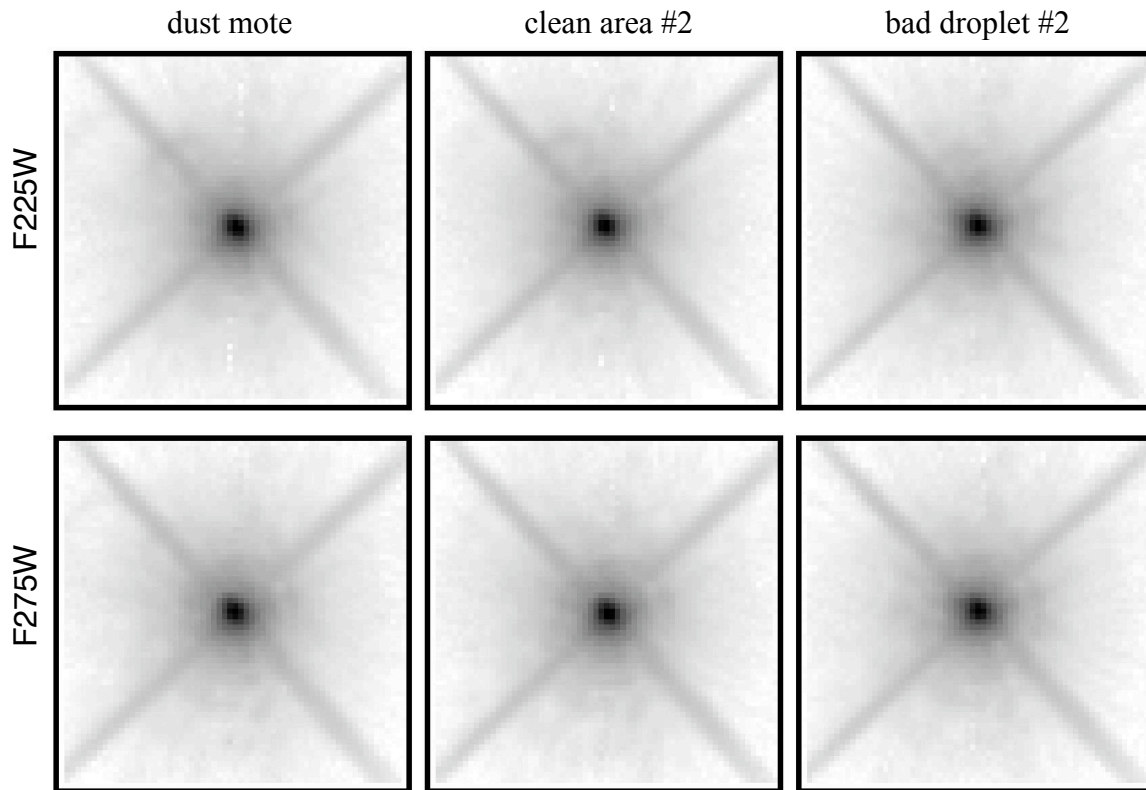


Figure B5: The PSF profiles at step #5 as the point source is stepped across a window feature in 4 pixel increments, corresponding to one of the curves in Figure 6. The annulus of the science beam intercepts the window feature.

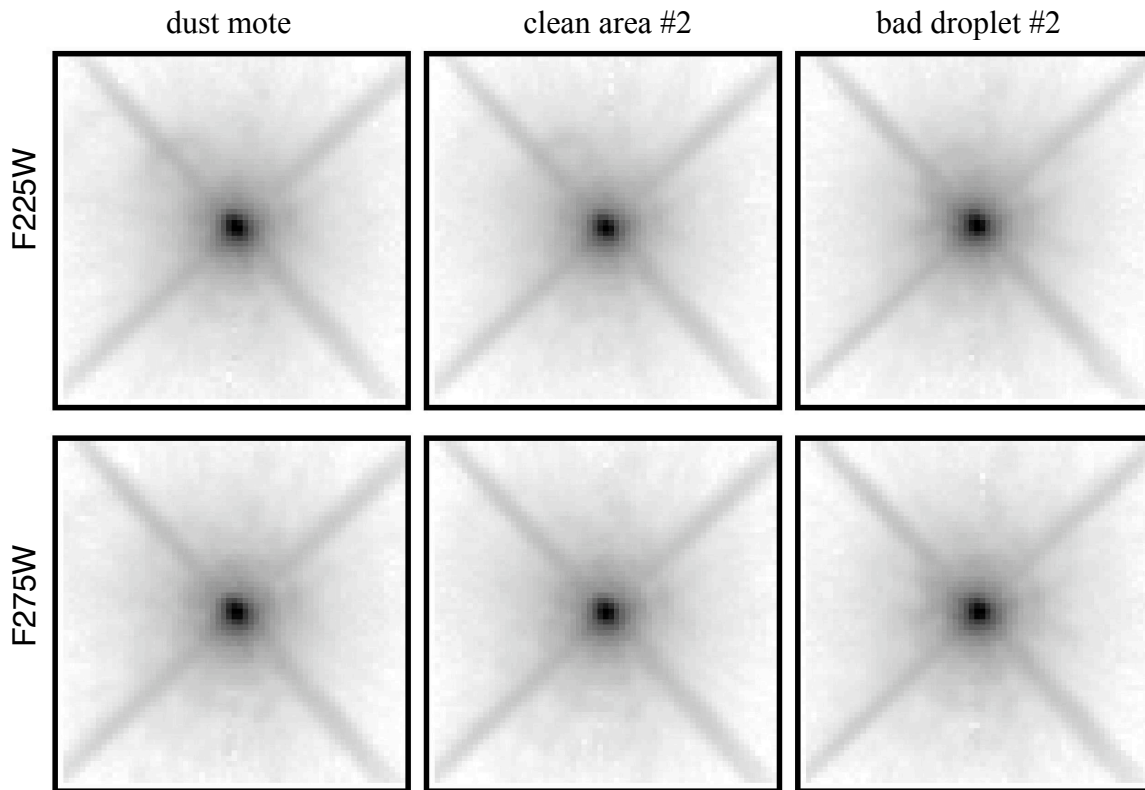


Figure B6: The PSF profiles at step #6 as the point source is stepped across a window feature in 4 pixel increments, corresponding to one of the curves in Figure 6. The annulus of the science beam intercepts the window feature.